

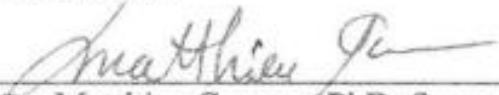
Copyright
by
Savannah Seely
2024

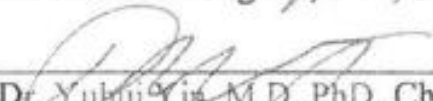
The Dissertation Committee for Savannah Seely

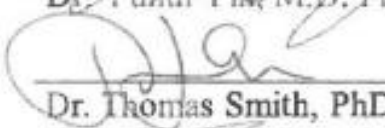
Certifies this is the approved version of the following dissertation:

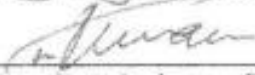
Investigating the molecular mechanism of ribosome recycling

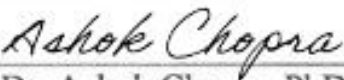
Committee:

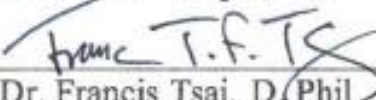

Dr. Matthieu Gagnon, PhD, Supervisor


Dr. Yukui Yin, M.D. PhD, Chair


Dr. Thomas Smith, PhD


Dr. Petr Leiman, PhD


Dr. Ashok Chopra, PhD


Dr. Francis Tsai, D.Phil

Investigating the molecular mechanism of ribosome recycling

by

Savannah Marie Seely, B.S.

Dissertation

Presented to the Faculty of the Graduate School of Biomedical Sciences of

The University of Texas Medical Branch

in Partial Fulfillment

of the Requirements

for the Degree of

Doctor of Philosophy

The University of Texas Medical Branch

March, 2024

Dedication

**This work is dedicated to Millie and Scout, may I finally be the person my
dogs believe I am.**

Acknowledgements

First and foremost, I would like to give enormous thanks to my family. To my parents, who have loved me so fiercely all my life, and have modeled for me what it means to live with kindness, integrity, and perseverance. To my sister Braelynn, who was my first friend in life and remains my best friend, and who I look up to in so many ways. To my sister April, who I've had the immense pleasure of watching grow into a beautiful young woman and motivates me to always be myself. To my brother Ryan, who inspires me to live with child-like joy and curiosity. I love you all beyond words and I thank you for making this possible for me. I hope that one day I can repay you for all you've given me, I did this all for you.

I would like to thank my husband, Jarrod, for the love and support he has given me throughout graduate school. For every morning cup of coffee, every hug after a long day, and everything in between. I'm so grateful to have this life with him and his unconditional support of my dreams.

I would like to thank Dr. Dustin Patterson, for being my mentor during my undergraduate career and opening the door for me to find my passion in research. I would have never gone to graduate school without his guidance and support.

I would like to thank Dr. Michael Sherman, for all the time he spent with me teaching me about structural biology and all the sage wisdom he's granted me over the years. The skills and lessons he's given me are priceless and I will carry them with me throughout my life.

I would like to thank Mandi Feinberg, the best friend I could hope for. Going through this experience with Mandi has made all its challenges manageable and brought me joy in the hard times. I'm grateful to have made a friend in Mandi; that I had her to cry with, celebrate with, and enjoy a beer with these years.

To my lab members, I cannot thank you enough for the opportunity to share these years and learn from you all. Dr. Mariia Rybak and Naveen Ganji, I am so thankful for all the laughs, advice, and assistance. A special thank you to Dr. Ritwika Basu, who has been with me from the beginning. I am lucky to have worked alongside such a talented scientist and incredible woman, I am blessed to call you my friend.

Finally, I cannot express enough gratitude for my mentor, Dr. Matthieu Gagnon, for all that he has done for me in my graduate career. There is so much I could say about the things Dr. Gagnon has taught me, the encouragement he has given me, and the grace he extended to me when I needed it. There were numerous times I felt that I was not in the right place, but Dr. Gagnon always gave me the guidance I needed to find my own way. I have thrived under his mentorship and have had the opportunity to grow as a critical thinker and researcher. Thank you, Matt, for letting me be a part of your circus.

Investigating the molecular mechanism of ribosome recycling

Savannah Marie Seely, Ph.D.

The University of Texas Medical Branch, 2024

Supervisor: Matthieu Gagnon, Ph.D.

In all living cells, the ribosome translates the genetic information carried by messenger RNAs (mRNAs) into proteins. The process of ribosome recycling, a key step during protein synthesis that ensures ribosomal subunits remain available for new rounds of translation, has been largely overlooked. Despite being essential to the survival of the cell, several mechanistic aspects of ribosome recycling remain unclear. Aminoglycosides are a class of antibiotics that bind to ribosomal RNA and exert pleiotropic effects on ribosome function, including recycling inhibition. Amikacin, the semisynthetic derivative of kanamycin, is commonly used for treating severe infections with multidrug-resistant, aerobic Gram-negative bacteria. Amikacin carries the 4-amino-2-hydroxy butyrate (AHB) moiety at the N¹ amino group of the central 2-deoxystreptamine (2-DOS) ring, which may confer amikacin a unique ribosome inhibition profile. During stress conditions such as antibiotic exposure, ribosomes stall on messenger RNAs, leading to inhibition of protein synthesis. To remobilize ribosomes, bacteria use rescue factors such as HflXr, that catalyzes the dissociation of translationally inactive ribosomes into individual subunits. Here we use *in vitro* fast kinetics combined with X-ray crystallography and cryo-EM to dissect the mechanisms of ribosome inhibition by amikacin and the rescue of stalled ribosome

through HflXr-mediated recycling. Amikacin interferes with tRNA translocation, release factor-mediated peptidyl-tRNA hydrolysis, and ribosome recycling, traits attributed to the additional interactions amikacin makes with the decoding center. The binding site in the large ribosomal subunit proximal to the 3'-end of tRNA in the peptidyl (P) site lays the groundwork for rational design of amikacin derivatives with improved antibacterial properties. Using time-resolved cryo-EM, we show that within the 70S ribosome, HflXr displaces helix H69 of the 50S subunit and induces long-range movements of the platform domain of the 30S subunit, disrupting inter-subunit bridges B2b, B2c, B4, B7a, and B7b. Our findings unveil a unique ribosome recycling strategy by HflXr which is distinct from that mediated by RRF and EF-G. The resemblance between HflXr and housekeeping HflX suggests that the alternative ribosome recycling mechanism reported is universal in the prokaryotic kingdom.

TABLE OF CONTENTS

List of Figures.....	xiii
List of Abbreviations.....	xiv
Chapter 1, Mechanisms of ribosome recycling in bacteria: a structural perspective	1
1.1 Bacterial Translation	1
1.2 RRF is a structural mimic of tRNA.....	3
1.3 The concerted action of EF-G and RRF recycles the ribosome.....	9
1.4 Select bacteria harbor multiple copies of EF-G.....	16
1.5 Some aminoglycosides inhibit ribosome recycling.....	17
1.6 HflX is an alternative ribosome recycling factor.....	19
1.7 Concluding remarks.....	23
Chapter 2, Molecular basis of the pleiotropic effects by the antibiotic amikacin on the ribosome	25
2.1 Introduction.....	25
2.2 Results.....	28
2.2.1 Crystal structures of the ribosome bound to amikacin and kanamycin.....	28
2.2.2 Amikacin interferes with mRNA translocation during peptide elongation.....	33
2.2.3 Amikacin inhibits release factor-mediated peptide release..	36
2.2.4 Amikacin inhibits recycling of the ribosome by EF-G and RRF.....	38

2.2.5 Cryo-EM structure of the <i>E. coli</i> ribosome bound to amikacin.....	39
2.2.6 A1408G ribosomes are resistant to amikacin.....	41
2.3 Discussion.....	42
2.4 Methods.....	47
2.4.1 Purification of 70S ribosomes, mRNAs, initiator tRNA, and tRNA ^{Phe}	47
2.4.2 Dipeptide and tripeptide formation experiments.....	49
2.4.3 Pyrene-mRNA based assay for ribosomal translocation.....	50
2.4.4 Measurement of RF-mediated peptide release.....	50
2.4.5 Ribosome recycling.....	51
2.4.6 Minimum inhibitory concentration (MIC) measurement.....	52
2.4.7 X-ray crystallographic structure determination.....	53
2.4.8 Cryo-EM data acquisition, image processing, and structure determination.....	55
2.4.9 Inter-subunit contact surface area at bridge B5.....	58
2.4.10 Figures.....	58
2.4.11 Data Availability.....	58
Chapter 3, Mechanistic insights into the alternative ribosome recycling by HflXr.....	60
3.1 Introduction.....	60
3.2 Materials and Methods.....	61
3.2.1 Preparation of 70S ribosomes, HflXr, and deacylated tRNA ^{phe}	61

3.2.2 Rapid-kinetics measurements.....	64
3.2.3 Sample preparation, cryo-electron microscopy and data acquisition.....	65
3.2.4 Cryo-electron microscopy image processing.....	66
3.2.5 Model building and refinement.....	71
3.2.6 PISA calculations.....	72
3.2.7 Figure generation.....	73
3.3 Results.....	73
3.3.1 HflXr-mediated ribosome recycling visualized by time-resolved cryo-EM.....	73
3.3.2 HflXr dismantles the non-rotated ribosome.....	76
3.3.3 The rotated ribosome bound to HflXr remains intact.....	82
3.3.4 Structure of the post-splitting 50S subunit complexed with HflXr.....	84
3.4 Discussion.....	86
3.5 Data availability.....	92
Chapter 4 Conclusions.....	94
4.1 Summary and contributions to the field.....	94
4.2 Future Directions.....	97
Appendix A, Chapter 2 Supplementary Materials.....	100
Appendix B, Chapter 3 Supplementary Materials.....	115
Bibliography/References.....	137
Vita.....	150

List of Figures

Figure 1.1: RRF is a tRNA mimic with a flexibly disposed domain II	3
Figure 1.2: Domain II of RRF is flexibly disposed on the 70S ribosome	5
Figure 1.3: RRF in the post-termination complex (PoTC) is not compatible with tRNA in the p/P state of binding and EF-G on the 70S ribosome	8
Figure 1.4: Pre-recycling complex with p/R- and E-site tRNAs	14
Figure 1.5: Cryo-EM structure of E. coli 50S subunit bound to HflX.....	19
Figure 1.6: Interactions of HflX with the 50S ribosomal subunit.....	22
Figure 2.1: Overview of the Thermus thermophilus 70S ribosome bound to amikacin.....	28
Figure 2.2: Canonical binding site of amikacin near the decoding center.....	29
Figure 2.3: Amikacin binding site in the large subunit proximal to the P-site tRNA.	30
Figure 2.4: Amikacin binding site at inter-subunit bridge B5.....	32
Figure 2.5: Effects of amikacin on the kinetics of peptide release and ribosome recycling.....	37
Figure 3.1: Time-resolved cryo-EM of HflXr-mediated ribosome recycling.....	74
Figure 3.2: HflXr displaces H69 and h44 without disrupting bridge B2a.....	78
Figure 3.3: HflXr induces conformational changes in the platform domain of the 30S subunit that break multiple inter-subunit bridges.....	79
Figure 3.4: Comparison of the direction of movement of the 30S platform in canonical ribosome ratcheting and HflXr-mediated recycling.....	83
Figure 3.5: HflXr alters the conformation of H69 post-splitting whereas the NTD-II acts as a sensor of the PTC occupancy.....	86

Figure 3.6: Model of HflXr-mediated ribosome recycling.....89

List of Abbreviations

UTMB	University of Texas Medical Branch
GSBS	Graduate School of Biomedical Sciences
RNA	ribonucleic acid
rRNA	ribosomal RNA
tRNA	transfer RNA
mRNA	messenger RNA
aa-tRNA	aminoacyl tRNA
LSU	large subunit
SSU	small subunit
DC	decoding center
PTC	peptidyl transferase center
SRL	sarcin ricin loop
NPET	nascent peptide exit tunnel
GAC	GTP activating center
A site	aminoacyl site
P site	peptidyl site
E site	exit site
TC	termination complex
Pre-TC	pre-termination complex
Post-TC	post-termination complex
H#	large subunit rRNA helix #
h#	small subunit rRNA helix #

uL#	universal large subunit protein #
uS#	universal small subunit protein #
bL#	bacterial large subunit protein #
bS#	bacterial small subunit protein #
IF1	initiation factor 1
IF2	initiation factor 2
IF3	initiation factor 3
EF-G	elongation factor G
EF-Tu	elongation factor Tu
RF1	release factor 1
RF2	release factor 2
RF3	release factor 3
RRF	ribosome recycling factor
HPF	hibernation promoting factor
EF-G2 _{mt}	mitochondrial elongation factor 2
RRF _{mt}	mitochondrial ribosome recycling factor
ODN	Obg, DRG1 and Nog1 protein family
GTPBP6	guanosine tri-phosphate binding protein 6
ArfA	alternative ribosome-rescue factor A
ArfB	alternative ribosome-rescue factor B
CTD	C terminal domain
NTD	N terminal domain
NTD-I	N terminal subdomain I

NTD-II	N terminal subdomain II
Met	methionine
fMet	formyl-methionine
Leu	leucine
Phe	phenylalanine
Tyr	tyrosine
Arg	arginine
GTP	guanosine tri-phosphate
ATP	adenosinetri-phosphate
UTP	uridine tri-phosphate
CTP	cytosine tri-phosphate
GDP	guanosine di-phosphate
ADP	adenosine di-phosphate
GDPCP	5'-guanosyl-methylene-triphosphate
GDPNP	5'-guanylyl imidodiphosphate
ERY	erythromycin
AMK	amikacin
AHB	4-amino-2-hydroxy butyrate
2-DOS	2-deoxystreptamine
ABK	arbekacin
KAN	kanamycin
BlaS	blasticidin S
BacA	bactobolin A

Cryo-EM	cryo-electron microscopy
NMR	nuclear magnetic resonance
smFRET	single molecule-fluorescence resonance energy transfer
PISA	proteins, interfaces, surface and assemblies
MIC	minimum inhibitory concentration
K _i	half-maximal inhibitory concentration
SEM	standard error of the mean
k _{app}	apparent rate
t _{1/2}	reaction half life
IM	initiation mix
EM	elongation mix
BOP	BODIPY™
BMD	broth microdilution
FSC	fourier shell correction
CTF	contrast transfer function
2D	two dimensional
3D	three dimensional
PDB	protein data bank
EMDB	electron microscopy data bank
<i>E. coli</i>	<i>Escherichia coli</i>
<i>T. thermophilus</i>	<i>Thermus thermophilus</i>
<i>L. innocua</i>	<i>Listeria innocua</i>
<i>L. monocytogenes</i>	<i>Listeria monocytogenes</i>

<i>M. abscessus</i>	<i>Mycobacterium abscessus</i>
<i>M. smegmatis</i>	<i>Mycobacterium smegmatis</i>
<i>P. aeruginosa</i>	<i>Pseudomonas aeruginosa</i>
<i>A. baumannii</i>	<i>Acinetobacter baumannii</i>

Chapter 1 Mechanisms of ribosome recycling in bacteria: a structural perspective¹

Chapter adapted with permission from Seely S.M., Gagnon M.G. Mechanisms of ribosome recycling in bacteria and mitochondria: a structural perspective. *RNA Biol.* 2022;19(1):662-677. doi: 10.1080/15476286.2022.2067712.¹

1.1 Bacterial Translation

In all organisms, the genetic information in messenger RNAs (mRNAs) is decoded and translated into proteins by a universally conserved macromolecular machine, the ribosome. The bacterial ribosome is composed of ~4,500 nucleotides and more than 50 ribosomal proteins, which assemble into a 70S ribosome made of two subunits, the small (30S) and the large (50S) subunits. The translation cycle is divided in four steps, initiation, elongation, termination, and recycling. Each step requires its own set of translation factors which interact with the ribosome in a sequential manner to control the accuracy and rate of protein synthesis.

The initiation complex begins with the 30S subunit, which binds the mRNA and selects the start codon positioned into the peptidyl (P) site. Assisted by initiation factors IF1, IF2, and IF3, the initiator fMet-tRNA^{fMet} binds the P site with high affinity and base pairs with the AUG codon on the mRNA². Joining of the 50S subunit is catalyzed by IF2, a GTPase that regulates the maturation of the 70S initiation complex into an elongation-competent ribosome^{3, 4}. Following dissociation of initiation factors, the ribosome is now programmed with the initiator fMet-tRNA^{fMet} in the P site and the first codon in the mRNA resides in the aminoacyl (A) site. The elongation cycle begins with the delivery of an aminoacyl-tRNA (aa-tRNA) by EF-Tu⁵. Decoding of the A-site codon stimulates hydrolysis of GTP by

EF-Tu, which releases aa-tRNA into the A site⁶⁻⁸. After peptide bond formation, translocation of mRNA and tRNAs is catalyzed by elongation factor G (EF-G) and GTP^{5, 9-13}. Through a series of conformational changes in EF-G¹⁴⁻¹⁶ and in the ribosome, including head swiveling of the 30S subunit¹⁷⁻²⁰ and ribosome ratcheting^{9-11, 21}, tRNAs are translocated by one codon after each amino acid addition to the nascent polypeptide chain. Finally, the stop codon is recognized by release factors RF1 or RF2²²⁻²⁷. Recognition of the stop codon triggers a conformational change in the release factor from its compact to extended conformation which allows its GGQ domain to dock into the peptidyl transferase center (PTC) near the nascent peptide chain attached to the peptidyl-tRNA in the P site, triggering hydrolysis and release of the complete protein [21–26]. Release factor 3 (RF3), found in a broad range of bacteria including *Escherichia coli*, facilitates the removal of RF1/RF2 from the ribosome²⁸⁻³⁰. The termination complex is then recycled into individual ribosomal subunits by EF-G, GTP, and the ribosome recycling factor (RRF)³¹⁻³⁴.

Over the last two decades, structures of key ribosome complexes have been elucidated with the use of X-ray crystallography and cryo-electron microscopy (cryo-EM), providing important insights into the mechanisms of protein synthesis. While the steps of initiation, elongation, and termination have received considerable attention, structures of ribosome complexes undergoing recycling remain relatively scarce. The lack of high-resolution structures of functional ribosome complexes before and after subunit splitting has impeded our understanding of this essential step of protein synthesis. In this chapter, the current

state of understanding of ribosome recycling that emanated from the structures of bacterial ribosomes complexed with recycling factors is described.

1.2 RRF is a structural mimic of tRNA

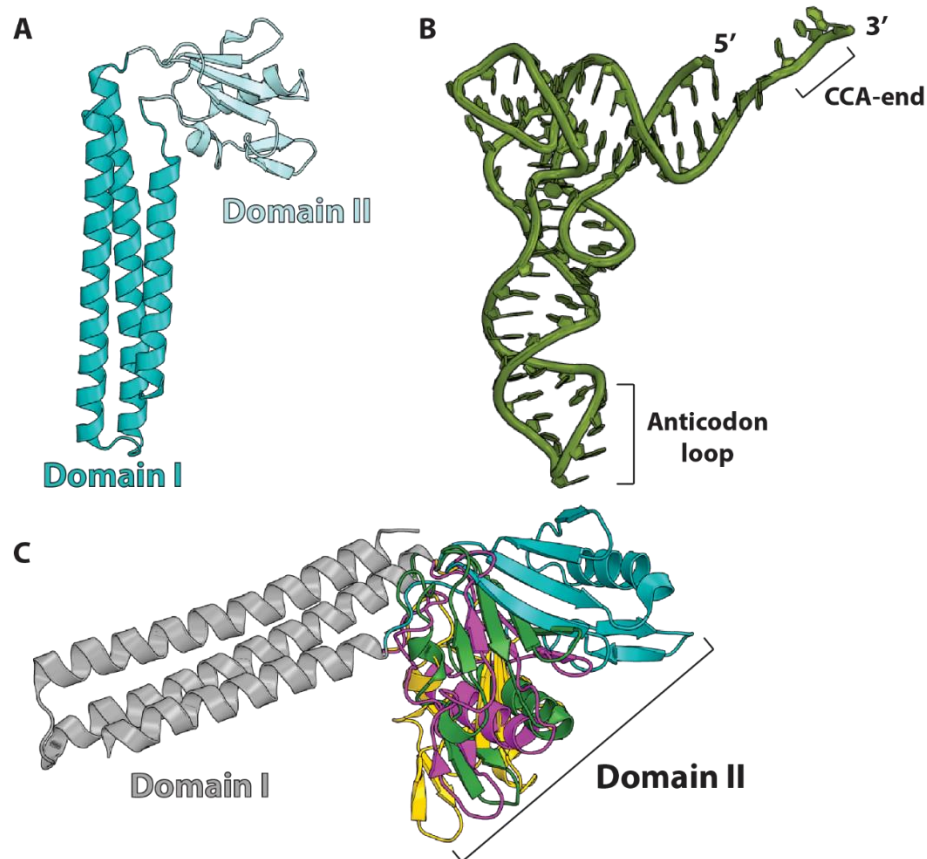


Figure 1.1 RRF is a tRNA mimic with a flexibly disposed domain II. (A) Ribbon diagram of the *E. coli* RRF crystal structure (PDB 1EK8)³⁵. Domains I and II are distinctly colored and connected by flexible linkers. (B) L-shaped structure of tRNA. (C) Crystal structures of RRF aligned by domain I show that domain II rotates about the axis of domain I (PDBs: 1EK8, teal; 1DD5, gold; 1EH1, green; 1GE9, magenta)³⁵⁻³⁸.

In bacteria, EF-G is typically a dual function protein that in addition to catalyzing tRNA and mRNA translocation, also promotes ribosome recycling. Ribosome recycling by EF-G requires RRF, the inactivation of which was shown to be lethal in *E. coli*^{39, 40}. It was initially proposed that RRF binds to the A site of the ribosome, similarly to release factors RF1 and RF2⁴¹. Crystal and solution NMR

structures of RRF revealed that its fold mimics that of the tRNA L-shape³⁵⁻³⁸. RRF consists of two domains, a long triple α -helix coil-coil bundle domain (domain I), and a smaller α/β domain (domain II) (Figure 1.1A, B). Alignment of the RRF structures through the triple-helix bundle domain I reveals that both domains in RRF are linked through flexible linkers, allowing domain II to freely rotate around the long axis of domain I^{35, 42} (Figure 1.1C). Domain swapping experiments in RRF demonstrated that domain II plays a crucial role in recycling the ribosome presumably through its interaction with EF-G⁴³. Hydroxyl radical probing of RRF bound to the *E. coli* 70S ribosome suggested that despite the fact that the structure of RRF mimics that of tRNA, the orientation of RRF in the ribosome differs significantly from the binding position of tRNA⁴². The model proposed that the long triple helix bundle domain I of RRF binds across the A and P sites on the large subunit (LSU), thereby overlapping with the positions of the acceptor arms of the A- and P-site tRNAs in the 70S ribosome.

The first cryo-EM reconstruction of the 70S ribosome bound to RRF provided, albeit at a low-resolution, a glimpse of the binding site of RRF at the interface of the subunits of the ribosome⁴⁴. The structure essentially confirmed the previous binding position of RRF inferred from hydroxyl radical probing protection experiments⁴², placing domain II further toward the small subunit (SSU), and revealed conformational changes in the inter-subunit bridge B2a that is formed between helix H69 of 23S rRNA and the top of helix h44 of 16S rRNA. This cryo-EM structure provided a rationale for the role of RRF in facilitating dissociation of the ribosomal subunits. Helix 69 plays a functional role in many steps of protein

synthesis, including subunit association and tRNA binding. Large ribosomal subunits lacking helix H69 are unable to associate with the small subunits to form functional ribosomes, and the assembled 70S ribosome can be recycled in the absence of RRF, demonstrating the importance of bridge B2a for the stability of the 70S ribosome⁴⁵. In agreement with the disruption of bridge B2a during ribosome recycling, a crystal structure of the *Deinococcus radiodurans* 50S subunit complexed with domain I of RRF showed that the tip of H69 moves by 20 Å toward h44 of the SSU⁴⁶. However, the physiological relevance of the 50S-RRF crystal structure raised doubts because RRF itself preferably binds to the 70S ribosome over the 50S subunit^{47, 48}. Furthermore, RRF bound to the 50S subunit is not released by EF-G, the latter being required for efficient ribosome recycling⁴⁹.

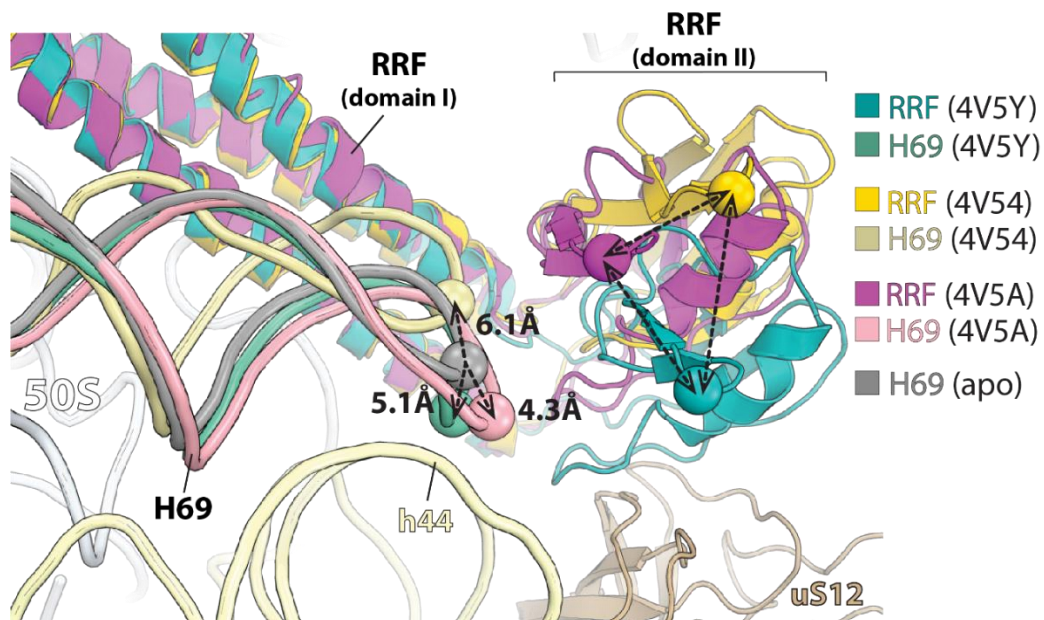


Figure 1.2 Domain II of RRF is flexibly disposed on the 70S ribosome. Crystal structures of RRF on the 70S ribosome aligned by 23S rRNA. In the absence of EF-G, domain II of RRF occupies different positions relative to the 23S rRNA helix H69 (PDBs: 4V5Y, *E. coli* 70S-paromomycin-RRF; 4V54, *E. coli* 70S-RRF; 4V5A, *T. thermophilus* 70S-RRF)^{33, 34}.

The crystal structure of the *Thermus thermophilus* 70S ribosome bound to RRF showed that under the experimental conditions used, RRF does not induce H69 movement³³. On the contrary, the crystal structures of the *E. coli* 70S bound to either *T. thermophilus* or *E. coli* RRF reported that RRF induces H69 movement away from the SSU h44^{32, 34} (Figure 1.2). The apparent discrepancy observed in the movement of H69 among the ribosome-RRF complex structures may be attributed to the absence of EF-G in these experiments. EF-G is required for RRF-mediated ribosome recycling and its influence on the conformation of RRF and the ribosome must account for its function.

The ribosome is known to fluctuate between the ratcheted and non-ratcheted conformations. This refers to the rotation of the SSU relative to the LSU in the 70S ribosome. The ratcheting motion of the ribosome is thermally driven in that the ribosome can spontaneously sample both rotated and non-rotated conformations⁵⁰ and occurs in the absence of factor^{51, 52}. However, these fluctuations do not lead to productive translocation in the absence of EF-G. EF-G bound to GTP induces the rotated conformation of the ribosome²¹, which is required for mRNA and tRNA translocation. However, the state of the ribosome to which RRF binds has remained unclear as cryo-EM and single molecule Förster resonance energy transfer (smFRET) experiments demonstrated that the association of RRF with a post-termination 70S ribosome containing a deacylated tRNA in the P site induces the ribosome to adopt the rotated state⁵³⁻⁵⁵. In agreement with RRF binding to the 70S ribosome following peptide release, RRF has low affinity for the non-rotated ribosome containing peptidyl-tRNA in the P

site⁵⁶. The crystal structure of RRF bound to a fully rotated *E. coli* 70S ribosome reported essentially the same interactions between domain I of RRF and the ribosome as with the non-rotated ribosome, while domain II interacts with ribosomal protein uS12 and is more constrained in the rotated ribosome⁵⁷. In this structure, the acceptor stem of the deacyl-tRNA has moved to the E site of the LSU and the tRNA is bound in the p/E hybrid position due to SSU rotation, which effectively avoids a steric clash between the triple helix bundle domain I of RRF and the acceptor stem of deacyl-tRNA (Figure 1.3A). The orientation of domain II on the rotated ribosome suggests that RRF must undergo large rearrangements to co-exist on the ribosome together with EF-G (Figure 1.3B). The presumed rotation of domain II in RRF induced by EF-G would lead to conformational changes in regions of the 50S subunit that are involved in inter-subunit bridging (e.g. bridge B2a).

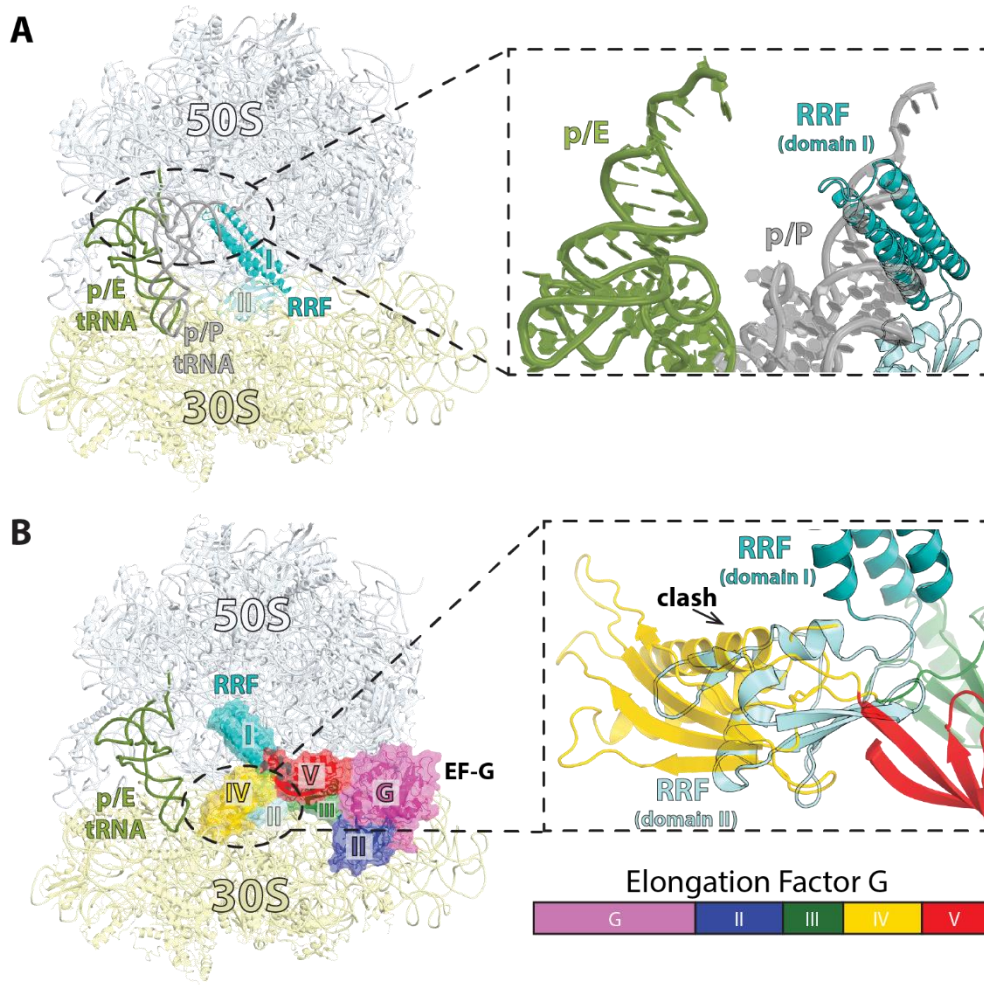


Figure 1.3 RRF in the post-termination complex (PoTC) is not compatible with tRNA in the p/P state of binding and EF-G on the 70S ribosome. (A) RRF (teal/light blue) bound to the 70S ribosome with p/E-tRNA (olive) (PDB 4V9D⁵⁷). The p/P-tRNA (gray) is shown. Inset: Domain I of RRF clashes with tRNA bound in the p/P state. (B) Structure of EF-G-GDP/PCP in the extended state bound to the 70S ribosome (PDB 4V5F⁵). EF-G is colored by domain according to the bar chart. Inset: Domain IV of EF-G in the extended conformation is not compatible with RRF without further rotation of RRF domain II about the long-axis of domain I.

The presence of mRNA and deacyl-tRNA on the post-termination ribosome was shown to increase the rate of subunit splitting by the concerted action of RRF and EF-G⁵⁸. Yet, the structure with RRF bound to the rotated ribosome and deacyl-tRNA in the p/E hybrid state fails to explain how deacyl-tRNA facilitates subunit splitting. For instance, the same p/E-tRNA hybrid state is observed during EFG-

mediated tRNA translocation, which does not lead to ribosome subunit dissociation. Until recently, little remained known of the interactions that form between RRF and EF-G on the pre-recycling 70S ribosome, and the role of deacyl-tRNA in subunit splitting.

1.3 The concerted action of EF-G and RRF recycles the ribosome

EF-G and RRF act together to split the post-termination 70S ribosome into its individual subunits. It was proposed that IF3 also acted as a ribosome splitting factor⁴⁷. However, further experiments confirmed that IF3 is not required for ribosome splitting, but rather associates with free 30S subunits and serves the role of an anti-association factor, keeping SSU from re-associating with free LSU^{59, 60}.

RRF bound to the ribosome without EF-G is observed to occupy two locations at the interface of the subunits, one that is same as previously determined, and a new position exclusively on the 50S subunit overlapping with that of tRNA in the P site⁶¹. Although the low-resolution cryo-EM structure suggested that RRF may 'spontaneously' move across the inter-subunit space disrupting contacts between the ribosomal subunits, the action of EF-G during recycling remained unclear. The lack of structures of pre-recycling 70S ribosome complexed with both RRF and EF-G is due to the rapid splitting of the ribosome ($\sim 5 \text{ sec}^{-1}$ *in vivo*) by these two factors⁶². Structural studies rely on the formation of stable complexes with lifetimes that are compatible with the experimental approach used to visualize it. Crystallization of the ribosome is a time-consuming process and complexes that are not stable enough represent a challenge for

structure determination using X-ray crystallography⁶³⁻⁶⁶. The technique of cryo-EM represents an advantage over crystallography in that it bypasses the crystallization step and can be used to capture structural intermediates and less stable complexes. The recent 'resolution revolution' in cryo-EM has opened a realm of new possibilities enabling visualization of large protein machineries at near-atomic resolution, which is essential to the understanding of how nanomachines function. The use of cryo-EM has been fueled by developments of transmission electron microscopes optics, software for data analysis, and sensors that combine fast readouts with the ability to directly detect electrons^{67, 68}. Ribosome complexes are assembled, applied to a holey-mesh carbon grid, flash-frozen in a thin film of vitreous ice, and single particles are visualized by electron microscopy (EM). Time-resolved cryo-EM is being developed and shown to be valuable to capture short-lived intermediates of ribosome complexes undergoing fast transitions, allowing reconstructions of functionally relevant transient structures^{4, 8, 13, 22, 31, 69}.

The first structure of a post-termination ribosome in complex with both RRF and EF-G used heterogeneous factors and ribosome. Cryo-EM was used to reconstruct structures of a complex containing the 70S ribosome and EF-G from *E. coli*, and RRF from *T. thermophilus*⁷⁰. The structures revealed new interactions between domain II of RRF and the ribosome in the absence of EF-G, forming contacts with helices H43 and H44 in the uL11-stalk of the 23S rRNA, part of the GTP-activating center (GAC). With EF-G bound, domain II of RRF rotates towards the 30S subunit, locating in the vicinity of inter-subunit bridge B2a as observed in other structures. The interpretation of these results was, however, obscured by the

fact that this heterogeneous combination of factors is inactive in ribosome recycling^{71, 72}.

Time-resolved cryo-EM was used to trap the ribosome incubated with RRF, EF-G and IF3 during subunit splitting³¹. The ribosome was rapidly mixed with RRF, EF-G and IF3, and the grids frozen. At the 140 ms reaction time point, four types of complexes were observed. The first class shows rotated 70S bound to RRF and with tRNA in the p/E state. In this complex, domain II of RRF is in contact with protein uS12 as observed in the crystal structure of rotated E. coli 70S ribosome bound to RRF⁵⁷, contrary to the heterogeneous complex in which domain II orients toward the 50S subunit⁷⁰. The second class contains RRF bound to the non-rotated ribosome without tRNA. Compared to the rotated ribosome, domain II interacts with the stalk base (GAC) of the 50S subunit, reminiscent to the interaction previously described for the recycling complex formed with heterogeneous factors⁷⁰. However, it was suggested that this class is not an authentic intermediate in the recycling process due to the lack of tRNA in the map. The third class has both EF-G and RRF bound to a rotated ribosome with a tRNA in the p/E state. The low resolution of these structures (~7.5–16 Å) makes it difficult to unambiguously determine the location of domain II of RRF because its density appears fused with that of EF-G. Yet, the angle between domains I and II decreased by ~60° as domain II rotates toward helix h44 of SSU and loses interaction with protein uS12. Domain IV of EF-G, the A-site binding domain during tRNA translocation, is seen to contact domain II of RRF, while domain III of EF-G is unresolved in this map. As expected from the ribosome splitting reaction,

individual 30S and 50S subunits were also observed. The SSU is either bound to tRNA or IF3, and the LSU remains associated with EF-G and RRF. On the LSU, domain I of RRF occupies the same position as that seen on the 70S-RRF and 70S-RRF-EF-G complexes. Domain II, however, is rotated even further toward helix H69 of 23S rRNA when compared to the 70S-RRF-EF-G complex. Taken together, these results corroborated previous observations indicating that EF-G assists the movement of domain II of RRF towards bridge B2a and jointly acts with RRF to split the post-termination complex into individual subunits.

The structures described above provided important insights into the mechanism of ribosome splitting by RRF and EF-G. Yet, the role of tRNA in facilitating this process remained unclear. In all of the recycling complexes that carry a tRNA the same p/E hybrid conformation was observed. The hybrid p/E state of tRNA binding occurs all the time during EF-G-mediated tRNA translocation and even just when the ribosome spontaneously takes the rotated state. Thus, how can the rate of subunit splitting by RRF and EF-G be 15- fold faster with tRNA bound to the post-termination ribosome⁵⁸? The crystal structure of a pre-recycling complex bound to RRF, EF-G, and two tRNAs provided a plausible explanation to this conundrum⁶³. In this study EF-G bound to GDP stabilizes the ribosome in a non-rotated state complexed with RRF and tRNAs in the P and E sites. As expected, domain I of RRF occupies the same position as previously seen on the non-rotated *E. coli* and *T. thermophilus* 70S ribosome^{33, 34}. The position of the acceptor stem of P-site tRNA is not compatible with the simultaneous binding of RRF domain I on the 50S subunit (Figure 1.3A). Consequently, the deacyl-tRNA is

tilted toward the E site and the CCA-end is located halfway between the P and E sites on the 50S subunit (Figure 1.4A, C). The CCA-end of the p/R-tRNA is blocked by a constriction formed by helices H74 and H80 of 23S rRNA (Figure 1.4D). The 3'-terminal nucleotides of tRNA are crunched together, suggesting that the tension that builds up in tRNA may facilitate subunit splitting. This data supports the notion that, despite the absence of tRNA translocation during ribosome recycling^{73, 74}, splitting of the ribosome proceeds rapidly in the presence of deacyl-P-site tRNA^{58, 74}. Correspondingly, RRF interacts weakly with translating ribosomes carrying peptidyl-tRNA in the P site⁵⁶, and EF-G and RRF do not dissociate such ribosomes⁷⁴.

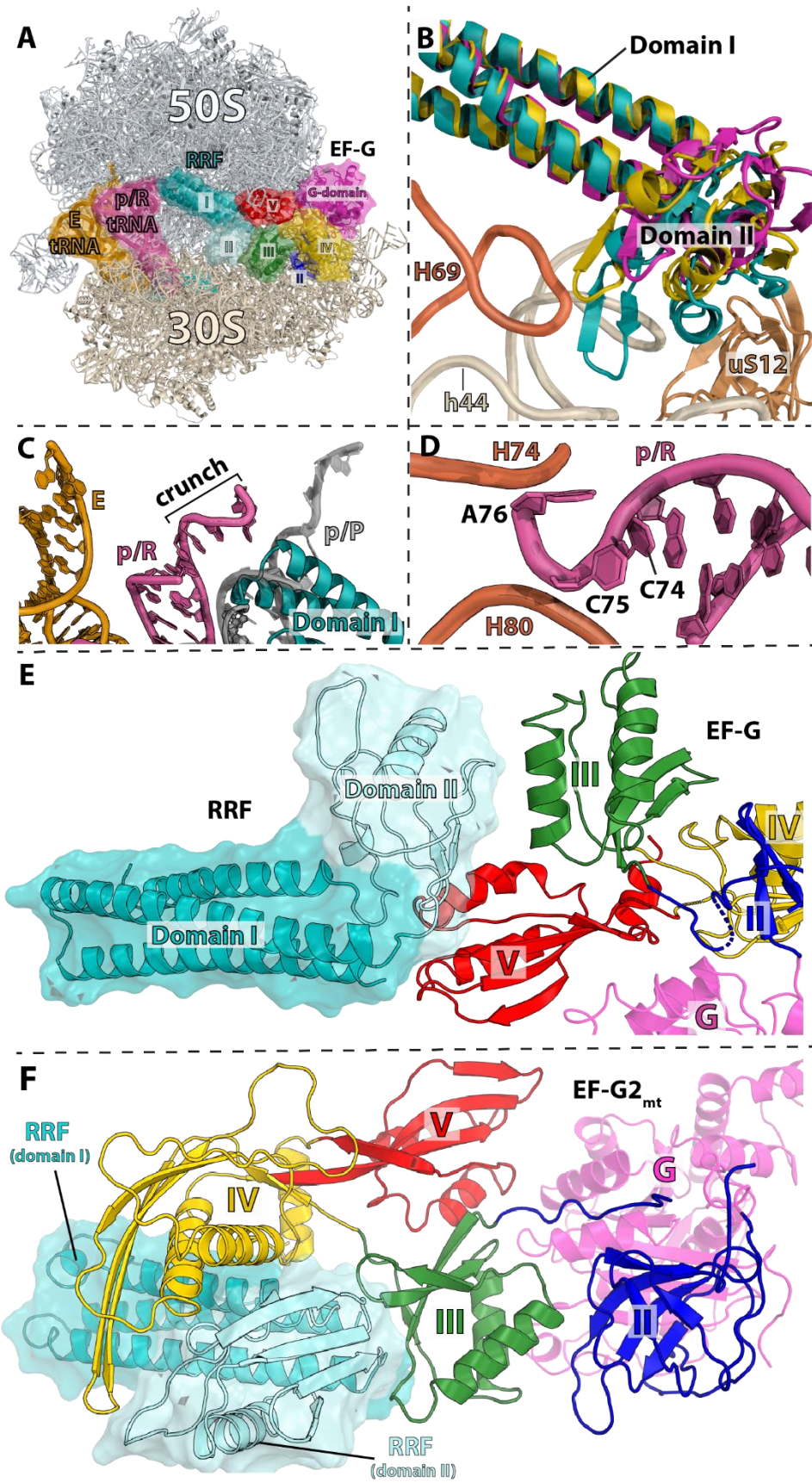


Figure 1.4 Pre-recycling complex with p/R- and E-site tRNAs. (A) Overview of pre-recycling complex (PDB 6UCQ⁶³) with E-site tRNA (orange), p/R-tRNA (pink), RRF (teal and light blue), and EF-G in the compact state (colored by domain). (B) RRF domain II positioned in a 'ready-to-attack' state. Domain II (teal) locates in the niche created by H69 (orange), h44 (cerium), and uS12 (brown). RRF from crystal structures in the absence of EF-G superimposed through domain I of RRF (PDBs 4V5A, gold; 4V55, magenta)^{33, 34}. (C) Close-up view of the tRNA interaction with RRF domain I wherein the p/R-tRNA CCA-end is crunched and displaced by ~22 Å toward the E site and exhibits shape complementarity with RRF. The classical p/P-tRNA is not be compatible with RRF on the 70S ribosome. (D) The CCA-end of the p/ R-tRNA is squeezed between 23S rRNA helices H74 and H80 (orange). (E) Interactions between compact EF-G and RRF. Domain II of RRF interacts favorably with EF-G domains III and V. (F) Interactions between RRF_{mt} and EF-G_{2mt} in the post-recycling complex (PDB 7L20⁷⁵) wherein EF-G_{2mt} has undergone rearrangements of domains III, IV and V. Domain IV of EF-G_{2mt} forms favorable interactions with the surface of RRF_{mt} domain II, which has rotated to avoid a steric collision with EF-G.

The presence of EF-G in this crystal structure complex causes domain II of RRF to rotate toward helix H69 of 23S rRNA as seen by time-resolved cryo-EM³¹. Compared to the crystal structures of RRF-70S complexes^{33, 34}, EF-G pushes domain II deeper into the space formed between H69 and ribosomal protein uS12, suggesting a 'ready-to-attack' state of RRF on the central bridge B2a (Figure 1.4B). In this pre-recycling complex, EF-G adopts a compact conformation identical to the one previously reported on a pre-translocation 70S ribosome¹⁶. In this conformation, domain IV of EF-G is directed away from RRF, and domains III and V of EF-G form a cleft into which RRF domain II docks⁶³. In the previous cryo-EM structures of the 70S-RRF-EF-G³¹ and 50S-RRF-EF-G^{53, 76}, domain IV of EF-G lies on top of RRF. One major difference is that in the 70S-RRF-EF-G structure³¹, the ribosome is rotated. Thus, EF-G would presumably undergo a large conformational rearrangement from the compact to the extended form as the ribosome transitions to the rotated state (Figure 1.4E, F).

The compact form of EF-G is likely transient, being trapped on the ribosome because of the intermolecular contacts in the crystal that lock the ribosome in the non-rotated state. The rapid transition of the ribosome to the rotated state in solution makes compact EF-G difficult to capture by cryo-EM. SmFRET experiments suggested the existence of a compact EF-G on the ribosome¹⁴, and a low-resolution cryo-EM reported large domain movements in EF-G on the ribosome¹⁵. Despite this, recent time-resolved cryo-EM studies of EF-G bound to the 70S ribosome during tRNA translocation did not observe the compact form of EF-G^{12, 13, 77}, further suggesting that it is not a ribosome-EF-G state that is highly populated. EF-G in its extended conformation interacts with RRF on the post-termination 70S complex; however, the low-resolution of the available cryo-EM studies limits the interpretation of the specific contacts between EF-G and RRF, and with the ribosome. Structures of pre-recycling ribosome complexes determined at higher resolution are required for a better understanding of ribosome recycling.

1.4 Select bacteria harbor multiple copies of EF-G

The genome of several bacteria contains more than one copy of the gene encoding for EF-G^{78, 79}. However, there are limited studies into the function and mechanism of these additional homologues. EF-G2 in *T. thermophilus* exhibits ribosome dependent GTPase activity and low levels of elongation activity in poly(U)-dependent protein synthesis while its possible role in recycling remains unclear⁸⁰. The function of EF-G2 in *Mycobacterium smegmatis* remains ambiguous due to the lack of GTPase activity which renders it unable to participate

in elongation or recycling⁸¹. *Borrelia burgdorferi* EF-G1 and EF-G2 have been determined to have specific singular activity rather than being bi-functional, wherein EF-G1 functions exclusively in elongation and EF-G2 functions exclusively with RRF in recycling, similarly to the suggested specific activity for the EF-G1A and EF-G1B homologues identified in *Pseudomonas aeruginosa*^{82, 83}. Currently, it remains difficult to derive conclusions regarding the specialization of EF-Gs in bacteria due to the absence of structural information. High-resolution structures of bacterial ribosomes complexed with specialized EF-Gs will be required to understand how specific forms of EF-G function exclusively during elongation while other forms work concomitantly with RRF during ribosome recycling.

1.5 Some aminoglycosides inhibit ribosome recycling

Antibiotics are an essential tool to combat bacterial infections, and many antibiotics inhibit ribosome function by targeting the functional centers of the ribosome, the PTC and DC. Most commonly, these small molecules inhibit the elongation step of protein synthesis by or induce dysfunction that results in errant protein production. One class of antibiotics, aminoglycosides, such as arbekacin, amikacin, paromomycin and neomycin have a broader inhibition profile including the inhibition of termination and ribosome recycling⁸⁴⁻⁹¹. While the development and study of aminoglycosides has been focused on their primary binding site in the decoding center, which is known to introduce miscoding effects on translation, it remains to be elucidated how this binding site inhibits recycling by EF-G and RRF.

In the case of neomycin, x-ray crystallography has shown that in addition to the decoding center neomycin also binds the ribosome in the large subunit adjacent to the critical inter-subunit bridge³⁴. This secondary binding site was determined to reduce the ability of EF-G and RRF to disrupt the contacts between H69 and h44 during the recycling step³⁴. For aminoglycosides such as amikacin, which has been one of the most successfully used antibiotics against infectious pathogens such as *Pseudomonas aeruginosa*, there is a lack of structural studies that would explore potential secondary binding sites on the ribosome that would elucidate its mechanism of inhibition on the recycling process⁹¹⁻⁹³. Inhibition of recycling by aminoglycosides requires more structural and biochemical studies to understand their different inhibition profiles. Renewed interest in these antibiotics as a response to the rise in antibiotic resistance is an important avenue to improvement of current antibiotics and development of new antibiotics that are more effective.

1.6 HflX is an alternative ribosome recycling factor

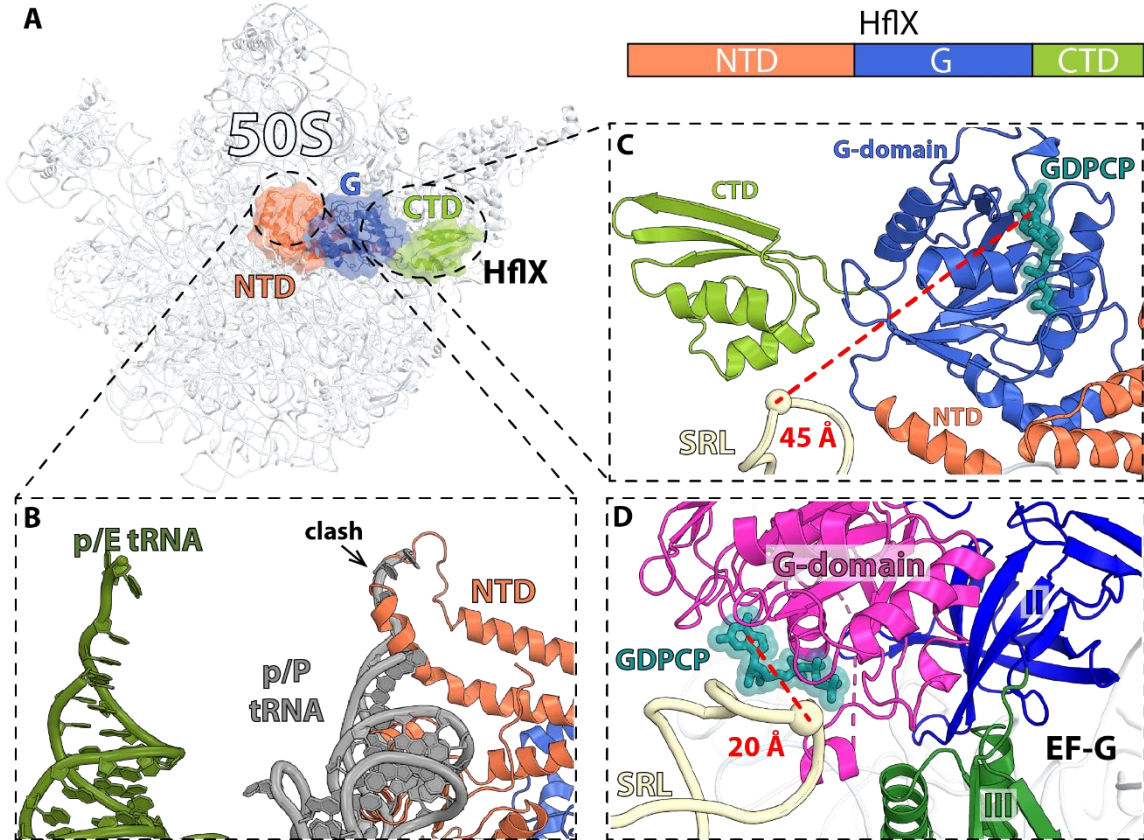


Figure 1.5 Cryo-EM structure of *E. coli* 50S subunit bound to HflX. (A) Overview of *E. coli* HflX bound to the 50S subunit (PDB 5ADY⁹⁴). (B) Close-up view of the HflX N-terminal domain with superimposed p/P- and p/E-tRNAs showing that the p/P-tRNA is not compatible with HflX. (C) The GDP nucleotide in the G-domain of HflX locates ~45 Å away from the 23S rRNA sarcin-ricin loop (SRL). (D) In EF-G-GDP bound to the 70S ribosome, the GDP nucleotide in the G-domain is closer (~20 Å) to the SRL (PDB 4V9H⁹).

In bacteria, HflX is one of the 11 conserved GTPases and shares high sequence homology with the ODN protein family (Obg, DRG1 and Nog1) involved in ribosome assembly⁹⁵. Like the ODN family proteins, HflX binds to LSU in a nucleotide dependent manner, including GTP, GDP, ATP, and ADP⁹⁶⁻⁹⁸. However, only the GTP-hydrolysis activity of HflX is stimulated upon ribosome binding⁹⁶. Yet, under conditions that favor regeneration of nucleotide diphosphate into triphosphate forms, it was shown that ATP hydrolysis by HflX is stimulated by the

70S ribosome and free 50S subunits⁹⁹. Despite being universally conserved, HflX is dispensable in *E. coli* under normal growth conditions¹⁰⁰. The *hflX* gene is part of a complex superoperon, *amiB-mutL-miaA-hfq-hflX-hflK-hflC*, characterized by genes that are co-transcribed from a series of alternating $E\sigma 70$ and $E\sigma 32$ heat shock promoters^{101, 102}. The relative amount of *hflX* transcript increases ~5-fold in cells undergoing heat shock¹⁰¹. HflX rescues stalled ribosomes during early elongation steps¹⁰³ and rapidly restores translational capacity to the cell during heat shock response. HflX in *E. coli* has been described to rescue stalled ribosomes by splitting the 70S ribosome into subunits, effectively recycling them at a rate that is around 5-fold slower than that with EF-G, RRF, and IF3⁹⁴. HflX exhibits a three-domain structure; the GTPase domain, the C-terminal domain (CTD), and the N-terminal domain (NTD) that is made up of two sub-domains⁹⁴. While chemical crosslinking experiments have previously suggested that HflX binds near the ribosomal E site, structure determination by cryo-EM showed that HflX binds along the subunit interface covering the A site and overlapping with the P site (Figure 1.5A)^{94, 104}. HflX binding in this position would clash with a peptidyl-tRNA in the P site and accounts for the observed lower splitting efficiency when a peptidyl-tRNA is present in the 70S (Figure 1.5B)⁹⁴. However, a deacyl-tRNA in the p/E-hybrid position would be accommodated and therefore, it is likely that HflX has preferential binding for a rotated ribosome similar to RRF and EF-G⁹⁴. When in complex with the 50S subunit, and unlike other GTPases, the G-domain of HflX is positioned in such a way that it does not contact the sarcin-ricin loop (SRL) of the 50S subunit, suggesting that GTPase activation in HflX occurs by a completely

different mechanism compared with other translational GTPases^{94, 96, 99} (Figure 1.5C, D). Structure alignment of the 50S:HflX:GDPNP cryo-EM reconstruction with the 50S subunit of the 70S ribosome shows that HflX causes rearrangements of H69 in LSU such that it would collide with the SSU h44 (Figure 1.6B). This suggests that similar to canonical recycling by EF-G and RRF, disruption of the contact between H69 and h44 is used by HflX to dissociate the 70S ribosome. However, structures of HflX in complex with the 70S ribosome will be necessary to elucidate this further.

Recently, HflX homologues in *Mycobacterium abscessus* and *M. smegmatis* have been associated with resistance to lincosamide and macrolide antibiotics^{105, 106}. Expression of *M. abscessus* and *M. smegmatis* is under the control of the *WhiB7* transcriptional activator which upregulates the expression of the *erm* genes in the presence of sub-inhibitory concentrations of antibiotics^{107, 108}. HflX-ribosome dependent splitting was also observed in these species; however, HflX was unable to prevent H³-erythromycin (ERY) from binding to the ribosome or remove it from the LSU¹⁰⁶. The NTD of HflX extends toward the PTC, with the tip of the NTD located ~12.3 Å from erythromycin bound deeper into the nascent peptide exit tunnel (NPET), which may explain why HflX fails to dislodge ERY from the LSU (Figure 1.6A). It was suggested that HflX alone is not sufficient to mediate antibiotic resistance and that a second factor may be required to remove the bound antibiotic from the 50S subunit before it can undergo a new round of translation¹⁰⁶.

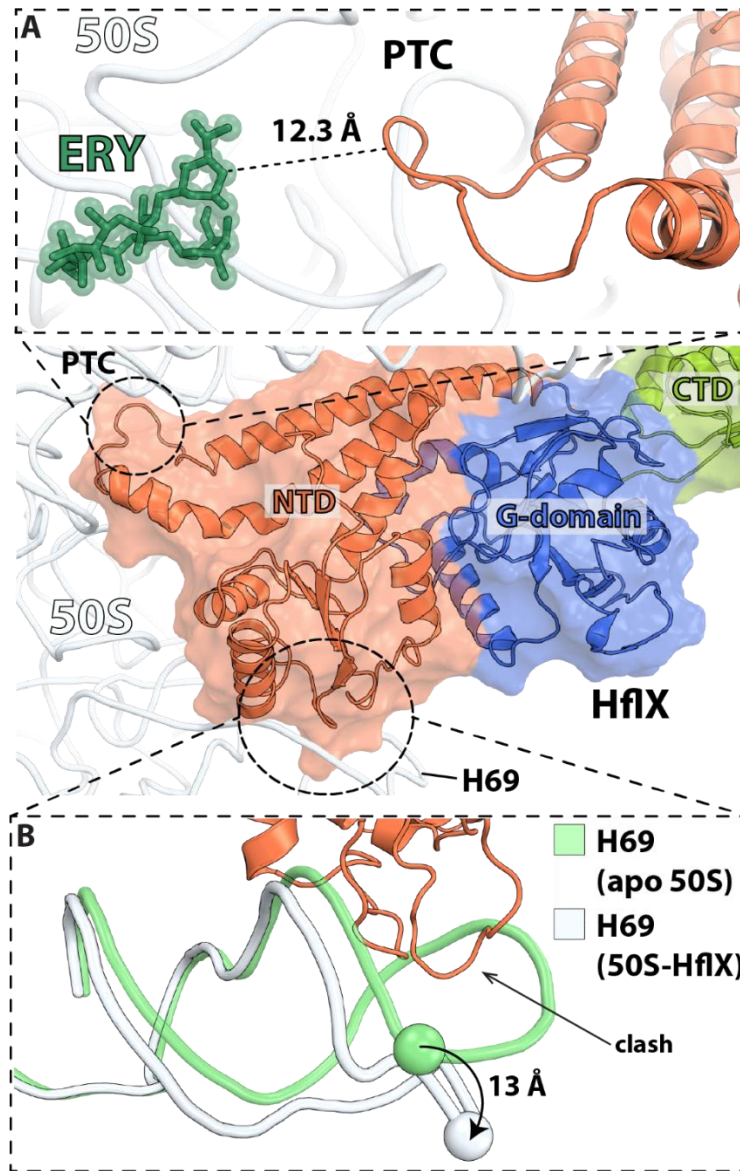


Figure 1.6 Interactions of HflX with the 50S ribosomal subunit. (A) Close-up view of the PTC loop within the HflX N-terminal domain (orange) (PDB 5ADY⁹⁴) with the antibiotic erythromycin (ERY) (green) bound in the nascent peptide exit tunnel (NPET) (PDB 6ND6¹⁰⁹). The nearest distance between HflX and ERY is more than 12 Å. (B) The N-terminal domain of HflX (orange) displaces 23S rRNA helix H69 by ~13 Å (white) relative to the apo form (green) of the 50S subunit.

Listeria monocytogenes carries two *hflX* genes, and one was named *hflXr* because its expression is associated with resistance to lincomycin and ERY. The *hflXr* gene is under the control of the *rli80* leader sequence and when exposed to lincomycin the transcription of *hflXr* significantly increases due to transcription

attenuation control of *rli80* associated genes¹¹⁰. Deletion of the *hflXr* gene leads to increase sensitivity to lincomycin and ERY while its over-expression increases resistance. HflXr is proposed to recycle antibiotic-stalled 70S ribosomes because they accumulate in *hflXr* knockout cells exposed to sub-lethal concentrations of ERY¹¹⁰. High-resolution structures of HflX/HflXr in complex with the 70S ribosome and 50S subunit are needed to elucidate the mechanism by which HflX recycles stalled ribosomes. Additionally, clarity is needed as to how HflX and HflXr mediate resistance through ribosome recycling and what additional factors may be involved in the prevention of antibiotic binding or antibiotic removal from the 50S subunit.

1.7 Concluding remarks

Structures of the ribosome complexed with canonical and alternative splitting factors have contributed to the molecular understanding of ribosome recycling. One common theme emerges: bacterial ribosome recycling factors destabilize the central inter-subunit bridge formed between h44 in the small subunit and helix H69 in the large subunit. While conformational changes in RRF domain II that displace helix H69 are induced by EF-G, the N-terminal domain of HflX performs this function. Nevertheless, the significance of displacing H69 can only be speculated at this time in the absence of high-resolution structures of pre-recycling ribosomes complexed with recycling factors. Similarly, the molecular basis by which HflX-mediated ribosome recycling is associated with antibiotic resistance in *L. monocytogenes*¹¹⁰ and *M. abscessus*^{105, 106} requires further analysis. Additionally, further characterization of aminoglycoside antibiotics and their role in inhibition of ribosome recycling is an essential component to

understanding ribosome function and development of new therapeutics effective in treating resistant bacteria.

Chapter 2 Molecular basis of the pleiotropic effects by the antibiotic amikacin on the ribosome¹¹¹

Chapter adapted with permission from Seely S.M., Parajuli N.P., De Tarafder A., Ge X., Sanyal S., Gagnon M.G. Molecular basis of the pleiotropic effects by the antibiotic amikacin on the ribosome. *Nat Commun.* 2023 Aug 3;14(1):4666. doi: 10.1038/s41467-023-40416-5.¹¹¹

2.1 Introduction

Antibiotics are an important arsenal used to treat bacterial infections. The majority of antibiotics inhibit protein synthesis by targeting the ribosome, the molecular machine responsible for decoding messenger RNAs (mRNAs) and correspondingly incorporating incoming amino acids into the nascent polypeptide chain. Structural studies of the ribosome in complex with antibiotics revealed that translation inhibitors generally target functional centers of the prokaryotic ribosome, the decoding center in the small (30S) subunit, and the peptidyl transferase center as well as the nascent peptide exit tunnel in the large (50S) subunit¹¹². Aminoglycosides are broad-spectrum bactericidal antibiotics used to treat a wide spectrum of infections caused by Gram-negative pathogenic bacteria. The most common clinically used aminoglycosides harbor the central 2-deoxystreptamine (2-DOS) ring joined by glycosidic linkages with amino sugars. They interfere with protein synthesis by targeting the region of 16S ribosomal RNA (rRNA) helix h44 forming the decoding center within the 30S subunit of the ribosome (Figure 2.1a, inset 1). Binding of 2-DOS-containing aminoglycosides to the decoding center displaces two universally conserved nucleotides, A1492 and A1493, promoting their interaction with the minor groove of the codon-anticodon duplex in the aminoacyl (A) site of the ribosome. This “ready-to-accept”

conformation of the decoding center promotes the binding of near-cognate aminoacyl-tRNAs, thereby inducing translational errors⁸⁴⁻⁹¹.

The nature of the 2-DOS core ring structure and types of chemical substitutions allow to broadly classify aminoglycosides into four subclasses: (i) no 2-DOS (e.g. streptomycin), (ii) mono-substituted 2-DOS (e.g. apramycin), (iii) 4,5-di-substituted 2-DOS (e.g. neomycin, paromomycin), and (iv) 4,6-di-substituted 2-DOS (e.g. gentamicin, kanamycin, tobramycin)⁹². Despite their similar chemical structures, aminoglycoside antibiotics exert pleiotropic effects on ribosome function. For instance, neomycin and paromomycin, both belonging to the 4,5-di-substituted subclass, promote 30S subunit rotation in the opposite direction relative to the usual ratcheting motion observed during translation¹¹³. The unique inhibition profile of aminoglycosides may be due to additional binding sites in the ribosome other than the primary site in h44 of the 30S subunit. To this effect, neomycin interferes with ribosome recycling through its association with 23S rRNA helix H69, helping to maintain the inter-subunit bridge between H69 and h44³⁴. Aminoglycosides also stabilize the classic state of tRNA binding, providing a basis by which they inhibit tRNA translocation¹¹⁴.

The rise of antibiotic resistance has challenged the use of aminoglycosides in the therapy for bacterial infections. Yet, it spurred renewed interest in the legacy aminoglycosides and the development of novel semisynthetic aminoglycosides such as amikacin, arbekacin, and plazomicin⁹². Amikacin (AMK) is the most widely used semisynthetic aminoglycoside due to being refractory to the majority of aminoglycoside-modifying enzymes. AMK is synthesized by the addition of the 4-

amino-2-hydroxy butyrate (AHB) group at the N1 amino group of the 2-DOS moiety of kanamycin A (KAN) (Figure 2.1b, c). Despite the common usage of AMK to treat a plethora of infections, the contribution of the AHB group to protein synthesis inhibition remains largely unknown. The crystal structure of an RNA mimic of the decoding center and the cryo-EM reconstruction of the 30S and 50S subunits of the *Acetivobacter baumannii* ribosome confirmed the binding of AMK to helix h44⁹¹,⁹³. However, it is conceivable that the AHB group confers AMK a unique binding spectrum to functional ribosome complexes, which may account for the high inhibition potency of AMK on protein synthesis.

Here we use in vitro fast kinetics to show that, in addition to impeding mRNA translocation, AMK strongly inhibits release factor (RF)-mediated peptidyl-tRNA hydrolysis and interferes with ribosome recycling. While the inhibitory effects of AMK are attributed to its binding to the decoding center, our crystal and cryo-EM structures of the 70S ribosome show that one AMK molecule binds to the 50S subunit proximal to the CCA-end of the peptidyl (P)-site tRNA, the functional significance of which is unknown. However, AMK binding to this site provides an opportunity for the development of aminoglycoside derivatives with novel antibacterial properties. Our structural and kinetics data illustrate how AMK and KAN, two closely related aminoglycosides, distinctively inhibit ribosome function.

2.2 Results

2.2.1 Crystal structures of the ribosome bound to amikacin and kanamycin

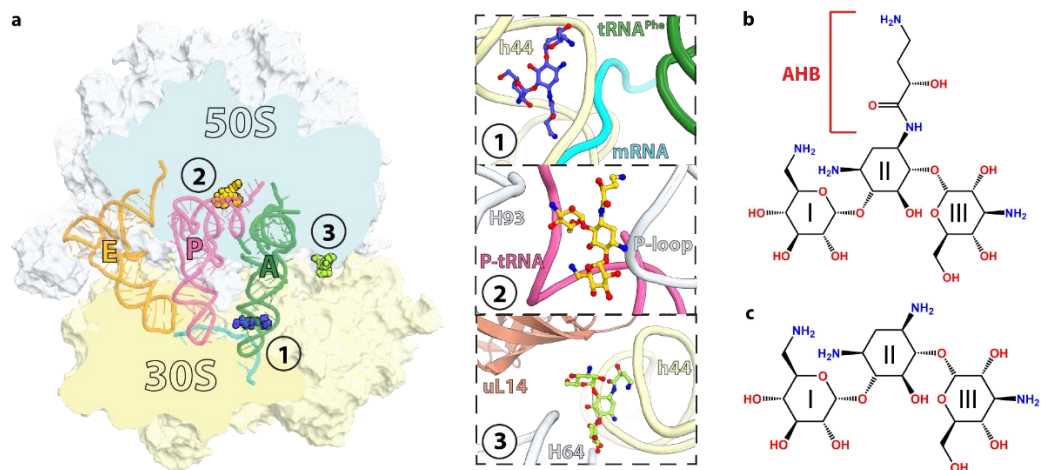


Figure 2.1 Overview of the *Thermus thermophilus* 70S ribosome bound to amikacin. **a** Overview of the 70S ribosome complexed with mRNA (cyan), tRNA^{Phe} in the aminoacyl (A) site (green), tRNA^{fMet} in the peptidyl (P) site (pink), tRNA^{Phe} in the exit (E) site (orange), and AMK bound to three potentially relevant sites. (Inset 1) AMK bound near the decoding center in the small subunit, (inset 2) AMK bound in the large subunit P site, and (inset 3) AMK bound at inter-subunit bridge B5. Chemical structures of the antibiotics AMK with the amino-hydroxy butyrate (AHB) moiety at the N1 position of the central 2-deoxystreptamine (2-DOS) ring II (**b**), and KAN (**c**).

The crystal structures of the *Thermus thermophilus* 70S ribosome in complex with mRNA, tRNAs, AMK or KAN were determined at ~ 2.9 Å resolution by molecular replacement using a high-resolution model of the 70S ribosome with the tRNA and mRNA ligands removed (see “Methods”) 15. The initial difference Fourier density maps calculated using the $F_{\text{obs}} - F_{\text{calc}}$ amplitudes revealed, as expected, clear unbiased density for AMK or KAN in the canonical aminoglycoside

binding site in helix h44 of 16S rRNA (Figure 2.1a inset 1, Figure 2.2a–c, Appendix A Figure 2.1a–c). Additional unique sites are observed for AMK and KAN, providing insights into their ribosome binding modes (Fig. 2.1a, Appendix A Figure 2.2 and 2.3). The peculiar location of two secondary AMK binding sites suggested that they may contribute to ribosome inhibition.

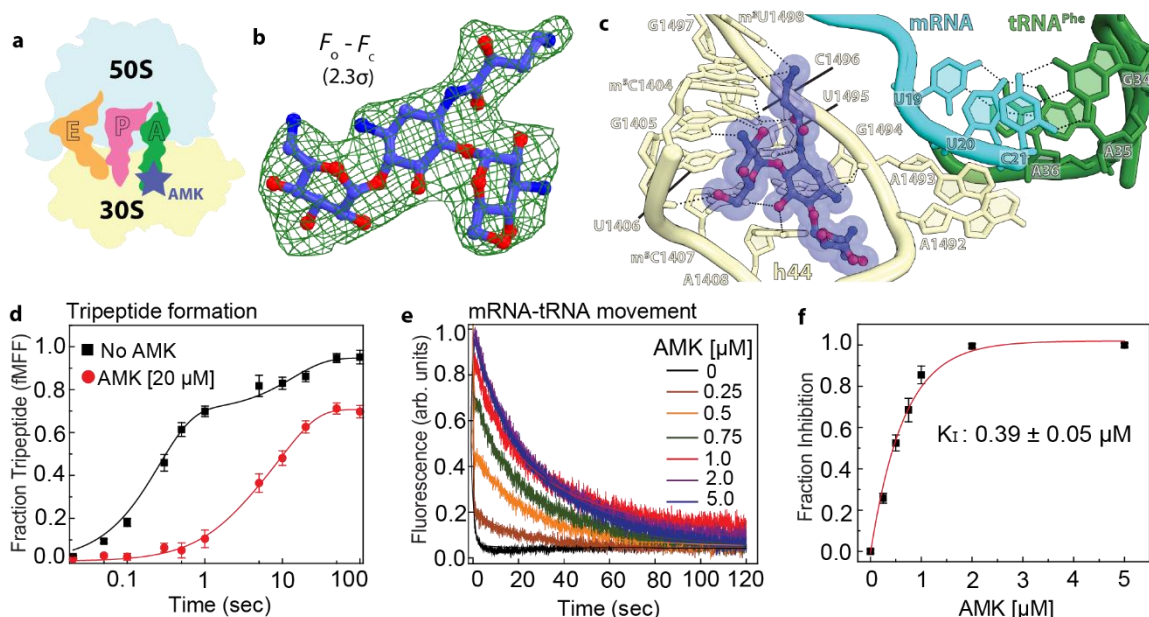


Figure 2.2 Canonical binding site of amikacin near the decoding center. **a** Simplified representation of the 70S ribosome with the AMK binding site indicated with the blue star. **b** The unbiased ($F_o - F_c$) difference electron density map of AMK bound near the decoding center is contoured at 2.3σ . **c** AMK binds within helix h44 of the decoding center where the AHB moiety forms three unique interactions. **d** Time courses of $f[^3\text{H}]\text{Met-Phe-Phe}$ tripeptide formation with EF-Tu ternary complex (TC) ($5\ \mu\text{M}$) and EF-G ($5\ \mu\text{M}$) in the absence (black) and presence of $20\ \mu\text{M}$ AMK (red). Solid lines represent the double exponential fit of the data with SEM from $n = 3$ independent experiments. **e** Time evolution of fluorescence traces obtained for the EF-G ($5\ \mu\text{M}$) catalyzed movement of pyrene-labeled mRNA on 70S ribosomes ($0.5\ \mu\text{M}$) in the presence of various concentrations (0–5 μM) of AMK. The inhibition of mRNA movement by AMK was estimated from amplitudes of the slow phase of fluorescence traces relative to the total transition (normalized to 1) indicative of inhibited fraction of the ribosomes. **f** The fraction of AMK-inhibited pre-TC plotted against AMK concentration. Data were fitted with hyperbolic function (solid line) and half-inhibitory concentration (K_i) of AMK on the inhibition of translocation was

estimated from mid-point of transition. Experiments were conducted in triplicates and error bars indicate the SEM of data.

One secondary binding site for AMK is in the vicinity of the P-site tRNA acceptor stem 3'CCA-end and the P-loop of 23S rRNA (Figure 2.1a inset 2, Figure 2.3a, b). At this site, the majority of the interactions AMK makes with rRNA and tRNA are mediated by sugar-phosphate backbones. Rings II and III of AMK stack with the ribose of nucleotides G2253 (*Escherichia coli* nucleotide numbers are used throughout) of the P-loop and C74 of P-site tRNA (Figure 2.3c, d). The AHB moiety and ring II form a surface that is chemically complementary with that of the universally conserved nucleotides G2252 and G2253 of the P-loop (Figure 2.3d). The hydroxymethyl in ring III and the amine in ring II are within hydrogen-bonding distance of the non-bridging oxygen atoms of P-site tRNA A73 and C2254 of the P-loop, respectively, and the amine of the AHB group forms multiple H-bonding interactions with G2252 of the P-loop (Figure 2.3d). The interactions mediated by the AHB group of AMK with the P-loop likely contribute to the binding of AMK to this site because KAN, which lacks the AHB moiety, does not bind to the P site of the 50S subunit.

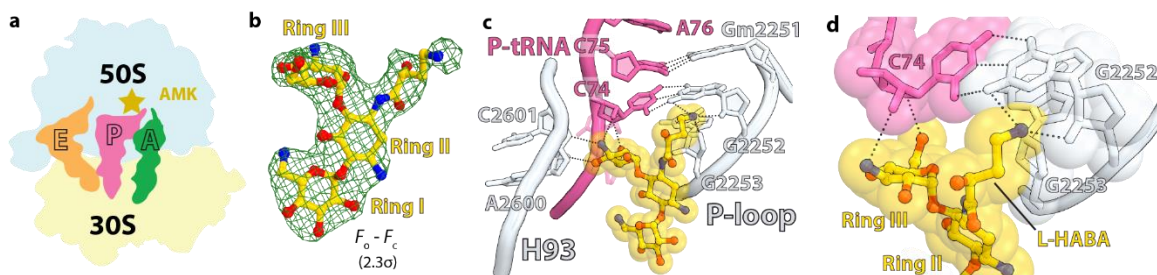


Figure 2.3 Amikacin binding site in the large subunit proximal to the P-site tRNA. **a** Cartoon representation of the 70S ribosome carrying three tRNAs with the AMK binding site indicated with the yellow star. **b** The unbiased ($F_o - F_c$) difference electron density map of AMK bound to the large subunit P site is contoured at 2.3σ . **c** In the large subunit AMK (yellow) binds near the CCA-end of

the P-site tRNA (pink), the conserved 23S rRNA P-loop (white), and helix H93 (white). **d** Interactions between AMK (yellow) and the Watson-Crick base pair G2252-C74 formed by the P-loop (white) and the P-tRNA CCA-end (pink).

The binding site of AMK in the P site of the 50S subunit is distinct from that of the translation inhibitors blasticidin S (BlaS) and bactobolin A (BacA)^{115, 116}. Contrary to BlaS and BacA, AMK does not interfere with the conformation of the CCA-end of P-tRNA (Figure 2.3c). BlaS, a cytidine nucleoside analog, spatially replaces C75 of tRNA and displaces it toward the A site, which interferes with the accommodation of the catalytic domain 3 containing the GGQ loop in release factors (RFs), thereby inhibiting RF-mediated peptidyl-tRNA hydrolysis¹¹⁵⁻¹¹⁸ (Appendix A Figure 2.4a). BacA also displaces the CCA-end of tRNA toward the A site, and correspondingly, is proposed to also inhibit RF-mediated peptide release¹¹⁹ (Appendix A Figure 2.4b).

In the ribosome, interactions between helices h44, H64, and ribosomal protein uL14 form bridge B5, the largest inter-subunit contact area^{22,23}. The difference Fourier map of the *T. thermophilus* 70S•AMK complex revealed one AMK molecule bound between the 30S and 50S subunits at the center of bridge B5 (Figure 2.1a inset 3, Figure 2.4a–c). The inter-subunit contact surface area (~1185 Å²) is increased to ~1430 Å² upon binding of AMK at bridge B5, suggesting that AMK strengthens this inter-subunit contact and may stabilize the 70S ribosome (Appendix A Figure 2.5a,b). At this site, AMK interacts with non-bridging oxygen atoms on the major groove side of helix h44 in the 30S subunit, with ribosomal protein uL14, and with nucleobases and the sugar phosphate backbone facing the minor groove of helix H64 in the 50S subunit (Figure 2.4c). While the 2-

DOS ring II of AMK does not interact with the ribosome, ring I stacks with the ribose of C1988 in H64 (Figure 2.4c). The amine and hydroxyl groups on one side of ring I are within hydrogen-bonding distance of non-bridging oxygen atoms of A1473 and G1474 in h44, and the hydroxyl groups on the other side of ring I interact with the 2'OH and exocyclic amino groups of G1987 in H64 (Figure 2.4c). AMK reaches across the major groove of h44 with the amino group of the AHB side chain forming water-mediated hydrogen bonding interactions with the phosphate oxygen atoms of C1420 and G1421 in h44 (Figure 2.4c). The AHB hydroxyl group and the chemical moieties decorating ring III form multiple interactions with ribosomal protein uL14 residues Tyr7, Glu45, Glu54, and the main chain carbonyl oxygen of Lys44 (Figure 2.4c). The observation that KAN does not bind to this site at the subunit interface of the *T. thermophilus* 70S ribosome indicates that the water-mediated interactions between the AHB moiety of AMK and helix h44 contribute to the binding of AMK at bridge B5.

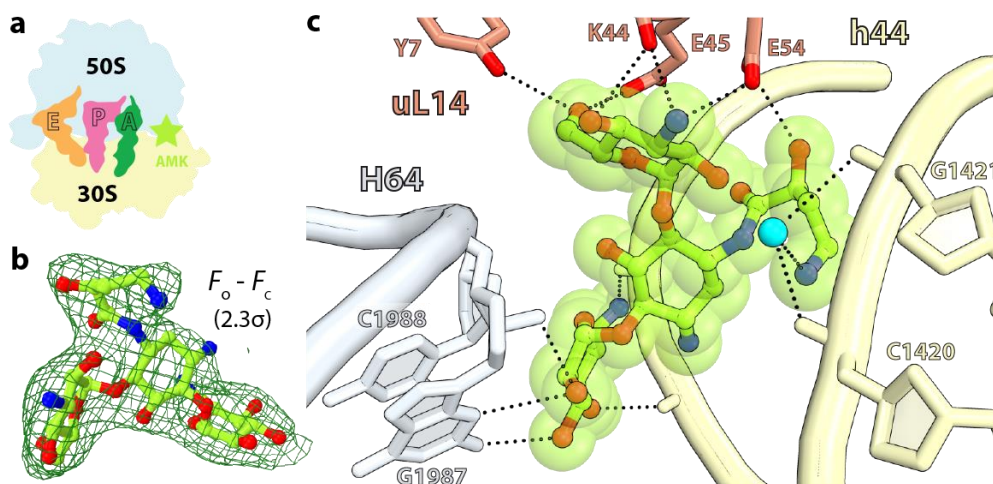


Figure 2.4 Amikacin binding site at inter-subunit bridge B5. **a** Simplified representation of the 70S ribosome with the AMK binding site indicated with the green star. **b** The unbiased ($F_o - F_c$) difference electron density map of AMK bound

at the inter-subunit space is contoured at 2.3σ . **c** AMK interacts with elements of inter-subunit bridge B5, helix h44 of 16S rRNA, helix H64 of 23S rRNA, and ribosomal protein uL14. The amine group of the AHB group forms water-mediated (cyan) H-bonds with the phosphate backbone of h44

2.2.2 Amikacin interferes with mRNA translocation during peptide elongation

To assess the effects, if any, of AMK binding in the 50S subunit near the CCA-end of P-site tRNA, we first conducted kinetic experiments to estimate the rates of dipeptide (fMet-Phe) formation in the absence and presence of AMK. In these experiments, ternary complex (TC) of EF-Tu•GTP•Phe-tRNA^{Phe} was rapidly mixed in a quench-flow with initiated ribosomes containing f[³H]Met-tRNA^{fMet} in the P site and the accumulation of dipeptide (f[³H]Met-Phe) with time was monitored. The rates of dipeptide formation with AMK-free ribosomes ($56 \pm 8 \text{ s}^{-1}$) was virtually identical to that observed with AMK-bound ribosomes ($53 \pm 5 \text{ s}^{-1}$), indicating no effect of AMK on delivery and accommodation of the aminoacyl-tRNA and peptidyl transfer (Appendix A Figure 2.6). This agrees with the observation that AMK at this location does not interfere with the conformation of the CCA-end of the P-site tRNA (Figure 2.3c, Appendix A Figure 2.4a,b). Likewise, KAN also showed no effect on dipeptide formation (Appendix A Figure 2.6a).

Within coordinate errors, we observe AMK bound to h44 in the same conformation as that previously reported from the structures of AMK bound to an RNA fragment of h44 and to the *Acinetobacter baumannii* 30S ribosomal subunit^{91, 93} (Appendix A Figure 2.7). Binding of AMK to h44 promotes the flipped-out conformation of the two universally conserved nucleotides A1492 and A1493

forming A-minor interactions with the mRNA-tRNA duplex in the A site (Figure 2.1a inset 1, Figure 2.2a–c, Appendix A Figure 2.7). The aminoglycoside-induced conformation of the decoding center promotes amino acid misincorporations by facilitating the binding of near-cognate aminoacyl-tRNAs¹²⁰. Binding of aminoglycosides to this site further exerts strong inhibition of tRNA translocation^{114, 120}. Single-molecule fluorescence resonance energy transfer (smFRET) studies reported that most aminoglycosides, including KAN, stabilize the classical state of tRNA binding and inhibit EF-G-catalyzed translocation^{114, 121, 122}. Correspondingly, ablation of the primary binding site through the A1408G mutation in h44 increased the K_i of EF-G-dependent translocation of neomycin and tobramycin by 100- and 25-fold, respectively¹²³. Furthermore, the ability of neomycin to promote reverse translocation depends on its primary binding site in h44¹²³.

We next estimated the rates of tripeptide formation in the absence and presence of AMK. In these experiments, EF-Tu•GTP•Phe-tRNA^{Phe} with EF-G•GTP were rapidly mixed with mRNA-programmed ribosomes containing f[³H]Met-tRNA_i^{fMet} in the P site and time courses of tripeptide (fMet-Phe-Phe) formation were measured. While AMK showed no effect on dipeptide formation (Appendix A Figure 2.6a), the rates for tripeptide formation dropped from $6.1 \pm 1.2 \text{ s}^{-1}$ to $1.1 \pm 0.5 \text{ s}^{-1}$ with the addition of 20 μM AMK (Figure 2.2d). These results suggest that the binding of AMK to elongating ribosomes affects the stage between dipeptide and tripeptide formation i.e., ribosomal translocation. We then directly measured the kinetics of EF-G-catalyzed movement of mRNA-tRNA during ribosomal translocation using a fluorescence assay based on pyrene-labeled mRNA (Figure

2.2e, f)^{120, 124}. Although this assay includes steps of aminoacyl-tRNA accommodation and peptidyl transfer prior to ribosomal translocation, the insensitivity of these processes toward AMK allows the precise estimation of its action on mRNA-tRNA movement. The fluorescence traces indicative of EF-G-catalyzed mRNA movement in the absence of AMK were nearly monophasic (95%), and the estimated rate of mRNA movement was $12.4 \pm 2 \text{ s}^{-1}$ (Figure 2.2e). However, upon pre-incubation with AMK, biphasic fluorescence traces were observed (Figure 2.2e). Interestingly, the meantime ($96 \pm 12 \text{ mSec}$) of the fast phase of fluorescence transition was comparable to that in the absence of AMK ($83 \pm 9 \text{ mSec}$), probably reflecting translocation on AMK-free ribosomes. Increased concentrations of AMK yielded a more predominant slow phase, however with virtually identical mean times ($\sim 18.3 \pm 1.7 \text{ Sec}$), indicative of increased binding of AMK and delayed translocation on AMK-bound ribosomes (Figure 2.2e). From the amplitudes of the slow phase, we then estimated the fraction of AMK-inhibited ribosomes prior to translocation and plotted them against each concentration of AMK¹²⁰ (Figure 2.2f). The fraction of inhibited ribosomes increased hyperbolically and reached its half-maximal value (K_i) at $0.39 \mu\text{M}$ AMK, identical to that of arbekacin (ABK)¹²⁰ ($\sim 0.4 \mu\text{M}$), a similar AHB-containing semisynthetic aminoglycoside. Nevertheless, similar to ABK¹²⁰, all the fluorescence traces recorded in the presence of AMK reached the same basal level verifying the completion of mRNA translocation in the presence of AMK. By comparison, KAN lacking the AHB side chain shows much weaker inhibition of translocation with $K_i \sim 0.8 \mu\text{M}$ (Appendix A Figure 2.6d). The twofold higher K_i of KAN than AMK can

be attributed to the fewer interactions of KAN with the decoding center due to the absence of the AHB group, which altogether reduces its affinity for the primary aminoglycoside binding site on the ribosome. The AHB group of AMK forms three additional hydrogen bonds with nucleotides C1496, G1497, and m³U1498 in h44 (Figure 2.2c). These interactions are unique to AMK, and likely to ABK as well, and may rigidify the top of h44 which is known to bend by ~8 Å toward the P site during EF-G-mediated tRNA translocation¹²⁵, providing a plausible explanation for the similar inhibitory effect of AMK and ABK on the movement of mRNA and tRNAs.

2.2.3 Amikacin inhibits release factor-mediated peptide release

Aminoglycosides have been reported to inhibit RF-mediated peptide release^{126, 127}. Recently ABK, which also harbors the AHB group, was shown to impair peptide release¹²⁰. We therefore asked whether AMK interferes with RF-mediated peptidyl-tRNA hydrolysis. To this end, we prepared pre-termination ribosome complexes (pre-TC) harboring the (BOP)•Met-Phe-Leu tripeptide attached to tRNA^{Leu} in the P site and a stop codon (UAA) in the A site, and rapidly mixed in a stopped-flow instrument with a RF mixture containing an excess of RF2. The resulting time courses of fluorescence transition due to the release of the (BOP)•Met-Phe-Leu tripeptide followed a nearly monophasic curve indicating a single-round of peptide release (Figure 2.5a). The apparent rate of peptide release from the AMK-free pre-TC was $7.1 \pm 0.8 \text{ s}^{-1}$. Upon addition of AMK to the pre-TC, we observed remarkable inhibition of peptide release. The rates estimated from the predominant fast phase (> 99%) were similar without or with different concentrations of AMK. However, the fluorescence amplitudes decreased with

increasing AMK concentration indicating that AMK-bound ribosomes are practically incapable of peptide release (Figure 2.5a). The fraction of inhibited pre-TCs determined by the fractional loss of fluorescence amplitudes increased hyperbolically with the concentration of AMK, giving a half-maximal inhibitory concentration (K_i) of $0.15 \pm 0.02 \mu\text{M}$ (Figure 2.5b). The antibiotic KAN, the parent compound of AMK, has no measurable effect on the termination step of translation (Appendix A Figure 2.6b). Noteworthy is that ABK inhibits peptide release with a much higher K_i value¹²⁰ ($0.6 \mu\text{M}$ for RF1 and $0.5 \mu\text{M}$ for RF2). These results show that AMK is probably the most potent inhibitor of RF-mediated peptide release among all known aminoglycosides.

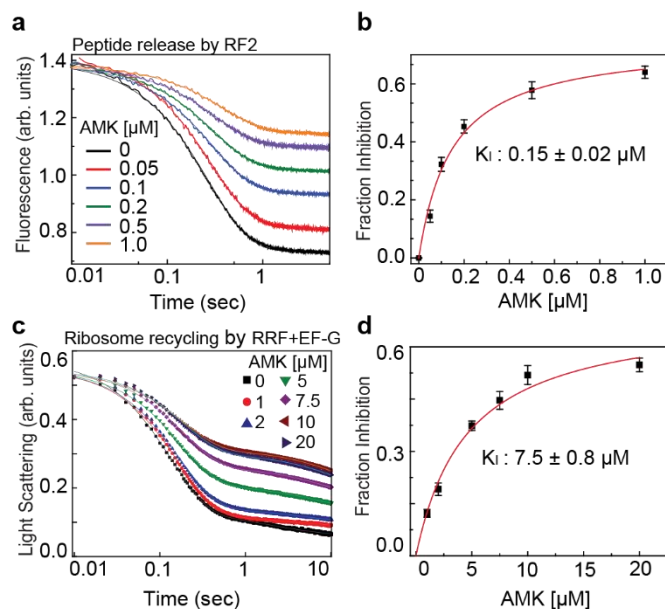


Figure 2.5 Effects of amikacin on the kinetics of peptide release and ribosome recycling. **a** Time courses of BOP-Met-Phe-Leu release from the P site of the ribosomes in pre-TC ($0.1 \mu\text{M}$) upon mixing with RF2 ($1 \mu\text{M}$) in the presence of various concentrations of AMK ($0-1 \mu\text{M}$). The near monophasic curves are fitted with double exponential function (solid lines) and the rates and amplitudes of the predominant fast phase ($> 99\%$) were determined. The fraction inhibited was estimated from the fractional loss in fluorescence amplitude for a given AMK concentration considering the total amplitude of fluorescence transition (without

AMK) as 1. **b** Fraction inhibition of RRF-mediated peptide release as the function of increasing concentrations of AMK. Solid line is the hyperbolic fit of data from which half-maximal inhibitory concentration (K_i) of AMK for peptide release was estimated. **c** Time traces for Rayleigh light scattering upon splitting of post-TC ribosomes ($0.5 \mu\text{M}$) into subunits by the concerted action of RRF ($20 \mu\text{M}$) and EF-G ($10 \mu\text{M}$) in the presence of various concentrations of AMK ($0\text{--}20 \mu\text{M}$). The scattering traces were fitted with double exponential function and the rates and amplitudes of both the fast and slow phases were determined. **d** Fraction inhibition of RRF and EF-G-mediated ribosome splitting was estimated from the fractional loss of the amplitude of the fast phase considering amplitude of the entire transition without AMK as 1. The solid line represents the hyperbolic fit of the fraction inhibition plotted against AMK concentration from which the half-maximal concentration (K_i) of AMK to inhibit ribosome recycling was estimated. Experiments were conducted in triplicates, data were fitted in Origin(Pro), Version 2016 (OriginLab Corp.), and error bars indicate the SEM of data.

2.2.4 Amikacin inhibits recycling of the ribosome by EF-G and RRF

During ribosome recycling, the inter-subunit bridges are dissolved and the 70S ribosome dissociates into individual 30S and 50S subunits. This process is catalyzed by the coordinated action of two translation factors in bacteria, the ribosome recycling factor (RRF) and elongation factor-G (EF-G)^{31, 47, 53, 60, 63, 71, 128, 129}. We measured the effects of AMK on post-termination ribosome splitting into subunits by RRF and EF-G. We prepared a post-termination 70S ribosome complex (post-TC) programmed with a deacylated-tRNA in the P site and subjected it to dissociation into subunits upon mixing with RRF, EF-G, and IF3 in a stopped-flow instrument. The time course of ribosome splitting was then monitored by following the decrease in Rayleigh light scattering in the absence and presence of various concentrations of AMK (Figure 2.5c). The traces were fitted with a double exponential function and mean times and amplitudes of the fast

phases indicating single-round ribosome splitting were determined. In the absence of AMK, the meantime of ribosome splitting was 205 ± 8.6 mSec, which increased to 574 ± 14 mSec upon the addition of $10 \mu\text{M}$ AMK (Figure 2.5c). Notably, the amplitude of the fast phase decreased with the increase of AMK. The fraction inhibited was estimated by the fractional loss of the amplitude of the fast phase, which increased hyperbolically and saturated with $10 \mu\text{M}$ AMK (Figure 2.5d). The half-maximal concentration of AMK for ribosome recycling (K_i) was estimated from the transition mid-point as $7.5 \pm 0.8 \mu\text{M}$ (Figure 2.5d). In comparison, KAN has only a marginal effect on ribosome recycling (Appendix A Figure 2.6c). Also, the reported K_i value for the similar aminoglycoside ABK in ribosome recycling is $30 \mu\text{M}$ ²⁴, suggesting that AMK is the most potent aminoglycoside inhibitor of ribosome splitting.

2.2.5 Cryo-EM structure of the *E. coli* ribosome bound to amikacin

The differential inhibition of translation by AMK and KAN may originate from the secondary binding sites observed in the *T. thermophilus* ribosome. However, the presence of secondary sites raises the legitimate concern that they may not be populated in the *E. coli* ribosomes at the drug concentrations used in the kinetics experiments. The crystals of *T. thermophilus* ribosomes were transferred into cryoprotection buffer solutions containing a high concentration ($100 \mu\text{M}$) of AMK or KAN, and then harvested and frozen. Likewise, the concentration of the ribosomes inside the crystals is ~ 0.2 mM, thereby representing non-physiological conditions.

To elucidate whether AMK binds to the P site in the 50S subunit and at inter-subunit bridge B5 of the *E. coli* ribosomes, we assembled a complex with mRNA, tRNAs, and a 20-fold molar excess of AMK, closely mimicking the conditions used in the kinetics assays, and subjected the sample to cryo-EM (Appendix A Figure 2.8). In this structure, refined to a nominal resolution of 2.9 Å (Appendix A Figure 2.9), AMK is bound near the decoding center in h44 and to the P site of the 50S subunit proximal to the tRNA as seen in the *T. thermophilus* ribosome (Appendix A Figure 2.10a, c). This observation agrees with AMK forming backbone-mediated interactions with the 23S rRNA and the CCA-end of the P-site tRNA, suggesting this binding site is universal. However, there is no density for AMK at bridge B5 in the *E. coli* ribosome, corroborating the non-conserved nature of Tyr7 and Glu54 in ribosomal protein uL14 (Appendix A Figure 2.11), residues that interact with AMK at this site in the *T. thermophilus* ribosome (Figure 2.4c). Increasing the concentration of AMK to 100 μM, the same as we used to soak the *T. thermophilus* ribosome crystals, did not populate this site (not shown), indicating that it is species-specific. Therefore, the inhibition of recycling of the *E. coli* ribosomes is not mediated through the binding of AMK at the subunit interface.

Two additional AMK molecules are observed in the *T. thermophilus* 70S ribosome, one in the 30S subunit and one in the 50S subunit (Appendix A Figure 2.2a). In the small subunit, AMK interacts with helix h7 in the body domain of the 30S subunit (Appendix A Figure 2.2b-d). In the large subunit, AMK contacts helices H18 in domain I and H28 in domain II of the 23S rRNA. At this site, AMK also interacts with Arg168 of ribosomal protein uL4 (Appendix A Figure 2.2e-g). In the

E. coli 70S ribosome, there is no density for AMK at these two sites, presumably indicating low-affinity binding sites. We note that the shorter helix H28 in the *E. coli* 50S subunit ablates one side of the drug binding pocket, suggesting that it may be a species-specific site.

In addition to binding to h44 near the decoding center, KAN binds to three secondary sites in the *T. thermophilus* 50S subunit (Appendix A Figure 2.3a). One KAN molecule interacts with helix H88 located in domain V of 23S rRNA (Appendix A Figure 2.3b-d), the other KAN contacts helices H40 and H42 in domain II (Appendix A Figure 2.3e-g), and the third KAN is found at the base of the A-site finger helix H38, interacting with helix H85 and with Lys8 of protein uL16 (Appendix A Figure 2.3h-j). While these secondary binding sites are not likely to be physiologically relevant and probably the result from the high concentration of drug used during crystallization, they nevertheless enrich the catalog of interactions between small molecules and RNA.

2.2.6 A1408G ribosomes are resistant to amikacin

We used *E. coli* ribosomes carrying the A1408G mutation to explore the functional significance of the AMK binding site in the 50S subunit proximal to the CCA-end of the P-site tRNA. In the presence of 100 μ M AMK or KAN, the rate of the EF-G-catalyzed movement of mRNA during ribosomal translocation is unchanged (Appendix A Figure 2.12a), indicating that AMK bound near the peptidyl transferase center does not interfere with tRNA translocation, consistent with a previous report showing that BlaS, which also binds in the vicinity of AMK in the

50S subunit P site, did not affect the apparent rate of EF-G-catalyzed translocation¹³⁰. Likewise, RF2-mediated peptide release from the A1408G mutant ribosomes is unaltered by AMK (Appendix A Figure 2.12b), again showing that the mutant ribosomes are fully resistant to AMK.

The minimum inhibitory concentrations (MICs) of AMK and KAN for wild-type and A1408G mutant strain of *E. coli* SQ171 were determined using the standard broth microdilution method. Our results indicate that the MICs of KAN for wild-type (8 µg/mL) and A1408G (≥256 µg/mL) were high compared to the MICs of AMK for wild-type (1 µg/mL) and A1408G (≥16 µg/mL) (Appendix A Table 2.1). The variation is possibly due to the difference in the affinity of these two drugs for the primary binding site in h44 near the decoding center within the 30S subunit.

The binding of RF2 to the stop codon in the A site causes nucleotide A1493 to stack inside h44 in a position that is not compatible with bound AMK²⁶ (Appendix A Figure 2.13a), possibly explaining the inhibition of RF2-mediated peptidyl-tRNA hydrolysis. Similarly, RRF and EF-G bound to the ribosome favor the intra-h44 stacking of A1492, which would in turn collide with AMK⁶³ (Appendix A Figure 2.13b). Taken together, our findings are consistent with the primary binding site in h44 for AMK being responsible for the inhibition of mRNA translocation, RF-mediated peptide release, and ribosome recycling.

2.3 Discussion

Aminoglycoside antibiotics are known to bind to secondary sites in the ribosome. For instance, neomycin and tobramycin associate with helix H69 in the

50S subunit, in addition to the canonical site in h44 of the 30S subunit³⁴. It is therefore challenging to disentangle the physiological role and the contribution of each binding site to ribosome inhibition. One approach is to ablate the canonical aminoglycoside binding site in h44 with the A1408G mutation, which then allows to assess the effects of the other sites in translation inhibition. This strategy was previously used to decipher the mechanism by which tobramycin and neomycin inhibit ribosome recycling¹²³. Interestingly, the inhibition of recycling of the A1408G ribosomes by neomycin and tobramycin is virtually the same as with the wild-type ribosomes, showing that the binding of these aminoglycosides to H69 is likely responsible for this inhibition.

In this work, we report that AMK and KAN exhibit unique translation inhibition profiles. These results, together with the reported role of the secondary site in H69 for neomycin and tobramycin on ribosome inhibition¹²³, prompted us to systematically probe the function of the secondary binding sites of AMK identified in the structure of the *T. thermophilus* ribosome (Figure 2.1, Appendix A Figure 2.2). Initially, the data showing that KAN is a less efficient ribosome inhibitor than AMK seemed to correlate with the presence of secondary binding sites for AMK that may be of physiological relevance. We employed a two-pronged approach to elucidate the role of the secondary binding sites for AMK in the P site of the 50S subunit and at inter-subunit bridge B5.

We first analyzed the conservation of the residues in ribosomal protein uL14 at bridge B5 that interact with AMK. The most striking difference between *T. thermophilus* and *E. coli* is at position 54 (Appendix A Figure 2.11). In *T.*

thermophilus, Glu54 forms a hydrogen bond with the amine of ring III in AMK (Figure 2.4c). In other representative bacteria, a basic residue (K or R) occupies position 54 (Appendix A Figure 2.11), which may alter the binding site for AMK. This observation suggested that AMK may not bind to bridge B5 in the *E. coli* ribosomes, which we used in the kinetics experiments.

We addressed this caveat by using cryo-EM to visualize a complex between AMK and a functional *E. coli* ribosome bound to mRNA and tRNAs. Here, the concentrations of ribosomes and AMK closely mimic those used in the kinetics assays. The density map of the reconstruction unambiguously shows that AMK is not bound at bridge B5 in the *E. coli* ribosomes, ruling out any inhibitory effect mediated by this secondary site. In this EM map, the clear density for AMK in the P site of the 50S subunit near the CCA-end of tRNA (Appendix A Figure 2.10c), and the RNA phosphate backbone-mediated interactions with AMK at this location, suggested that this binding site is likely universal. However, three-dimensional (3D) variability analysis focused on the AMK binding site in the 50S subunit revealed that less than 30% of the ribosomes contained clear density for the drug at this site (Appendix A Figure 2.8), suggesting that AMK has a lower affinity for the P site of the 50S subunit than for the canonical site in h44. This observation is also consistent with the 16-fold higher MIC of AMK for the *E. coli* strain expressing A1408G mutant ribosomes (Appendix A Table 2.1).

To further assess the relevance of the binding site in the 50S subunit near the P-site tRNA, we used the A1408G ribosomes to perform kinetics of mRNA translocation and RF2-mediated peptide release (Appendix A Figure 2.12). These

assays conclusively show no inhibition by AMK, indicating that the binding site proximal to the tRNA in the 50S subunit does not affect ribosome function. While the inhibition of ribosome recycling by neomycin and tobramycin could be attributed to the binding site in H69¹²³, our results associate all the ribosomal inhibitory effects of AMK to the canonical binding site in h44.

It is intriguing that mRNA translocation proceeds to completion in the presence of 5 μ M AMK (Figure 2.2e), while AMK-bound ribosomes are incapable of peptide release and recycling at the highest concentration of AMK (Figure 2.5a, c). The selection of aminoacyl-tRNAs by the ribosome involves the monitoring nucleotides A1492 and A1493 in h44, which probe the geometry of the minor groove of the mRNA-tRNA anticodon helix. For the A-site tRNA to translocate to the P site, the monitoring bases disengage from the tRNA-mRNA complex, a process that is facilitated by EF-G^{12, 13}. It is possible for A1492 and A1493 to remain unstacked and not interfere with bound AMK in h44, which would allow mRNA translocation to proceed despite the presence of AMK. However, the binding of RF2 and RRF to the ribosome cause nucleotide rearrangements in the decoding center that are not compatible with AMK bound in h44 (Appendix A Figure 2.13a, b).

In the structure of the pre-recycling non-rotated 70S ribosome complex with RRF and EF-G, domain II of RRF remodels the tip of H69 and the decoding center in the 30S subunit⁶³. In this complex, A1492 stacks inside h44 and is within interaction distance of A1408. In this conformation, A1492 is not compatible with AMK bound to its primary site (Appendix A Figure 2.13b). The competition between

AMK and A1492 for the same site seemingly explains why, over the time course of the experiment, the ribosome recycling reaction does not reach completion (Figure 2.5c). Similarly, during translation termination, binding of RF2 to the stop codon triggers rearrangements of A1493, and the stacking of A1493 within h44 is not compatible with bound AMK²⁶ (Appendix A Figure 2.13a). The reaction of RF2-mediated peptide release does not reach completion, presumably because ribosomes that are bound to AMK do not simultaneously bind to RF2 (Figure 2.5a). The higher affinity of AMK for h44, relative to KAN, explains their different inhibition profiles. It is likely that the remodeling of the ribosome decoding center upon binding of RRF and RF2 promotes dissociation of KAN from the canonical site. The effects appear to be similar to the inhibition of the RF-catalyzed peptide release by neomycin and paromomycin¹²⁷. In agreement with this premise, binding of RF1 to the ribosome promoted dissociation of paromomycin from h44¹²⁷.

Despite the apparent non-physiological relevance of the AMK binding site in the P site of the 50S subunit, it nevertheless provides valuable information for future development and repurposing of old antibiotics. This approach represents a promising strategy to circumvent the spread of resistance to the drugs currently in use^{131, 132}. The adjacency of the AMK binding site near the tRNA in the large ribosomal subunit to the old antibiotics BlaS and BacA represents an opportunity to generate chimeric molecules that may have improved antibacterial properties and activity. A similar strategy was used to generate radezolid¹³³, a chimeric molecule between linezolid and sparsomycin based on their overlapping binding sites within the peptidyl transferase center of the 50S subunit^{117, 134}. Radezolid has

a higher affinity for the ribosome than linezolid, which provided improved antibacterial activity against various Gram-positive bacteria¹³³. The nucleoside cytidine analog BlaS, and the antitumor antibiotic BacA, are toxic to prokaryotic and mammalian cells^{115, 135-137}. Derivatives of BacA and BlaS, based on their structures bound to the ribosome^{118, 119, 138}, are explored to improve drug-like properties and circumvent the inhibitory activity toward eukaryotic cells while retaining potency against prokaryotic ribosomes¹³⁹⁻¹⁴³. Their adjacency to AMK may provide strategies to solve this challenging issue.

Collectively, our findings illustrate how two closely related antibiotics, AMK and KAN, exhibit pleiotropic ribosome inhibition activities. It is remarkable how the AHB chemical group increases the efficiency of translation inhibition by AMK. It will be worth exploring further modifications of aminoglycosides, and in particular of AMK, which could increase the binding affinity to the P site of the 50S subunit. The ribosome inhibition activity of such AMK variants could be potentiated by impeding the movement of the acceptor domain of the P-site tRNA as it transits to the E site.

2.4 Methods

2.4.1 Purification of 70S ribosomes, mRNAs, initiator tRNA, and tRNA^{Phe}

Thermus thermophilus 70S ribosomes were purified as described previously⁵⁶ and resuspended in buffer containing 5 mM HEPES-KOH, pH 7.5, 50 mM KCl, 10 mM NH₄Cl, 10 mM Mg(CH₃COO)₂, and 1 mM β-mercaptoethanol (β-ME), at a concentration of approximately 800 A260/mL, flash-frozen in liquid

nitrogen, and stored in small aliquots at $-80\text{ }^{\circ}\text{C}$ until use in crystallization experiments. The *E. coli* strain SQ171, harboring only one ribosomal RNA operon, containing ribosomes with the A1408G mutation in the *rrsB* gene was kindly provided by M. Johansson's laboratory¹⁴⁴. Tight coupled *E. coli* 70S ribosomes (MRE600 and SQ171-A1408G) were purified following standard procedures¹⁴⁵. The 24-mer XR7 mRNA, 5'-GCC AAG GAG GUA AAA **AUG** UUC UAA-3' with strong Shine-Dalgarno sequence (AAGGAGG) (in italics), AUG start codon (bold) followed by the UUC (Phe) (underlined) and UAA (stop) codons was chemically synthesized by Integrated DNA Technologies (Coralville, IA). Other XR7-mRNAs with ORF sequence AUGUUCUUCUAA (Met-Phe-Phe-stop) and AUGUUCCUGUAA (Met-Phe-Leu-stop) were transcribed in vitro and prepared as in ref. 59. Pyrene-labeled mRNA+10 (sequence 5'-UAACAAU AAGGAGGUAUUA**AUGUUCCUGU**-3'-pyrene) coding for Met-Phe-Leu were from IBA-biosciences, Germany¹²⁴. The *E. coli* tRNA^{Phe} and tRNA^{iMet} were expressed and purified as previously described⁶⁰. Nucleotides (ATP, UTP, CTP and GTP) were from Cytiva. All other analytical grade chemicals including amikacin sulfate and kanamycin sulfate were from Sigma-Aldrich (cat# K-1876 and A-2324, respectively).

All in vitro kinetic experiments were carried out in HEPES polymix buffer (pH 7.5) (5 mM HEPES, 95 mM KCl, 5 mM NH₄Cl, 5 mM Mg(OAc)₂, 8 mM putrescine, 0.5 mM CaCl₂, 1 mM spermidine and 1 mM 1,4-dithioerythritol) at 37 °C with energy regeneration components (1 mM ATP, 1 mM GTP, 10 mM

phosphoenolpyruvate (PEP), 1 µg/ ml pyruvate kinase and 0.1 µg/ml myokinase) ensuring cellular free Mg²⁺ concentration (~2 mM)¹²⁰.

2.4.2 Dipeptide and tripeptide formation experiments

Two mixtures, initiation mix (IM) and elongation mix (EM), were prepared in the HEPES polymix buffer. IM contained 70S ribosomes (0.5 µM), f[³H]Met-tRNA^{iMet} (0.55 µM), mRNA Met-Phe-Phe (1 µM), IF1 (0.5 µM), IF2 (0.5 µM) and IF3 (0.5 µM) and EM was comprised of tRNAPhe (5 µM), EF-Tu (5 µM), EF-Ts (2 µM), Phe (200 µM), and PhetRNAPhe synthetase (1.5 units/µl). For tripeptide experiments, EM was supplemented with EF-G (5 µM). To test the effects of AMK and KAN, 20 µM of each drug was added to both IM and EM. Both mixes were incubated for 15 min at 37 °C. After incubation the IM and EM were rapidly mixed in a quench-flow instrument (RQF-3; KinTek Corp., USA) and the reactions were quenched with formic acid (17% final) at definite time intervals. Samples were processed as described earlier²⁴ and the relative amounts of f[³H]Met, f[³H]Met-Phe, and f[³H]Met-Phe-Phe in the supernatant were separated using a reverse-phase chromatography column (C-18, Merck) connected to a Waters HPLC system coupled with the in-line β-RAM radioactive detector. The rates of dipeptide and tripeptide in the absence and presence of AMK and KAN were estimated by fitting the data to a single exponential function using Origin(Pro), Version 2016 (OriginLab Corp., Northampton, MA, USA). Experiments were conducted in triplicates and average data was plotted with SEM.

2.4.3 Pyrene-mRNA based assay for ribosomal translocation

Initiation mix (IM) was prepared essentially in a similar way as in the case of dipeptide experiments, except that XR7-mRNA in IM was replaced with 3' pyrene-labeled mRNA+10 (coding for Met-Phe-Leu)¹²⁴. AMK (0-5 μ M) was added to IM as indicated. EM was prepared as in the case for tripeptide experiments. Both mixes were incubated for 15 min at 37 °C. Equal volumes of IM and EM were rapidly mixed in a stopped-flow instrument (μ SFM BioLogic) at 37 °C and the fluorescence transition was monitored using 360-nm long-pass filter (Comar Optics Ltd.) after exciting at 343 nm. The resultant fluorescence traces were fitted with a double exponential function using Origin(Pro) 2016. Experiments were conducted in triplicates.

2.4.4 Measurement of RF-mediated peptide release

Pre-termination ribosome complex (Pre-TC) containing BODIPYTM (BOP)•Met-Phe-Leu-tRNA^{Leu} tripeptide in the P site and a stop codon (UAA) in the A site was prepared in HEPES polymix buffer (pH 7.5)^{120, 146}. Equal volumes of pre-incubated pre-TC (0.1 μ M) and RF mixture containing RF2 (1 μ M) were rapidly mixed in a stopped-flow instrument (μ SFM BioLogic) at 37 °C. To assess the effect of AMK and KAN on peptide release, indicated concentration of each drug was added to both mixes. The release of BOP-Met-Phe-Leu tripeptide was followed by monitoring the decrease in BOP fluorescence (excitation: 575 nm) with a cutoff filter of 590 nm. The fluorescence traces were fitted with a double exponential function using Origin Pro 2016 and the rates and amplitudes of the predominant

fast phase were estimated¹⁴⁷. The fraction of the ribosomes inhibited with a given concentration of AMK was estimated by subtraction of the amplitude of the fluorescence curves with AMK from the one without AMK, divided by the total fluorescence change (without any drug). The fraction inhibition was plotted as a function of AMK concentration and fitted with hyperbolic equation to determine the half-maximal inhibitory concentration (K_i). Experiments were conducted in triplicates and average data was plotted.

2.4.5 Ribosome recycling

Post-termination ribosome complex (post-TC), with an empty A site and deacylated tRNA in the P site, was prepared by mixing 70S ribosomes (0.5 μM) with XR7-mRNA (Met-Phe-Leu) (1 μM) and deacylated tRNA^{Leu} (1 μM) in HEPES–polymix buffer. A factor mix (FM) containing RRF (20 μM), EF-G (10 μM), and IF3 (1 μM) was prepared. AMK (0–20 μM) or KAN (0–100 μM) was added to both post-TC and FM. Both mixes were incubated at 37 °C for 5 min. Equal volumes of post-TC and FM were rapidly mixed in a stopped-flow instrument (μSFM BioLogic) and the splitting of post-TC into subunits was monitored as a decrease in Rayleigh light scattering at 365 nm¹⁴⁸. The rate of post-TC dissociation was estimated by fitting the data with the double exponential equation in Origin Pro 2016. The rates and amplitudes of the fast phases were determined. The fraction of the inhibited ribosomes was estimated by subtraction of the amplitude of the fast phase with AMK from the one without AMK, divided by total amplitude change (without any drug). The half-maximal inhibitory concentration (K_i) was estimated by plotting

fraction inhibition against AMK concentration and fitting the data with hyperbolic function using Origin Pro 2016.

2.4.6 Minimum inhibitory concentration (MIC) measurement

The minimum inhibitory concentrations (MICs) of AMK and KAN were determined by broth microdilution (BMD) method following Clinical and Laboratory Standard Institute (CLSI) guidelines for aminoglycosides. Briefly, twofold serial dilutions of AMK and KAN were prepared in cation-adjusted Mueller Hinton broth (CA-MHBII) corresponding to the concentrations ranging from 0.25 to 256 $\mu\text{g}/\text{mL}$ and added to the 96-well (12 \times 8) round-bottomed microtiter plate. A control well containing only media without any antibiotic served as growth control. Bacterial suspensions equivalent to 5×10^5 CFU/mL (either with WT or A1408G mutant) prepared from a single colony of each strain from a freshly streaked agar plate into CA-MHBII, were added to the wells containing various AMK and KAN concentrations. The microtiter plates were incubated at 37 °C for 16 to 18 h and MIC was estimated as the lowest concentration of the AMK or KAN that prevented the visible growth of bacteria. The results were interpreted according to the susceptibility breakpoints for AMK (susceptible ≤ 4 $\mu\text{g}/\text{mL}$; resistant ≥ 16 $\mu\text{g}/\text{mL}$) and KAN (susceptible ≤ 16 $\mu\text{g}/\text{mL}$; resistant ≥ 64 $\mu\text{g}/\text{mL}$) in CLSI guidelines. *E. coli* ATCC 25922 was used as a reference quality control strain in all experiments. Experiments were conducted in triplicates (Appendix A Table 2.1).

2.4.7 X-ray crystallographic structure determination

The ribosome complex was formed as previously reported with modifications⁶³. The ribosomes were incubated with 8 μ M 24-MF mRNA in buffer containing 5 mM HEPES-KOH pH 7.5, 10 mM Mg(CH₃COO)₂, 50 mM KCl, 10 mM NH₄Cl, and 6 mM β -ME at 55 °C for 5 min. The tRNA^{Phe} and tRNA^{fMet} were added to a final concentration of 20 μ M and 8 μ M, respectively, and the complex incubated at room temperature for 5 more minutes. Finally, the complex was allowed to reach equilibrium at room temperature for 10 min prior to use in crystallization experiments.

Crystals were grown at 19 °C in sitting drop trays in which 3 μ L of ribosome complex was mixed with 4 μ L of reservoir solution containing 100 mM Tris-HCl (pH 7.6), 150 mM L-Arginine-HCl, 2.9% (wt/vol) PEG 20,000, 9–10.5% (vol/vol) MPD, and 0.5 mM β -ME. Ribosome crystals grew to full size within 7–10 days. The crystals were transferred stepwise into cryo-protectant solutions with increasing MPD concentrations to 40% (vol/vol) and containing 100 mM Tris-HCl pH 7.6, 50 mM KCl, 10 mM NH₄Cl, 10 mM Mg(COOH)₂, 2.9% PEG 20,000, and 100 μ M AMK or KAN in which they were incubated overnight at 19 °C. After stabilization, crystals were harvested and immediately frozen in a nitrogen cryostream at 80 K before being plunged into liquid nitrogen.

Collection and processing of the X-ray diffraction data, model building, and structure refinement were performed as described^{63, 149}. Diffraction data were collected at beamline 24-ID-C and 24-ID-E at the Advanced Photon Source at the

Argonne National Laboratory (Argonne, IL) using NE-CAT remote access software 6.2.0. The final complete datasets of the 70S ribosome-AMK and -KAN complexes were both collected from a single crystal at 100 K with 0.3° oscillations and 0.979 Å wavelength. The raw data were integrated and scaled with the XDS program package¹⁵⁰ (June 17, 2015). The ribosome complex with AMK or KAN, tRNA^{Phe} and tRNA^{fMet} crystallized in the primitive orthorhombic space group $P2_12_12_1$ with approximate unit cell dimensions 210 Å × 450 Å × 620 Å and contained two copies of the 70S ribosome per asymmetric unit of the crystal. The structure was determined by molecular replacement with PHASER from the CCP4 suite¹⁵¹. The search model was generated from the published high-resolution structure of the *T. thermophilus* 70S ribosome with all ligands removed. The initial molecular replacement solution was refined by rigid-body refinement with the ribosome split into multiple domains, followed by five cycles of positional and individual B-factor refinement with PHENIX 1.14¹⁵². After initial refinement, there was clear electron density in the unbiased $F_o - F_c$ difference Fourier maps corresponding to the mRNA, three tRNAs in the A, P, and E sites, and AMK or KAN.

Structural models and restraints for AMK and KAN were generated using PHENIX eLBOW¹⁵³. The mRNA, AMK or KAN, tRNA^{Phe} in the A site, tRNA^{fMet} in the P site, and tRNA^{Phe} in the E site were built into the unbiased difference density map from the initial round of refinement, and the refinement scheme described above was performed after addition of each ligand. The final model of the ribosome complex was generated by multiple rounds of model building in Coot 0.8.9.1¹⁵⁴ and

subsequent refinement in Phenix 1.14¹⁵⁵. The statistics of data collection and refinement for the complex are compiled in the Appendix A Table 2.2.

2.4.8 Cryo-EM data acquisition, image processing, and structure determination

To determine the cryo-EM structure of the *E. coli* 70S-AMK complex with tRNAs, we incubated 2 μM *E. coli* 70S ribosomes purified from strain MRE600 as described in ref. 64, 8 μM 24-MF mRNA, 8 μM fMet-tRNA^{fMet} in 1x ribosome buffer (5 mM Tris-HCl pH 7.4, 60 mM NH₄Cl, 10 mM MgCl₂, 6 mM β -mercaptoethanol) at 37 °C for 10 min. Then, 40 μM AMK was added and the complex was incubated at room temperature for 10 min. Finally, 15 μM Phe-tRNA^{Phe} was added and incubated for an additional 10 min at room temperature.

Quantifoil R2/1 gold 200 mesh grids (Electron Microscopy Sciences) were glow-discharged for 30 s in an (H₂O₂)-atmosphere using the Solarus 950 plasma cleaner (Gatan). Before freezing, the complex was diluted 1.5-fold in the 1x ribosome buffer, resulting in a final concentration of 1.3 μM 70S ribosomes and 25 μM AMK. The mixture (4 μL) was applied onto grids, blotted in 85% humidity at 22 °C for 24 s, and plunged-frozen in liquid nitrogen-cooled ethane using a Leica EM GP2 cryo-plunger. Grids were transferred into a Titan Krios G3i electron microscope (ThermoFisher Scientific) operating at 300 keV and equipped with a K3 direct electron detector camera (Gatan) mounted to a BioQuantum imaging filter operated with an energy filter slit width of 20 eV. Multi-shot multi-hole acquisition was performed by recording five shots per grid hole from nine holes at

a time (3×3), using SerialEM¹⁵⁶ setup to record movies with 41 fractions with a total accumulated dose of $40.58 \text{ e}^-/\text{\AA}^2/\text{movie}$. The nominal magnification was $105,000\times$ and the pixel size at the specimen level was 0.839 \AA . A total of 10,000 image stacks were collected with a defocus ranging between -0.7 and $-2 \mu\text{m}$. The statistics of data acquisition are summarized in Appendix A Table 2.3.

The image stacks (movies) were imported into cryoSPARC 4.1.2¹⁵⁷ and gain corrected. Image frames (fractions) were motion-corrected with dose-weighting using the patch motion correction, and patch contrast transfer function (CTF) estimation was performed on the motion-corrected micrographs. Based on relative ice thickness, CTF fit, length, and curvature of motion trajectories, 9,403 micrographs were selected for further processing (Appendix A Figure 2.8).

1,981,432 particles were picked using the circular “blob” picker in cryoSPARC and were filtered based on defocus adjusted power and pick scores to 1,758,570 particles. Then, 1,435,519 particles were extracted (512×512 -pixel box) and subjected to two rounds of reference-free two-dimensional (2D) classification. After discarding bad particles, 974,230 particles were selected from 2D classification and used to generate the ab-initio volume. Using ‘heterogeneous refinement’ in cryoSPARC with two groups, the 70S-like particles were further classified into one class average. This class represents the 70S ribosome with density for bound tRNAs. The particles (837,845) were binned 2x and were further classified based on focused 3D variability analysis (3DVA)¹⁵⁸ with a spherical mask around the acceptor stem of the P-site tRNA and AMK bound proximal to the CCA-end in the 50S subunit. This approach yielded to one main class containing

234,339 ribosome particles with solid density for the P-site tRNA and AMK bound to the 50S subunit P site. The particles were re-extracted to full-size (512×512-pixel box), followed by non-uniform and CTF refinement in cryoSPARC. The Fourier Shell Correlation (FSC) curves were calculated using the cryo-EM validation tool in Phenix 1.19.2 for even and odd particle half-sets masked with a 'soft mask' excluding solvent¹⁵⁹. The *E. coli* 70S ribosome reconstruction complexed with AMK, mRNA, A-site Phe-tRNA^{Phe}, deacylated P-site tRNA^{fMet}, and deacylated E-site tRNA^{Phe} has a nominal resolution of 2.9 Å using the FSC-cutoff criterion of 0.143 (Appendix A Figure 2.9).

The previous *E. coli* 70S ribosome structure (PDB 8EKC)¹⁴⁹ was used to build the 70S-AMK complex. The individual 30S and 50S subunits were rigid-body docked into the 2.9 Å-resolution EM map using UCSF Chimera 1.14¹⁶⁰. The Phe-tRNA^{Phe} in the A site, tRNA^{fMet} in the P site, the tRNA^{Phe} in the E site were adjusted in Coot 0.9.8.7¹⁵⁴, and AMK was modeled bound to helix h44 and in the P site of the 50S subunit. The complete model of the *E. coli* 70S ribosome, including modified nucleotides in rRNAs and tRNAs, ordered solvent, bound AMK, A-site Phe-tRNA^{Phe}, P-site tRNA^{fMet}, and the E-site tRNA^{Phe} was real-space refined into the EM map for five cycles using Phenix 1.19.2¹⁵⁵ with global energy minimization and group ADP refinement strategies along with base pair restraints for rRNA and tRNAs, together with Ramachandran and secondary structure restraints. The resulting model of the *E. coli* 70S-AMK ribosome complex with Phe-tRNA^{Phe} in the A site, deacylated tRNA^{fMet} in the P site, and deacylated tRNA^{Phe} in the E site was validated using the comprehensive validation tool for cryo-EM in Phenix

1.19.2¹⁵⁵. The cryo-EM data collection, refinement, and validation statistics are compiled in the Appendix A Table 2.3.

2.4.9 Inter-subunit contact surface area at bridge B5

The solvent accessible surface area at inter-subunit bridge B5 ($SASA_{B5}$) was calculated in PyMOL using the refined *T. thermophilus* 70S ribosome structure complexed with AMK. With the magnesium ions and water molecules removed, ribosomal elements and protein uL14 with generated hydrogen atoms within a radius of 15 Å around AMK were considered for the calculations. The interface area at bridge B5 without AMK is given by $SASA_{B5} = (SASA_{B5(30S)} + SASA_{B5(50S)}) - SASA_{B5(30S+50S)}$. Similarly, the interface area with AMK bound is given by $SASA_{B5+AMK} = (SASA_{B5(30S)} + SASA_{B5(50S+AMK)}) - SASA_{B5(30S+50S+AMK)}$.

2.4.10 Figures

All figures showing electron density and atomic models were generated with PyMOL (The PyMOL Molecular Graphics System, Version 2.1.0 Schrödinger, LLC), the chemical structures of AMK and KAN were generated with the ChemDraw Professional version 16.0 software (PerkinElmer Informatics Inc.), and individual panels assembled with Adobe Illustrator (Adobe Inc.).

2.4.11 Data availability

The data supporting the findings of this study are available from the corresponding authors upon reasonable request. The atomic coordinates and structure factors for the crystal structures of the *T. thermophilus* 70S ribosome

complexes have been deposited in the Protein Data Bank (PDB) under the accession codes 8EV6 (70S-AMK) and 8EV7 (70S-KAN). The cryo-EM map of the *E. coli* 70S ribosome bound to AMK has been deposited in the Electron Microscopy Data Bank (EMDB) under the accession code EMD-40882, and the corresponding atomic coordinates in the PDB under the accession code 8SYL. Source data are provided with this paper.

Chapter 3 Mechanistic insights into the alternative ribosome recycling by HflXr¹⁶¹

Chapter adapted with permission from Seely S.M., Basu R.B., Gagnon M.G., Mechanistic insights into the alternative ribosome recycling by HflXr. *Nucleic Acids Research*. 2024 Feb 26:gkae128. doi: 10.1093/nar/gkae128. Epub ahead of print. Erratum in: *Nucleic Acids Res*. 2024 Mar 18;; PMID: 38407413.¹⁶¹

3.1 Introduction

Bacteria have evolved cellular pathways to combat environmental stresses that include a variety of rescue factors, such as the universally conserved GTPase HflX which remobilizes stalled ribosomes ^{1, 94, 95, 106, 162, 163}. In *Escherichia coli*, the *hflX* gene is under the control of heat shock promoters ^{101, 164} and production of HflX restores the translational capacity of the cell ⁹⁴. HflX was shown to recycle 70S ribosomes in a nucleotide-dependent manner and GTP hydrolysis by HflX is required for its release from the 50S subunit ⁹⁴. Cryo-electron microscopy (cryo-EM) studies visualized HflX and the mitochondrial homologue, GTPBP6, bound to the large ribosomal subunit across the aminoacyl (A) and peptidyl (P) sites ^{94, 165-167}, representing a post-splitting state.

Sublethal concentrations of lincosamide and macrolide antibiotics upregulate the expression of HflX in *Mycobacterium abscessus* and *M. smegmatis* ¹⁰⁵. In *M. abscessus*, HflX confers similar levels of resistance to macrolide antibiotics as Erm41, a ribosomal methyltransferase ¹⁰⁶. Similar to the *E. coli* homolog, mycobacterial HflX splits 70S ribosomes into individual subunits ¹⁰⁶. Recently, two homologs of HflX have been identified in *Listeria monocytogenes*, the housekeeping HflX (*Imo1296*), and HflXr (*Imo0762*) which confers resistance

to lincosamides and macrolides ^{110, 166}. The expression of HflXr is upregulated by an attenuation mechanism in response to these classes of antibiotics ^{110, 168} and genomic deletions of HflXr result in the accumulation of 70S ribosomes, suggesting that HflXr recycles antibiotic-stalled ribosomes ⁹⁴. The recent cryo-EM structure of the *L. monocytogenes* HflXr bound to the 50S ribosomal subunit provided insights into the role of its peptidyl transferase center (PTC)-binding loop in conferring antibiotic resistance ¹⁶⁶.

To elucidate the mechanism of HflXr-mediated ribosome dissociation into individual subunits, it is necessary to visualize the 70S ribosome bound to HflXr in the pre-splitting state. Despite the recent capture of short-lived intermediates of the *E. coli* 70S ribosome bound to HflX by cryo-EM ¹⁶⁹, the molecular details by which HflX dissociates the ribosome into subunits remain unclear. Here we follow the splitting reaction of 70S ribosomes by *L. monocytogenes* HflXr using time-resolved cryo-EM (Figure 3.1A-C), revealing a distinct ribosome recycling mechanism employed by HflXr which differs from that used by EF-G and RRF. The high sequence and structural homology of HflXr and HflX, combined with the phylogenetic conservation of HflX in prokaryotes, suggest that the ribosome recycling mechanism reported here is universal in bacteria.

3.2 Materials and Methods

3.2.1 Preparation of 70S ribosomes, HflXr, and deacylated tRNA^{phe}

The full-length *hflXr* gene sequence from *Listeria monocytogenes* (*Imo0762*) was custom synthesized (GenScript, USA) and cloned into the pET21

(Novagen) plasmid containing a C-terminal His-tag. *E. coli* BL21 (DE3) Star (Invitrogen) cells transformed with this construct were grown in the LB medium supplemented with 100 µg/mL ampicillin (Gold Biotechnology) to an absorbance of 0.8 at 600 nm before inducing expression of HflXr-6xHis with 0.5 mM IPTG for 4 hours at 37°C. The cells were collected by centrifugation, flash frozen in liquid nitrogen and stored at –80°C. To purify HflXr, frozen cells were resuspended in the lysis buffer at 4°C (50 mM Tris pH 7.5, 500 mM NaCl, 20 mM imidazole, 1 mM PMSF, 1 mM β-mercaptoethanol) with one EDTA-free protease inhibitor tablet (Pierce, Thermo Scientific). The resuspended cells were lysed by passing several times through an LM20 high-pressure homogenizer (Microfluidics, Westwood, MA) operated at 15,000 psi. Cell debris were removed by centrifugation at 30,624 × g at 4°C for 45 minutes and filtered through a 0.22-µm filter (Millipore). The lysate was then loaded onto a 5 ml HisTrap HP (GE Healthcare) column and washed with a high salt buffer (lysis buffer with 2M NaCl) to remove bound nucleic acids and equilibrated back in lysis buffer. HflXr was eluted with a linear gradient of imidazole to 500 mM. HflXr was further purified by anion exchange (source Q), hydrophobic HiTrap Phenyl HP, and Superdex 200 16/60 (GE Healthcare) chromatography columns. Pure HflXr was concentrated, flash-frozen and stored at –80°C in the buffer containing 10 mM Tris pH 7.5, 300 mM KCl, 200 mM L-Arginine, 5mM EDTA, and 15 mM MgCl₂.

Escherichia coli deacylated tRNA^{Phe} was purified using established procedures ¹⁴⁶. Briefly, tRNA^{Phe} was expressed overnight in *E. coli* JM109 under the constitutive *lpp* promoter, extracted from the cells using phenol-chloroform and

precipitated in 100% ethanol. tRNA^{Phe} was purified by anion exchange source Q (HR 16/10) and reversed-phase chromatography PROTO 300 C4 HPLC (10 x 250 mm) (Higgins Analytical) columns. The unacylated tRNA^{Phe} was then aminoacylated with phenylalanine-tRNA synthetase and purified by reversed-phase HPLC by isolating the shifted peak on the chromatogram corresponding to aminoacylated Phe-tRNA^{Phe} on the C4 column. Phe-tRNA^{Phe} was then deacylated in 100 mM Tris pH 8.0 and re-purified on the C4 column.

The 21-mer F-stop (21F-stop) mRNA, containing a Shine-Dalgarno sequence and the Phe codon in the P site, with the sequence 5' GGC AAG GAG GUA AAA **UUC** UAA 3' (Phe codon in bold), was chemically synthesized by Integrated DNA Technologies (Coralville, IA). *Listeria innocua* cells (ATCC 33090) were grown in the brain heart infusion (BHI) medium at 37 °C for 4 hours to an absorbance of 0.6 at 600 nm. The cells were then pelleted by centrifugation at 17,500 × g for 15 minutes, flash frozen in liquid nitrogen, and stored at –80°C until used to isolate 70S ribosomes. Briefly, the cells were washed and lysed in buffer A (50 mM Tris-HCl pH 7.6, 10 mM MgCl₂, 100 mM NH₄Cl, 0.5 mM EDTA and 6 mM β-mercaptoethanol) using an LM20 high-pressure homogenizer (Microfluidics, Westwood, MA). The lysate was cleared by centrifugation at 39,000 × g for 30 minutes at 4°C and filter-sterilized through a 0.45 μm filter and stored at –80°C. To isolate ribosomes, the lysate was layered on a 1.1 M sucrose cushion buffer (10 mM Hepes pH 7.6, 100 mM NH₄Cl, 14.5 mM MgCl₂, 0.5 mM EDTA, 6 mM β-mercaptoethanol) and spun at 214,573 × g in a Type 45Ti rotor (Beckman) for 20 hours at 4°C. Ribosome pellets were resuspended in 10 mM Hepes pH 7.6, 100

mM NH₄Cl, 14.5 mM MgCl₂, 0.5 mM EDTA, 6 mM β-mercaptoethanol. Ribosomes were then purified through 10-50% sucrose density gradients in a SW32 rotor (Beckman) at 58,971 × g at 4°C for 19 hours. The fractions containing 70S ribosomes were collected, diluted to adjust Mg²⁺ concentration to 10 mM and concentrated by centrifugation at 214,573 × g at 4°C. Pure 70S ribosomes were resuspended and brought to the final buffer 10 mM Hepes pH 7.6, 60 mM NH₄Cl, 15 mM KCl, 10 mM MgCl₂, flash-frozen in liquid nitrogen and stored at –80°C.

3.2.2 Rapid-kinetics measurements

The dissociation of 70S ribosomes into subunits was monitored using Rayleigh light scattering at 435 nm with a 400 nm cut off filter using a stopped-flow apparatus (Applied Photophysics, UK). Experiments were performed in buffer containing 10 mM Hepes pH 7.6, 60 mM NH₄Cl, 15 mM KCl, and 5 mM MgCl₂. 70S ribosomes (0.05 μM) were rapidly mixed with 0.5 μM of HflXr in the presence of 500 μM of nucleotide (ATP, GDP, GTP, or GDPCP) at 37°C or 20°C. Control reactions were performed in the absence of nucleotide and HflXr. All concentrations are final after mixing. The reaction was recorded for at least 120 seconds and data fitting was performed on normalized curves obtained by averaging 5-8 traces using GraphPad Prism version 9.5.1 for Windows, GraphPad Software, www.graphpad.com.

3.2.3 Sample preparation, cryo-electron microscopy and data acquisition

Ribosome complexes were programmed using 2 μM *L. innocua* 70S ribosomes, 10 μM 21F-stop mRNA, 10 μM deacylated-tRNA^{Phe} incubated in final 70S buffer (10 mM Hepes pH 7.6, 60 mM NH₄Cl, 15 mM KCl, 10 mM MgCl₂, 1 mM β -mercaptoethanol) at 37°C for 15 minutes. This complex was used to freeze grids for the 0 second sample in the absence of HflXr. The same complex was then prepared with 40 μM HflXr and 1 mM GDPCP (Millipore Sigma) at room temperature (~22°C) and 4 μL aliquots of the complex was applied to EM grids and plunge-frozen in liquid nitrogen-cooled ethane at 160 seconds and 600 seconds to obtain grids for the respective time points. Quantifoil R2/1 gold 200 mesh grids (Electron Microscopy Sciences) pre-cleaned and glow-discharged for 30 seconds in a Solarus 950 plasma cleaner (Gatan) were used to apply 4 μL sample, blotted for 24 seconds at 22°C and 85% humidity before freezing using a Leica EM GP2 cryo-plunger. Grids were transferred into a Titan Krios G3i electron microscope (Thermo Fisher Scientific) operating at 300 keV and data acquired with a Falcon III direct electron detector (Thermo Fisher Scientific). Data collection for all three datasets at 0, 160 and 600 seconds were acquired with similar parameters. The image stacks (movies) were acquired with a pixel size of 0.85 Å/pixel using the EPU software (ThermoFisher Scientific) to record movies with 40 fractions with a total accumulated dose of ~40 e⁻/Å²/movie. A total of 7,572 (0 second), 10,151 (160 seconds) and 10,446 (600 seconds) image stacks were collected for the respective

time-resolved datasets with defocus values ranging between -1.0 to -2.3 μm . The statistics of data acquisition are summarized in the Supplementary Table S1.

3.2.4 Cryo-electron microscopy image processing

Data processing for all three datasets was done in cryoSPARC 4.1.0¹⁵⁷. The image stacks were collected and imported into cryoSPARC, where the image frames (fractions) were motion-corrected with the patch motion correction job, followed by patch contrast transfer function (CTF) estimation. Based on relative ice thickness, CTF fit, and length and curvature of motion trajectories, 7,525 (0 second), 10,065 (160 seconds) and 10,337 (600 seconds) micrographs were selected for further processing.

0 second dataset – 821,331 particles were picked using the circular ‘blob’ picker in cryoSPARC and filtered based on defocus adjusted power and pick scores. Particles were subjected to reference-free two-dimensional (2D) classification. After discarding bad 2D classes, selected particles were used to generate *ab-initio* volumes which upon ‘heterogeneous refinement’ yielded three main class averages of 70S ribosomes. Class average 1 consisted of 282,602 particles which gave a reconstruction of the 70S ribosome in the classic non-rotated state, class average 2 consisted of 177,879 particles yielding a reconstruction of the 70S ribosome with a swiveled 30S head domain and bound to deacylated-tRNA^{Phe} in the pe/E state. Class average 3 contained 120,066 particles and yielded a 70S ribosome volume with poor density for the 30S subunit.

The other class contained 26,571 particles which did not provide meaningful reconstructions and were discarded.

Class average 3 was further classified to yield more 70S ribosome particles in the non-rotated state (20,668 particles), and the head-swiveled conformation bound to pe/E-tRNA^{Phe} (19,007 particles) which were pooled, respectively, with particles from class average 1 resulting in a total of 303,270 particles (class average I-A), and with particles from class average 2 resulting in 196,886 particles (class average I-B). The other two classes from this step sorted out 50S subunit particles (25,492) and 70S ribosome particles with a ratcheted 30S subunit (7,857). Particles from the final class averages I-A and I-B were extracted with a box size of 512 × 512 pixels and processed using 'non-uniform refinement' in CryoSPARC 4.1.0 yielding reconstructions with a nominal resolution of 3.0 Å for 70S ribosomes in the classic non-rotated state, which we named structure I-A, and 3.0 Å for the class with the head-swiveled 70S ribosomes bound to pe/E-tRNA^{Phe}, which we named structure I-B. The map of structure I-A was sharpened using a B-factor of -85 and structure I-B with a B-factor of -90. Multibody refinement of the head domain of the 30S subunit of structure I-B yielded a local reconstruction of 3.0 Å.

160 seconds dataset – 1,009,110 particles were picked using the 'blob' picker, filtered based on defocus adjusted power and pick scores and particles subjected to reference-free 2D classification. After discarding bad 2D classes, 802,665 particles were used for *ab-initio* reconstruction followed by 'heterogeneous refinement' that sorted the particles into four ribosome classes: class average 1 contained 189,943 particles of 70S ribosomes in classic (non-

rotated) state, and bound to P and E site tRNA; class average 2 contained 125,796 particles of 70S ribosomes with the 30S head-swiveled, and bound to deacylated pe/E-tRNA and HflXr; class average 3 contained 150,564 particles of ratcheted 70S ribosomes, and bound to HflXr and p/E-tRNA; class average 4 contained 298,789 particles of 50S subunits. The last class with 37,573 particles did not yield anything meaningful and were considered not specimen-related particles which were discarded from further processing.

Further classification of the particles in the class average 1 containing classic 70S ribosomes (non-rotated) using a spherical mask around the P- and E-tRNA unexpectedly yielded a class of 38,285 particles with strong density for HflXr, and another class of 57,518 particles of classic non-rotated 70S ribosome with P- and E-site tRNA. We then used a soft mask focused on HflXr to sort out 10,742 particles of empty 70S ribosomes, leaving a final pool of 27,543 particles with strong density for HflXr and containing HPF bound to a non-rotated 70S ribosome, which upon refining with non-uniform refinement resulted in a reconstruction with a nominal resolution of 3.2 Å (structure II-B). Multibody refinement combined with particle subtraction of the 30S head, 30S body, and HflXr yielded focused maps with nominal resolutions of 3.3 Å, 3.3 Å and 3.8 Å, respectively (figs. S5, S6). The maps were combined into a composite map using the `combine_focused_maps` job in PHENIX 1.19.2 ¹⁵².

Particles in the class average 2 comprising of HflXr-bound 70S particles with the head-swiveled were further classified with a soft mask focused on HflXr to isolate particles with solid density for HflXr. This classification yielded 55,099

particles containing 70S ribosomes with the 30S head-swiveled and solid density for HflXr and pe/E-tRNA, which was further refined by non-uniform refinement to a nominal resolution of 3.1 Å (structure II-C). Local refinements with signal subtraction were performed on the 30S head, 30S body, and HflXr to improve the local resolutions of these regions, resulting in local maps of the 30S head refining to 3.6 Å, 30S body to 3.2 Å and HflXr to 3.0 Å that were all combined into a composite map using the `combine_focused_maps` job in PHENIX 1.19.2¹⁵². The above particle classification also gave a class of 36,682 particles of 70S ribosomes with the 30S head swiveled and bound only to pe/E-tRNA, and a class of 34,015 particles with poor density for HflXr and tRNA, which were both discarded.

Class average 3 contained HflXr-bound to ratcheted 70S ribosomes and was similarly classified with a soft mask around HflXr to sort the particles based on the presence of HflXr. The best density of HflXr was found in a class of 80,381 particles of ratcheted 70S ribosomes with the 30S head swiveled and bound to deacylated pe/E-tRNA^{Phe}. These particles were refined by non-uniform refinement to a nominal resolution of 3.1 Å (structure II-D). Focused refinement with signal subtraction was performed on sub-regions, which improved the resolution of the 30S head to 3.4 Å, 30S body to 3.1 Å and HflXr to 3.0 Å. 15,497 particles from this classification contained ratcheted 70S ribosomes bound to p/E-tRNA but without HflXr. The reconstruction from this class was refined to a resolution of 3.3 Å (structure II-A), which has been used as a HflXr-free ratcheted 70S ribosome reference structure for comparison with structure II-D. The volume for structure II-A was also used for focused refinement of the 30S head and body, resulting in

local resolutions of 3.6 Å and 3.5 Å respectively. 14,570 particles from class average 3 (ratcheted 70S ribosome) showed weak density for HflXr and were discarded. To aid in model-building, the global and local refinement maps were sharpened in cryoSPARC with B_{sharpen} as indicated in the Supplementary Table S4 and below the respective classes in the workflow for each dataset (figs. S2, S5, and S9). Locally refined maps were combined with the global refinement map using the 'combine focused maps' tool in PHENIX 1.19.2 ¹⁵².

600 seconds dataset – 912,156 particles were picked using the 'blob' picker, filtered based on defocus adjusted power and pick scores and subjected to reference-free 2D classification. After discarding bad 2D classes, *ab-initio* reconstruction followed by 'heterogeneous refinement' identified three class averages; class average 1 contains 445,279 particles of 50S ribosomal subunits bound to HflXr, class average 2 contains 299,389 particles of 70S ribosomes with the 30S head domain swiveled and bound to HflXr, and class average 3 containing 79,818 particles of non-rotated 70S ribosomes bound to HflXr. The 70S ribosome class averages 2 and 3 particles were pooled and further classified using a soft mask on the 30S subunit. This classification further sorted out 50S subunit particles bound to HflXr (35,136), 70S ribosomes with the 30S head-swiveled and bound to HflXr (28,135), non-rotated 70S ribosomes with the 30S head-swiveled and no HflXr (146,519), and non-rotated, non-swiveled 70S ribosome particles with no HflXr (143,956). The 70S ribosome particles from this dataset essentially represent structures I-A, I-B, and II-C from the 0 and 160-second datasets and were therefore not processed further. 3D classification of the particles in class

average 1 using a mask on HflXr sorted out 53,944 particles of 50S subunits without HflXr, 297,377 particles of 50S subunit bound to HflXr, and 93,958 particles of 50S subunit with weak density for HflXr. The 50S subunit particles bound to HflXr were pooled (332,513) and refined using non-uniform refinement to a nominal resolution of 2.7 Å (structure III). All EM maps (overall, focused and composite) generated in this study are listed in Supplementary Table S4, together with their resolution, sharpening B factor, and number of particles.

3.2.5 Model building and refinement

The structure of the *L. innocua* 70S ribosome was first built in the 3.0 Å reconstruction of the non-rotated 70S ribosome structure I-A density map, using a model of the *Listeria monocytogenes* 70S ribosome structure from PDB 7NHN¹⁷⁰ docked as a rigid body using the 'Fit to Map' feature in UCSF Chimera 1.14¹⁶⁰. The sequences of several ribosomal proteins and ribosomal RNAs were revised according to the genomic sequence of the *L. innocua* strain ATCC 33090 (GenBank CP117229.1) as indicated in the Supplementary Table S6 and were correspondingly remodeled into the density map. A model-to-map fit of each nucleotide in the 16S, 23S, and 5S rRNAs was inspected visually and were corrected for their *anti* or *syn* conformations for a better fit into the EM density map. The model of tRNA^{Phe} was rigid-body fit into the EM density (pe/E state in structure I-B) and adjusted in Coot 0.9.8.7¹⁵⁴. The model of the head domain of the 30S subunit was separated and rigid-body fit into the density for the swiveled position (structure I-B). The empty 70S ribosome in the ratcheted conformation (structure II-A) was similarly modeled by rigid-body fitting the 30S subunit. The HflXr-free

models of structures I-A, I-B and II-A were then fit into volumes of structures II-B, II-C and II-D, respectively. The initial model of *L. innocua* HflXr was generated using AlphaFold2 ¹⁷¹, and rigid-body fit into the locally refined map of structures II-B, II-C, and II-D, and then real-space refined in Coot 0.9.8.7 ¹⁵⁴. The 50S subunit model and HflXr from structure II-B were rigid-body fit into the map of structure III in Coot 0.9.8.7 ¹⁵⁴. After initial rigid-body fit into the respective densities, the models were all refined by phenix.real_space_refinement in PHENIX 1.19.2 ¹⁵². Magnesium ions and water were modeled into relevant densities in Coot 0.9.8.7 ¹⁵⁴. The final models with ordered solvent were real-space refined in PHENIX 1.19.2 ¹⁵⁵ including global energy minimization and group ADP refinement strategies along with base-pair restraints for rRNA and tRNA^{Phe}, together with Ramachandran and secondary structure restraints. Resulting models were validated using the comprehensive validation tool for cryo-EM in PHENIX (Supplementary Table S1). The extent of 30S head swiveling was determined by aligning the 30S body of structures to structure I-A in PyMOL using the angle_between_domains script (https://pymolwiki.org/index.php/Angle_between_domains). The difference vectors between P and C α atoms in Figures 3.3 and 3.4 were calculated using the PyMOL modevectors.py script (<https://raw.githubusercontent.com/PyMol-Scripts/PyMol-script-repo/master/modevectors.py>).

3.2.6 PISA calculations

Buried surface area measurements were done using PISA (<https://www.ebi.ac.uk/pdbe/pisa/>). Hydrogen bonds, salt-bridges and buried

surface area for each structure was measured and pairwise comparisons between structures are tabulated as % differences (Figure 3.3D-F; Supplementary Tables S2, S3).

3.2.7 Figure generation

All figures showing atomic models were generated using PyMOL (The PyMOL Molecular Graphics System, Version 2.0 Schrödinger, LLC) or ChimeraX 1.5¹⁷² and assembled with Adobe Illustrator (Adobe Inc.). Supplementary Movie S1 was made in ChimeraX 1.5¹⁷².

3.3 Results

3.3.1 HflXr-mediated ribosome recycling visualized by time-resolved cryo-EM

The high homology of HflXr in the non-pathogenic *L. innocua* and the close relative pathogenic *L. monocytogenes* (96% sequence identity) (Appendix B Figure 3.14), and of ribosomal RNA and r-proteins (Appendix B Table 3.6), prompted us to use *L. monocytogenes* HflXr and 70S ribosomes isolated from *L. innocua*. We assessed the influence of the nucleotide identity and temperature on the ribosome recycling kinetics by HflXr using a stopped-flow apparatus (Figure 3.1A; Appendix B Figure 3.1). The dissociation of 70S ribosomes into subunits by HflXr is monitored by the decrease in Rayleigh light scattering as a function of time (Figure 3.1A)^{94, 104, 173}. In the presence of ATP, HflXr does not recycle ribosomes, seemingly at odds with the reported ATP-dependent ribosome dissociation activity

recycling and their assignment as pre-HflXr binding, intermediates, and post-splitting. Maps are colored to show the 50S subunit (blue), 30S subunit body domain (yellow), 30S subunit head domain (gold), HflXr (pink), HPF (purple), tRNA (green), and mRNA (cyan). **(D)** The NTD of HflXr (pink) bound to the cleft formed by H69 and H71 in the 50S subunit in structure II-C. In structure I-B (gray), H69 would collide with HflXr, resulting in the displacement of H69 with a concomitant movement of the platform domain of the 30S subunit away from the 50S subunit.

The loss of amplitude of scattered light in both experimental conditions is similar, indicating that the dissociation of ribosomes into subunits mediated by HflXr proceeds to completion despite the lower temperature of the reaction (Figure 3.1A). We, therefore, used the kinetic parameters determined at 20 °C to guide the freezing of the cryo-EM grids. Three time points along the ribosome dissociation reaction coordinates were selected for cryo-EM analysis: 0, 160, and 600 seconds. In *E. coli*, HflX efficiently recycles ribosomes programmed in the post-release state containing a deacylated-tRNA in the P site ⁹⁴, similar to the mitochondrial homolog GTPBP6 ¹⁷⁴. To mimic such a ribosome complex, we correspondingly programmed 70S ribosomes with a deacylated-tRNA^{Phe} bound in the P site ⁹⁴, to which *L. monocytogenes* HflXr and GDPCP were added. Initial data processing shows that the population of 70S ribosome particles decreased at each time point from 95% to 44%, and conversely the 50S subunit particles increased from 5% to 56% (Figure 3.1B).

Prior to the addition of HflXr (0 second; dataset I), classification of the particles yielded two ribosome populations, one in the classical state lacking tRNA and bound to the hibernation promoting factor (HPF) (structure I-A), and one with the head domain of the 30S subunit swiveled by ~18° and tRNA^{Phe} in the pe/E hybrid state of binding (structure I-B) (Figure 3.1C; Appendix B Figures 3.2, 3.3

and 3.4A; Appendix B Table 3.1). At the 160 second-time point (dataset II), 163,023 particles are 70S ribosomes in three distinct states and bound to HflXr, representing pre-splitting ribosome complexes (Figure 3.1C; Appendix B Figures 3.5, 3.6, and 3.7; Appendix B Table 3.1). Ribosomes in class average II-B are non-rotated and contain HPF, class II-C lacks HPF and the 30S head domain is swiveled by $\sim 14^\circ$ and in II-D, the 30S subunit is rotated by $\sim 9^\circ$ and the head domain swiveled by $\sim 12^\circ$ (Figure 3.1C; Appendix B Figures 3.4B, 3.5, and 3.8A-C). Ribosome II-A is rotated and lacks HflXr (Figure 3.1C; Appendix B Figures 3.4B and 3.5). This dataset also contains 298,789 particles which are 50S subunits bound to HflXr, consistent with the notion that the non-hydrolysable analog of GTP, GDPCP, interferes with the dissociation of HflXr from the large ribosomal subunit following splitting of the ribosome ⁹⁴. At 600 seconds (dataset III), the population of 50S subunits (480,415 particles) surpasses that of 70S ribosomes (379,207 particles), which allowed to refine the 50S•HflXr complex to a nominal resolution of 2.7 Å (Figure 3.1C; Appendix B Figures 3.8D, 3.9, and 3.10; Appendix B Table 3.1).

3.3.2 HflXr dismantles the non-rotated ribosome

The analysis of the integrity of the twelve inter-subunit bridges in the HflXr•70S complexes elucidates the mechanism of ribosome dissociation by HflXr (Appendix B 3.11). The binding site of HflXr on the 70S ribosome at 160 seconds in structures II-B, II-C, and II-D is consistent with that seen in the previous 50S-complex structures ^{94, 165, 166, 175} (Appendix B Figure 3.12B). The largest effects of HflXr on the integrity of the bridges are observed in the absence of HPF in structure

II-C, in which the ribosome is non-rotated and the head domain of the 30S subunit is swiveled (Appendix B 3.2).

In contrast to the mode of action of RRF and EF-G ^{1, 31-33, 43, 44, 53, 61, 63, 76}, binding of HflXr to the 70S ribosome does not initially disrupt the central inter-subunit bridge B2a mediated by the contact between helices H69 in the 50S subunit and h44 in the 30S subunit (Figure 3.2A-C; Appendix B Tables 3.2 and 3.3). Despite the close interaction between the N-terminal subdomain I (NTD-I) of HflXr and H69 in complex II-C, the buried surface area by bridge B2a is unchanged relative to the equivalent ribosome lacking HflXr (I-B) (Figure 3.3A, D; Appendix B Table 3.2). The NTD-I of HflXr locates in the cleft formed by H69 and H71 of the 23S rRNA (Figure 3.1D). Several basic and polar residues interact with the phosphate backbone of H69 near nucleotides 1939-1943 and 1948-1951 (Appendix B Figure 3.14). The importance of these interactions is substantiated by a truncation of the NTD-I that inactivates the ribosome splitting activity of the *E. coli* and *M. smegmatis* HflX ^{94, 106}. The interaction between the NTD-I of HflXr and H69 results in a displacement of H69 and h44 by ~4 Å toward the platform domain of the 30S subunit, maintaining the conserved A-minor interactions with h44 (Figs. 3.1D, 3.2A). The observation that the integrity of bridge B2a is maintained in our structures suggests that HflXr catalyzes ribosome recycling by a mechanism that is distinct from that mediated by RRF and EF-G, which together ablate bridge B2a (Appendix B Figure 3.12A) ^{1, 31-33, 43, 44, 53, 61, 63, 76}.

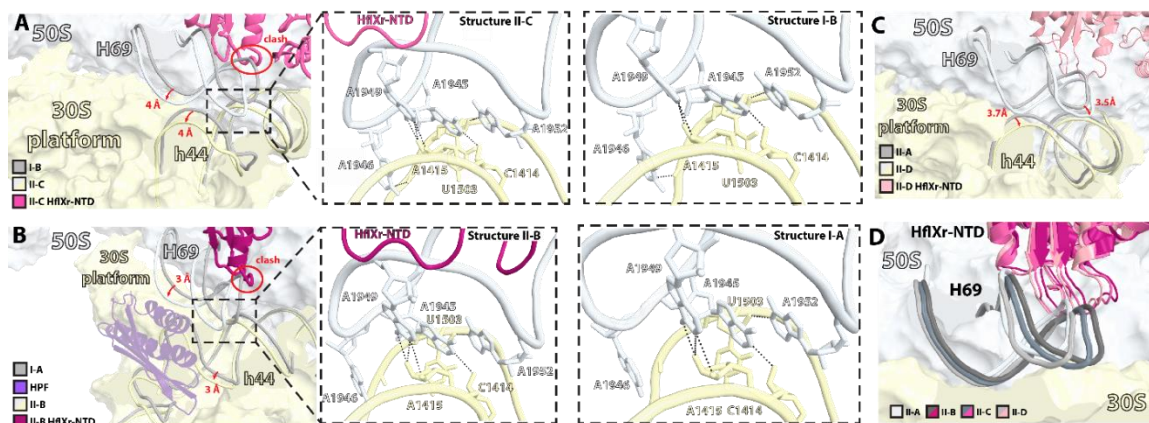


Figure 3.2 HflXr displaces H69 and h44 without disrupting bridge B2a. (A) (left) Binding of HflXr (pink) to structure II-C near bridge B2a causes displacement of H69 (white) from its position in I-B (gray), resulting in an approximately equal displacement of h44 (yellow) toward the 30S platform domain. Conserved hydrogen bond interactions in bridge B2a in the presence (center; II-C) or absence (right; I-B) of HflXr. (B) (left) Despite the presence of HPF (purple) in II-B, HflXr (pink) causes a similar movement of bridge B2a. The integrity of the bridge is maintained irrespective whether HflXr is bound (center; II-B) or not (right; I-A) (C) Binding of HflXr (pink) in II-D near bridge B2a results in approximately equal displacement of H69 (white) and h44 (yellow) from their positions in II-A (gray) (D) Binding of HflXr to the 70S ribosome in structures II-B, II-C, and II-D positions H69 similar to that in the rotated state II-A without HflXr.

To estimate the stability and strength of the remaining eleven inter-subunit bridges, we calculated the contact area for each bridge using the protein interface, surfaces, and assemblies (PISA) service of the European Bioinformatics Institute (Figure 3.3D-F) ¹⁷⁶. Helix h44 in the 30S subunit spans the entire length of the body domain and participates in several inter-subunit bridges. Despite the fact that the NTD-I of HflXr displaces H69 in structure II-C, which in turn pushes the top of h44, bridges B3, B5, and B6 along h44 do not exhibit significant losses in surface area (Figure 3.3D; Appendix B Figure 3.11; Appendix B Table 3.2), indicating that the overall conformation of h44 is unaltered. Whereas the buried surface area around bridge B6 is reduced, this can be attributed to a lower resolution of protein bL19 in structure II-C which did not allow to visualize side chains (Appendix B

Figure 3.13A-B). However, the peptide backbone of bL19 remains still, suggesting that bridge B6 is unchanged by the binding of HflXr in structure II-C (Appendix B Figure 3.13C). Visual inspection of structures I-B and II-C shows that the displacement of the top region of h44 caused by HflXr emanates into a large-scale movement of the adjacent helices in the platform domain of the 30S subunit, leaving the body domain essentially unaltered (Figure 3.3A, D; Appendix B Figure 3.11B). Despite the preservation of bridges B2a, B3, B5, B6, and B8 in structure II-C, the total loss of inter-subunit contact area is $\sim 1282 \text{ \AA}^2$ (Figure 3.3D; Appendix B Table 3.2), indicating that HflXr disrupts more than 23% of the interactions that hold the ribosome together. The swiveled conformation and flexibility of the head domain of the 30S subunit in both structures I-B and II-C resulted in poor electron density for this region and therefore, precluded the analysis of bridges B1a, B1b, and B1c.

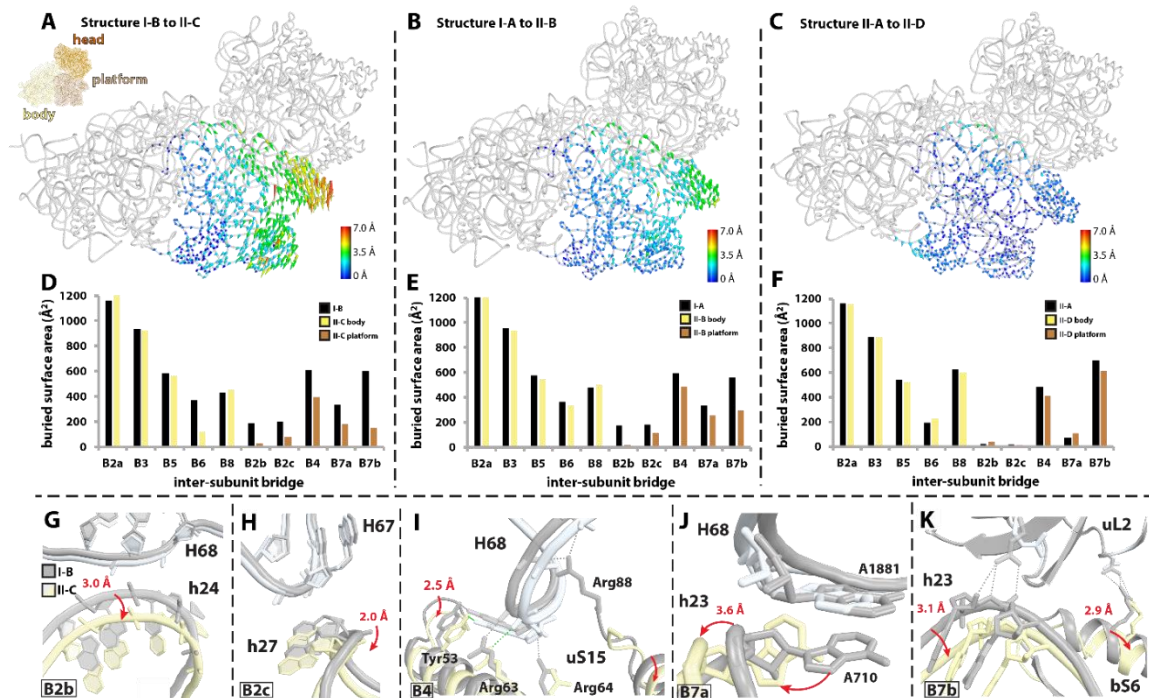


Figure 3.3 HflXr induces conformational changes in the platform domain of the 30S subunit that break multiple inter-subunit bridges. Effect of HflXr binding to the 70S ribosome shown as difference vectors for P and C α atoms of the 30S platform domain, colored by distance. The displacement vectors are drawn between the empty and HflXr-bound head swiveled states, structures I-B and II-C (**A**), classic non-rotated states bound to HPF, structures I-A and II-B (**B**), and the ratcheted states, structures II-A and II-D (**C**), respectively, superposed on the 30S subunit of the starting structures I-B, I-A and II-A (gray ribbon). The buried surface area between subunits was determined by PISA for each 70S ribosome state, non-rotated with the 30S head domain swiveled I-B and II-C (**D**), classic non-rotated with HPF I-A and II-B (**E**), and ratcheted II-A and II-D (**F**). (**G-K**) Inter-subunit bridges of the 30S subunit platform domain (B2b, B2c, B4, B7a, B7b) are disrupted in II-C (white 50S and yellow 30S) through displacement of 16S rRNA helices and ribosomal proteins from their position in I-B (gray) due to large scale conformational changes in the platform domain of the 30S subunit caused by HflXr. Putative hydrogen bonds are indicated with dashed grey (I-B) and green (II-C) lines.

In structure II-C, ~85% (~1098 Å²) of the total loss (~1282 Å²) of contact area is attributed to the disruption of the bridges localized to the 30S platform domain, B2b, B2c, B4, B7a, and B7b (Figure 3.3D; Appendix B Figure 3.11B; Appendix B Table 3.2). The HflXr-mediated movement of the apical part of h44 causes the proximal helices h23, h24, h27, and h45 in the platform domain to shift away from the 50S subunit, disrupting inter-subunit bridges and leading to the dissociation of the ribosome (Figure 3.3A, G-K; Appendix B Tables 3.2 and 3.3). Bridge B2b, which is proximal to B2a, consists of interactions between the stem of h24 in the 30S subunit and the base of H68 in the 50S subunit. In the absence of HflXr in structure I-B (0 second), the phosphate backbone of h24 (nucleotides 790-792) is within interaction distance of H68 (nucleotides 1868-1870). In structure II-C (160 seconds), HflXr causes h44 and h45 to shift toward and displace h24 by ~3 Å away from H68, destroying bridge B2b (Figure 3.3G). The adjacent bridge B2c, formed by interactions between the phosphate backbone of H67 (nucleotides

1864-1866) and the minor groove of the tetraloop capping h27 (nucleotides 908-909), is dissolved through the movement of h44, h45 and h27 caused by HflXr (Figure 3.3H). The importance of bridge B2c is substantiated by findings that perturbations of the phosphate backbone in h24, which interacts with h27 and considered a part of bridge B2c, interfere with subunit association ¹⁷⁷.

At the edge of the platform domain, ribosomal protein uS15 contacts the loop region of H34 forming bridge B4. In structure I-B (0 second), the side chains of residues Tyr53, Arg63, Arg64, and Arg88 in protein uS15 form five hydrogen bonds with nucleotides G759, U760, and A761 in H34. In structure II-C (160 seconds), uS15 is displaced through its interactions with h23 and h24 resulting in the loss of hydrogen bonds between Arg63, Arg64, and Arg88 and H34 (Figure 3.3I; Appendix B Table 3.3) Although the specific interactions between uS15 and H34 are not conserved, the presence of bridge B4 is essential for optimal subunit association ¹⁷⁸.

Bridge B7a links the 30S platform and the uL1-stalk of the 50S subunit through interactions between h23 and H68. In structure I-B (0 second), nucleotide A710 in h23 flips and interacts with H68, including stacking with nucleotide A1881. At 160 seconds (II-C), h23 shifts away from H68 resulting in the loss of B7a (Figure 3.3J; Appendix B Table 3.3). The displacement of h23 can be traced back through the network of intra-30S subunit movements of adjacent helices in the platform domain. HflXr moves H69, shifting h44 and h45 in the 30S subunit, which then permeates to the nearby h24 that interacts with the loop region of h23 near bridge B7a. Bridge B7b is made up of contacts between the stem of h23 and protein uL2

as well as interactions between uL2 and bS6. Proteins uL2 and bS6 interact together, and nucleotides A720 and G721 of 16S rRNA interact with uL2. The shift of h23 and bS6 observed in structure II-C results in the loss of all hydrogen bonds destroying B7b (Figure 3.3K; Appendix B Table 3.3).

Despite the presence of HPF bound to classical state ribosomes I-A (0 second) and II-B (160 seconds), HflXr induced similar rearrangements in the 30S subunit of structure II-B (Figure 3.3B). Bridge B2a is also preserved with H69 and h44 being displaced toward the 30S head domain, as observed in complex II-C (Figure 3.2A, B). However, the total loss of buried surface area in structure II-B relative to I-A is only $\sim 717 \text{ \AA}^2$ ($\sim 13\%$) (Figure 3.3E; Appendix B Tables 3.2 and 3.3), consistent with the function of HPF at stabilizing the 70S ribosome and protecting it from subunit dissociation ¹⁷⁹⁻¹⁸². The structural rearrangements in the decoding center mediated by HPF further provide a structural basis for the reported increased tolerance of *L. monocytogenes* stationary-phase cultures to aminoglycoside antibiotics (Appendix B Figure 3.12E) ¹⁸³.

3.3.3 The rotated ribosome bound to HflXr remains intact

The 160-second dataset contains two additional class averages in which the ribosome is rotated. Structure II-A contains p/E-tRNA^{Phe}, whereas structure II-D is bound to a pe/E-tRNA^{Phe} and to HflXr (Figure 3.1C; Appendix B Figure 3.5). Relative to structure II-A, binding of HflXr in II-D resulted in a total loss of buried surface area of $\sim 116 \text{ \AA}^2$ ($\sim 2.5\%$) (Figure 3.3C, F; Appendix B Table 3.2), which is substantially less than in the non-rotated ribosome. Bridge B3, near the pivot point

of the 30S subunit rotation, and bridges B5, B6, and B8 in the 30S body domain, are maintained (Appendix B Tables 3.2 and 3.3), whereas bridges B1a, B1b, and B1c in the 30S head domain are highly variable, in line with previous studies ^{30, 57, 184}.

It is remarkable that the position of H69 in the non-rotated 70S•HflXr complexes (II-B, II-C) is similar to that in the rotated 70S ribosome structures (II-A, II-D) independently whether HflXr is associated (II-D) or not (II-A) (Figure 3.2D). In the rotated ribosome, the displacement of H69 is mitigated by the concomitant displacement of h24 and h45 away from H69 caused by the natural rotation of the 30S subunit (Figures 3.3C, 3.4A-C), explaining the lesser influence of HflXr on the inter-subunit bridges in structure II-D. This observation indicates that the binding of HflXr to the rotated ribosome is transiently stable and hints at the possibility that the rotated ribosome is the substrate for HflXr. The niche created between H69 and H71 in the rotated ribosome allows the NTD-I of HflXr to bind proximal to H69, suggesting that the association of HflXr with the rotated ribosome is energetically more favorable relative to the non-rotated state.

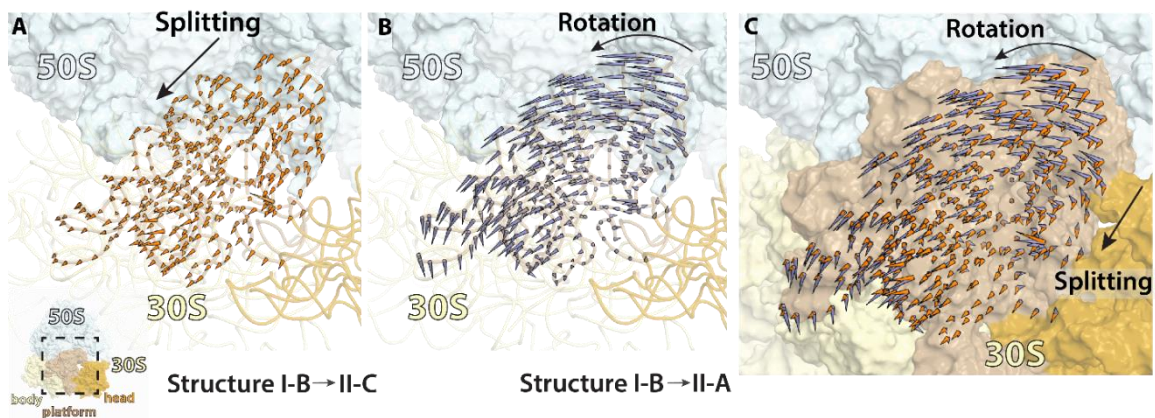


Figure 3.4 Comparison of the direction of movement of the 30S platform in canonical ribosome ratcheting and HflXr-mediated recycling. (A) The surface overview of the 70S ribosome is shown with the 50S subunit colored in light blue, the body of the 30S subunit in light yellow, the platform domain of the 30S subunit in light brown, and the 30S head in yellow orange. Magnified view of the 70S ribosome is indicated in the box, and includes a part of the 50S subunit (light blue) and 16S cartoon or surface colored according to the scheme in the overview figure (A-C). Difference vectors drawn between P atoms of the 30S platform of structure I-B and HflXr-bound structure II-C, represented as orange vectors (A and C), show the orthogonal movement of the 30S platform away from the 50S subunit. Difference vectors for the same atoms drawn between structures I-B (non-rotated) and II-A (rotated) in blue gray (B and C), show the classic ratcheting movement of the 30S subunit along the 50S subunit, which is nearly perpendicular to the HflXr-mediated movement of the 30S platform (C). Labeled black arrows denote the overall direction of the movements.

3.3.4 Structure of the post-splitting 50S subunit complexed with HflXr

After 600 seconds in the presence of HflXr and GTPCP, the majority of ribosomes have dissociated into subunits (Figure 3.1A, B). This allowed to visualize HflXr trapped on the 50S subunit post-splitting at a nominal resolution of 2.7 Å (Figure 3.1C; Appendix B Figures 3.8D, 3.9, and 3.10)^{94, 166}. The conformation of HflXr in structure III is similar to that seen in the recently reported 50S•HflXr complex with an RMSD value of 1.6 Å between equivalent C α atoms (Appendix B Figure 3.12C)¹⁶⁶. The relative position of HflXr bound to the 70S ribosome (II-C) and the 50S subunit (III) provides further insights into how HflXr promotes dissociation of the subunits. The alignment of the 23S rRNA in both complexes reveals that HflXr rotates by $\sim 5^\circ$ toward its C-terminal domain (CTD) about the axis created by its helix-loop-helix NTD subdomain II, causing a displacement of NTD-I by ~ 3 Å toward H69 (Figure 3.5A). In structure III, the

absence of the 30S subunit allows H69 to be pushed by ~ 9 Å further away from the 50S subunit relative to the 70S ribosome structures II-B and II-C, accounting for the total displacement of ~ 12 Å relative to structures I-A and I-B (Figure 3.5B)^{94, 166}. The incompatibility of the 50S•HflXr complex with the 30S subunit illustrates how HflXr with GDPCP interferes with ribosomal subunit re-association (Figure 3.5B)⁹⁴.

The helix-loop-helix domain (NTD-II) of HflXr occupies essentially the same location in the pre-splitting 70S•HflXr (II-B, II-C, and II-D) and post-splitting 50S•HflXr (III) complexes, acting as the pivot point for the rotation of HflXr (Figure 3.5C, D). The apical loop region of the NTD-II reaches into the PTC of the 50S subunit and interacts with several conserved nucleotides of the 23S rRNA¹⁶⁶. The PTC-binding loop of HflXr is extended by two residues relative to the housekeeping HflX and is not compatible with the binding of lincosamide antibiotics (Figure 3.5D; Appendix B Figure 3.14), explaining the increased resistance phenotype of *L. monocytogenes* to lincomycin by HflXr^{110, 166}. The PTC-loop is also not compatible with the location of the CCA-end of tRNA bound in the canonical p/P state (Figure 3.5E). Therefore, the association of HflXr with the ribosome requires the P-site tRNA to move to a hybrid state of binding, explaining why the mitochondrial homolog, GTPBP6, and *E. coli* HflX, promote rapid recycling of post-release or vacant ribosome complexes, and not of ribosomes bearing a peptidyl-tRNA^{94, 174}.

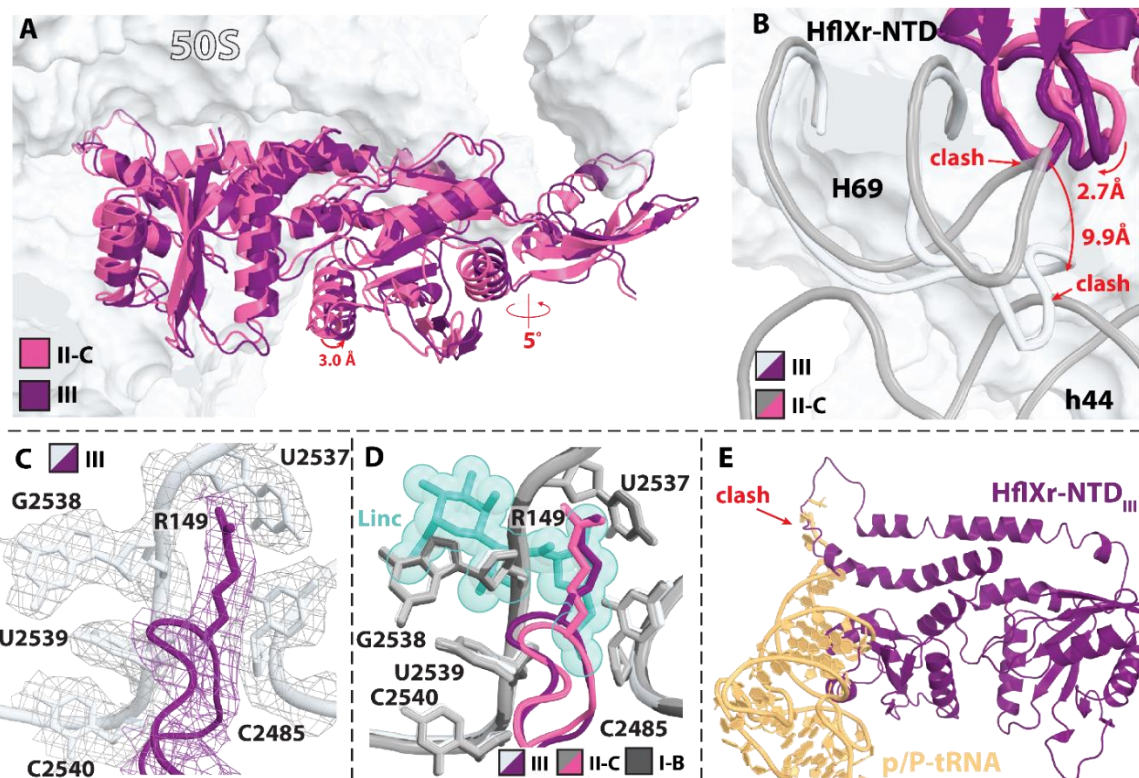


Figure 3.5 HflXr alters the conformation of H69 post-splitting whereas the NTD-II acts as a sensor of the PTC occupancy. (A) Rotation of HflXr in the 50S subunit (III; purple) by $\sim 5^\circ$ relative to its position in the 70S ribosome (II-C; pink), resulting in a displacement of the NTD, G domain and CTD of ~ 3 Å. (B) Displacement of the HflXr NTD toward H69 and dissociation of the 30S subunit result in the continued movement of H69 away from the 50S subunit. (C) Residue Arg149 of the HflXr NTD-II stacks with conserved 23S rRNA nucleotides in the PTC. (D) The NTD-II and Arg149 remain anchored in the PTC in both the 70S ribosome II-C (pink) and 50S subunit III (purple) while not altering the conformation of the PTC. The tip of the PTC-binding loop of HflXr is not compatible with the lincosamide antibiotic lincomycin (turquoise, PDB 8A5I) ¹⁶⁶. (E) NTD-I and NTD-II of HflXr are not compatible with a tRNA bound in the classic p/P state.

3.4 Discussion

The mechanism of ribosome recycling by the enigmatic and conserved GTPase HflX has remained elusive. The available structures of HflX complexed with the 50S ribosomal subunit provided a snapshot of the post-recycling state ^{94, 165-167}, showing that HflX displaces H69 toward the 30S subunit that would cause

a steric clash with h44 in the 30S subunit ^{94, 166, 167}. This observation led to the suggestion that HflX directly breaks the central RNA inter-subunit bridge B2a, thereby dissociating the ribosome into individual subunits. Using time-resolved cryo-EM, we visualized HflXr bound to the 70S ribosome in pre-splitting states. The structures show that HflXr keeps bridge B2a intact, displacing it as a whole toward the 30S subunit. The conformational changes propagate to the platform domain of the 30S subunit, breaking several inter-subunit bridges. In contrast, during canonical ribosome recycling mediated by the concerted action of RRF and EF-G, RRF acts as a wedge breaking bridge B2a by dissolving the interactions between helices H69 and h44 ^{1, 31-33, 43, 44, 53, 61, 63, 76}. Thus, HflXr uses a distinct mechanism to catalyze dissociation of the ribosome into subunits. The residues in the NTD-I of HflXr interacting with helices H69 and H71 are highly conserved in the ubiquitous housekeeping HflX (Appendix B Figure 3.14), suggesting that the ribosome recycling mechanism described here is universal in bacteria.

Upon peptidyl-tRNA hydrolysis, the 30S subunit of the ribosome spontaneously samples both the non-rotated and rotated states ⁵⁶, which is a thermally induced motion ^{50, 185}. Translation factors, such as initiation factor IF2, EF-G, and release factor RF3 are known to stabilize the rotated state of the ribosome ^{3, 9-11, 21, 29, 30, 186-192}. During tRNA translocation, EF-G engages with the A site of spontaneously achieved ribosome conformations such as the rotated state, unlocking the unidirectional movement of peptidyl-tRNA ¹⁹³. Then, the thermally driven reverse rotation of the 30S subunit translocates the peptidyl-tRNA and mRNA ¹⁹⁴. EF-G is proposed to act as a doorstop promoting forward movement of

the peptidyl-tRNA by rectifying the inherent and spontaneous dynamics of the ribosome into translocation of tRNAs and mRNA^{12, 13}. Similarly, following peptide release, EF-G associates with the rotated ribosome bound to RRF, which then catalyzes GTP-dependent subunit dissociation⁵⁵.

In bacteria, stalled ribosomes are rescued by trans-translation¹⁹⁵⁻¹⁹⁸, ArfA¹⁹⁹⁻²⁰⁶, or ArfB^{64, 207-210}, resulting in ribosome complexes carrying a deacylated-tRNA in the P site. Such ribosomes are substrates for canonical recycling by RRF and EF-G, and are likely to also be recycled by HflXr or the housekeeping HflX. Based on the presented structures, we propose the following model for HflXr-mediated recycling of stalled ribosomes. Following peptidyl-tRNA hydrolysis, the spontaneous rotation of the ribosome moves the deacylated-tRNA to a hybrid state of binding. The accessible pocket between helices H69 and H71 in the rotated ribosome allows binding of HflXr and docking of the NTD-I proximal to H69, a state of the ribosome that is seemingly stable (Figures 3.3C, F, 3.6A, B). Upon reverse rotation of the 30S subunit, H69 is sterically blocked by the NTD-I of HflXr from moving back to its canonical position akin to the non-rotated complexes I-A and I-B (Figure 3.6C). As the 30S subunit pivots back around bridge B3, the platform domain shifts away from the 50S subunit to accommodate the non-ideal position of H69, effectively tearing the 70S ribosome into subunits (Figure 3.6D). In this model, the mode of action of HflXr during ribosome recycling is analogous to that of EF-G during tRNA translocation, and possibly during recycling with RRF, in which HflXr passively uses the back rotation of the 30S subunit to split the ribosome into individual subunits. Finally, and by analogy with *E. coli* HflX⁹⁴,

hydrolysis of GTP by HflXr catalyzes its dissociation from the 50S subunit (Figure 3.6E). Whereas our results show that, similar to *E. coli* HflX⁹⁴, GTP hydrolysis by HflXr is not required for ribosome splitting, the use of the non-hydrolysable GTP analog, GTPCP, did not allow to elucidate the role of GTP hydrolysis and Pi release for the dissociation of HflXr from the 50S subunit. It also remains unclear how the ribosome stimulates GTP hydrolysis by HflXr. The G-domain of HflXr does not contact the sarcin-ricin loop (SRL) in the 50S subunit and lacks the landmark catalytic histidine, traits that are essential for the ribosome-stimulated GTP hydrolysis by other translational GTPases.

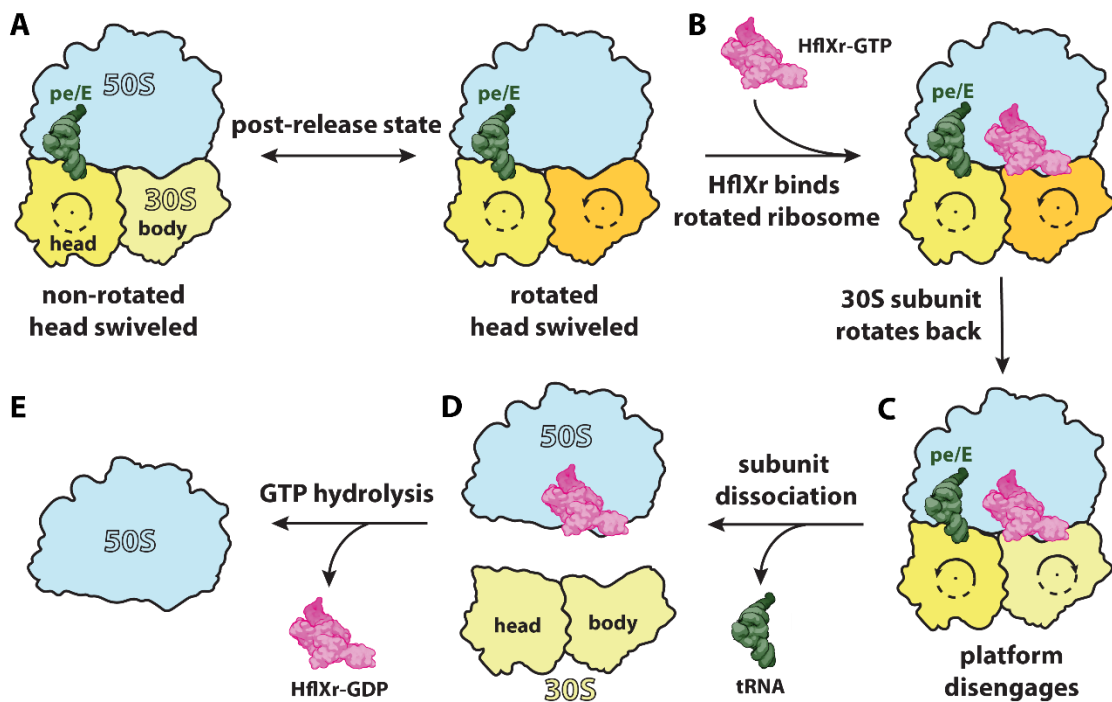


Figure 3.6 Model of HflXr-mediated ribosome recycling. (A) After peptide release, the ribosome spontaneously samples the non-rotated and rotated states. (B) HflXr with GTP binds to the post-release rotated ribosome. (C) Upon back rotation of the 30S subunit, the NTD-I of HflXr impedes helix H69 from returning to its original position, effectively disengaging inter-subunit bridges between the platform domain of the 30S subunit and the 50S subunit. (D) Splitting of the ribosome frees tRNA whereas the dissociated 50S subunit remains bound to HflXr. (E) GTP hydrolysis by HflXr promotes its dissociation from the 50S subunit.

In the HflXr•70S and HflXr•50S complexes, the helix-loop-helix NTD-II of HflXr remains anchored to the PTC of the ribosome, acting as the pivot point for the observed rotation of HflXr (Figure 3.5A). In light of these results, we suggest that the PTC-binding loop of HflXr serves a dual role. On the one hand, the HflXr loop may function as a sensor to discriminate between stalled and actively translating ribosomes and on the other hand, the extended PTC-binding loop in HflXr relative to the housekeeping HflX (Appendix B Figure 3.14) may facilitate clearing of the 50S subunit from PTC-binding antibiotics ^{106, 110, 166}. In *L. monocytogenes*, the expression of the *hflXr* gene is induced by the antibiotics lincomycin and erythromycin ¹¹⁰. It is plausible that HflXr binds and splits post-release ribosomes independently of the presence of a bound drug, as previously proposed ¹⁶⁶. The dissociated antibiotic-free 50S subunits are then available to initiate a new round of translation. It remains unclear, however, whether the 50S subunits would re-bind the antibiotic or if HflXr functions cooperatively with another cellular factor helping to eliminate or neutralize the drug. By responding to the presence of ribosome-targeting antibiotics through the increased production of HflXr, *L. monocytogenes* presumably adapts to a wider range of growth stresses relative to *E. coli*, which possesses only the housekeeping HflX.

In the ribosome complexes reported here, HflXr does not alter the conformation of the PTC nucleotides (Figure 3.5C, D). This observation differs from a previous 50S•HflXr structure in which nucleotide G2538 flips and obstructs the binding sites of lincomycin and erythromycin (Appendix B Figure 3.12D) ¹⁶⁶. The same study showed that the PTC conformation remained unchanged in the 50S

subunit complex bound to the housekeeping *L. monocytogenes* HflX, suggesting that HflXr confers resistance to macrolide and PTC-binding antibiotics through an allosteric mechanism.

The reason for the absence of nucleotide rearrangements in the PTC of our HflXr-bound ribosome complexes is unclear (Figure 3.5C, D; Appendix B Figure 3.12D). One culprit could stem from the use of heterogeneous complexes composed of *L. innocua* ribosomes bound to *L. monocytogenes* HflXr. However, the genome of *L. innocua* also encodes a homolog of HflXr, the sequence of which is 96% identical to that of *L. monocytogenes* HflXr (Appendix B Figure 3.14), with none of the amino acid substitutions located near the PTC or helix H69 in the 50S subunit (Appendix B Table 3.6). The near identical conformation of HflXr (Appendix B Figure 3.12B, C) and the same spatial location of Arg149 at the tip of the PTC-binding loop of HflXr which sterically clashes with bound lincomycin in our and previous complexes (Figure 3.5D; Appendix B Figure 3.12D) ¹⁶⁶, argue in favor of a subtler phenomenon driving the PTC-nucleotide rearrangements. For instance, the shifted position of G2538 previously observed upon HflXr binding to the 50S subunit would also interfere with the binding sites of linezolid and chloramphenicol and yet, HflXr does not confer resistance to these antibiotics ¹⁶⁶. This observation shows that the mechanism of HflXr-mediated antibiotic resistance remains generally obscure. Similarly, the functional relationship between the ribosome recycling activity of HflXr and antibiotic resistance is elusive. It is worth noting that the level of antibiotic resistance provided by *L. monocytogenes* HflXr is relatively modest, with the necessity to knockout VgaL, an ARE-ABCF protein conferring

lincomycin resistance, to observe the effect of HflXr in the presence of this antibiotic ¹¹⁰, re-enforcing the hypothesis that other cellular factors may be involved in clearing the ribosome from bound drugs.

The presence of the ribosome hibernation factor HPF in structure II-B is interesting, showing that HPF does not interfere with the binding of HflXr to the non-rotated ribosome. Despite the relatively mitigated HflXr-induced movement of the platform domain of the 30S subunit bound to HPF (Figure 3.3B, E), structure II-B suggests that HflXr also promotes dissociation of hibernating ribosomes. This agrees with previous reports showing that HflX promotes dissociation of hibernating 100S ribosomes in *Staphylococcus aureus* ^{211, 212}.

In conclusion, our time-resolved cryo-EM reconstructions reveal the long-sought mechanism of ribosome recycling by HflXr and, because of its high sequence and structural homology with the housekeeping gene, by HflX as well. The preservation of the central ribosome bridging region, which is ablated by RRF and EF-G ^{1, 31-33, 43, 44, 53, 61, 63, 76}, underscores the distinct mechanism employed by HflXr in disassembling ribosomes into individual subunits, representing an alternative and universal process that remobilizes stalled bacterial ribosomes.

3.5 Data Availability

The atomic coordinates were deposited in the RCSB Protein Data Bank (PDB) under accession codes 8UU4 (structure I-A; 0 second 70S-HPF), 8UU5 (composite structure I-B; 0 second 70S-head swiveled), 8UU6 (composite structure II-A; 160 seconds 70S-rotated, no HflXr), 8UU7 (composite structure II-

B; 160 seconds 70S-non-rotated-HflXr-HPF), 8UU8 (structure composite II-C; 160 seconds 70S-head swiveled with HflXr), 8UU9 (composite structure II-D; 160 seconds 70S-rotated-head-swiveled bound to HflXr), and 8UUA (structure III; 50S subunit bound to HflXr). The cryo-EM maps have been deposited in the Electron Microscopy Data Bank (EMDB) under accession codes EMD-42554 (structure I-A); EMD-42555 (initial map structure I-B), EMD-42556 (30S head focused map structure I-B), EMD-42557 (composite structure I-B); EMD-42558 (initial map structure II-A), EMD-42559 (30S head focused map structure II-A), EMD-42560 (30S body focused map structure II-A), EMD-42561 (composite structure II-A); EMD-42562 (initial map structure II-B), EMD-42563 (30S head focused map structure II-B), EMD-42564 (30S body focused map structure II-B), EMD-42565 (HflXr focused map structure II-B), EMD-42566 (composite structure II-B); EMD-42567 (initial map structure II-C), EMD-42568 (30S head focused map structure II-C), EMD-42569 (30S body focused map structure II-C), EMD-42570 (HflXr focused map structure II-C), EMD-42571 (composite structure II-C); EMD-42572 (initial map structure II-D), EMD-42573 (30S head focused map structure II-D), EMD-42574 (30S body focused map structure II-D), EMD-42575 (HflXr focused map structure II-D), EMD-42576 (composite structure II-D); and EMD-42577 (structure III).

Chapter 4 Conclusions

4.1 Summary and contributions to the field

Our work reported here provides a deeper understanding of ribosome recycling and its importance in resistance to antibiotics that can be applied to a wide array of pathogenic bacteria. Recycling is an essential final step in translation that bridges the production of one protein to the initiation of a new round of translation. Despite the essential nature of ribosome recycling in bacteria and its distinctness from that in eukaryotic translation, as discussed in Chapter 1, no antibiotics have been designed to inhibit this critical process and there is a lack of mechanistic information in currently available structures of recycling complexes. Additionally, there is a lack of understanding of how alternative recycling through rescue factors described in Chapter 1 contributes to antibiotic resistance and how those mechanisms compare to canonical recycling. Our work has shed light on the molecular basis by which aminoglycosides can inhibit recycling and how alternative ribosome recycling by HflXr is circumventing the effects of a wide range of antibiotics that inhibit translation through a unique stratagem of ribosome splitting.

In Chapter 2 we investigated the mechanism of translation inhibition by the aminoglycoside antibiotic amikacin to elucidate what ribosomal features are essential for ribosome recycling and how those features are affected by amikacin binding. We discovered previously unknown binding sites for amikacin in the ribosome and systematically determined the effects of these sites on ribosome function. Using fast kinetics, we determined that amikacin is the most potent

inhibitor of translation termination and ribosome recycling among known aminoglycosides. A combination of X-ray crystallography and cryo-EM showed that a novel binding site for amikacin in the large ribosomal subunit is likely universally conserved. This site, adjacent to the CCA-end of the P-site tRNA, interacts with universally conserved rRNA nucleotides of the P-loop similar to the binding site of the antibiotics BlaS and BacA^{115, 116}. Despite kinetics results using mutant ribosomes that prevent amikacin binding to the decoding center of the small ribosomal subunit (primary site) that suggest this site is not functionally contributing to translation inhibition, it presents an opportunity to improve upon amikacin binding or the creation of fusion antibiotics that would bind this site and inhibit multiple steps in translation. In the primary amikacin binding site, we showed that the probing nucleotide A1492 is displaced in such a way that is incompatible with the conformation previously reported in recycling complexes with RRF⁶³. This work has contributed to a deeper understanding of aminoglycoside function in general as well and shedding light on the necessity of the interaction between probing nucleotides in the decoding center in the process of ribosome recycling.

In Chapter 3 we investigated ribosome recycling by the rescue factor HflXr due to its slower splitting compared to canonical recycling factors EF-G and RRF^{62, 94, 174}. We hypothesized that HflXr recycled ribosomes using a similar mechanism to that of canonical recycling that involved breaking of the critical central RNA bridge B2a. However, using time-resolved cryo-EM guided by fast kinetics we discovered that HflXr splits ribosomes through a mechanism that is distinct from that mediated by the concerted action of EF-G and RRF. We discovered that the

true substrate of HflXr is likely to be the rotated ribosome, like that of EF-G during translocation, and the binding of HflXr works against natural ribosome rotation to peel the platform subdomain of the 30S subunit away from the 50S subunit^{50, 56, 185}. Back rotation of the ribosome is an essential movement during multiple steps in translation, and the interaction of HflXr with the flexible tip of 23S rRNA helix H69 in the 50S subunit locks H69 in its “rotated” conformation, thus forcing the adjacent platform to accommodate to the non-ideal positioning of H69. Long-range movements in the platform domain disrupt multiple inter-subunit bridges and destabilize the 70S ribosome ultimately leading to dissociation of the subunits. Away from the subunit interface, the helix-loop-helix domain of HflXr occupies the PTC and is sterically incompatible with antibiotics that bind this functional site of the ribosome, suggesting that this sensor-like loop would dislodge the antibiotics and allow the newly liberated 50S subunit to function again in peptide bond formation. The results presented in this work enriches our understanding of how alternative ribosome recycling contributes to antibiotic resistance and has shed light on a novel mechanism of ribosome remobilization by a single factor.

Our work presents new foundations for understanding ribosome recycling, its inhibition by antibiotics and how rescue through recycling contributes to antibiotic resistance. Through structure determination and fast kinetics, we have elucidated more clearly the role of the decoding center nucleotides in ribosome recycling based on conformational changes made by amikacin binding and inhibition. We have systematically determined the role of previously undetected binding sites for amikacin in the ribosome, including a conserved binding site in

the large subunit that could be used to develop new antibiotics that would inhibit tRNA movement that is essential for recycling as well as other steps in translation. By using kinetics to guide freezing of cryo-EM grids, we also determined the first structures of the rescue factor HflXr bound to the ribosome allowing us to elucidate in detail a unique mechanism of ribosome recycling. The ability of HflXr to act passively on the ribosome, working against the thermally driven movement of the 70S ribosome is akin to other translation factors active during the elongation and termination steps. This mechanism presents a new avenue of research into how canonical recycling may act passively interacting with the same area of the ribosome. Taken together, this work has shown the need for continuous investigation of legacy antibiotics as the prevalence of resistance continues to grow as well as the advantages of understanding mechanisms of ribosome rescue and how they can relate to canonical mechanisms of protein synthesis.

4.2 Future directions

As discussed in Chapter 1, approximately 30% of bacteria harbor multiple copies of EF-G in their genome^{78, 79}. Specifically, in *P. aeruginosa*, it has been suggested that one copy of EF-G, EF-G1A, is not translocation competent and is therefore a specialized recycling factor^{82, 83}. However, this was determined using a termination-incompetent *in vitro* translation system, and thus it remains to be seen if EF-G1B can recycle ribosomes in a post-release state. The lack of structural studies of specialized recycling factors like EF-G1A renders us unable to draw conclusions about its specialized nature and about its mechanism of ribosome splitting. Having developed a protocol for time-resolved cryo-EM

described in Chapter 3 will allow us to capture EF-G1A and EF-G1B on the 70S ribosome in the presence and absence of RRF and further elucidate their mechanisms of action. Additionally, point mutations in EF-G1A have been determined to confer significant levels of resistance to amikacin in clinical isolates of *P. aeruginosa*^{213, 214}. In knock-out cell lines, mutant EF-G1A was shown to confer equivalent levels of resistance as the MexXY efflux pump system^{215, 216}. It remains unclear how mutations in EF-G1A confer resistance to amikacin in conjunction with its role in recycling. Having a deeper understanding of amikacin's mechanism of action in recycling inhibition described in Chapter 2 will aid in future structural studies of EF-G1A and its mutants to better understand not only the mechanism of recycling but how resistance is conferred. Continuing this work will provide greater definition of the canonical mechanism of ribosome recycling, the structural basis for specialized recycling and translocation factors, and how bacteria use mutations in these factors to confer resistance to hallmark antibiotics.

As pictured in chapter 1 (Figure 1.5 D), the binding site for GTP in *E. coli* HflX is ~20 Å away from the SRL and in Chapter 3, because of the use of the non-hydrolysable GTP analog, GDPCP, our structures could not shed light on the mechanism of GTP hydrolysis by *L. monocytogenes* HflXr. Our results agree with previous work that GTP hydrolysis is not required for ribosome splitting but is necessary for HflXr dissociation from the 50S subunit. HflX and HflXr lack the hallmark features required for GTP hydrolysis in other translational GTPases such as the catalytic histidine and interaction with the SRL in the 50S subunit. It is known that *E. coli* HflX does not require a guanosine exchange factor, rather only requires

the ribosome to facilitate GTP hydrolysis⁹⁶. Taken together, this suggests that HflXr and the ribosome work in concert to hydrolyze GTP in a way that is unique from other translational GTPases. Further studies to understand how the ribosome stimulate GTP hydrolysis post-splitting are necessary to fully understand the complete mechanism of HflX-mediated ribosome recycling. While the helix-loop-helix domain that binds the PTC in the structures described in Chapter 3 is highly conserved (Appendix B figure 3.24), *M. abscessus* and *M. smegmatis* have additional amino acid residues in this loop that have yet to be studied structurally. This extended loop may take on unique conformations inside the PTC that could account for the broader profile of antibiotic resistance compared to *L. monocytogenes* HflXr^{107, 108}. Using time-resolved cryo-EM methods as described in Chapter 3, we could capture HflX from Mycobacterium on the ribosome and visualize the extended loop inside of the PTC in order to compare its conformations to that of antibiotic binding sites. This work will deepen our understanding of ribosome rescue through recycling and investigate greater nuances of this mechanism in different pathogenic bacteria.

Appendix A. Chapter 2 Supplementary Materials

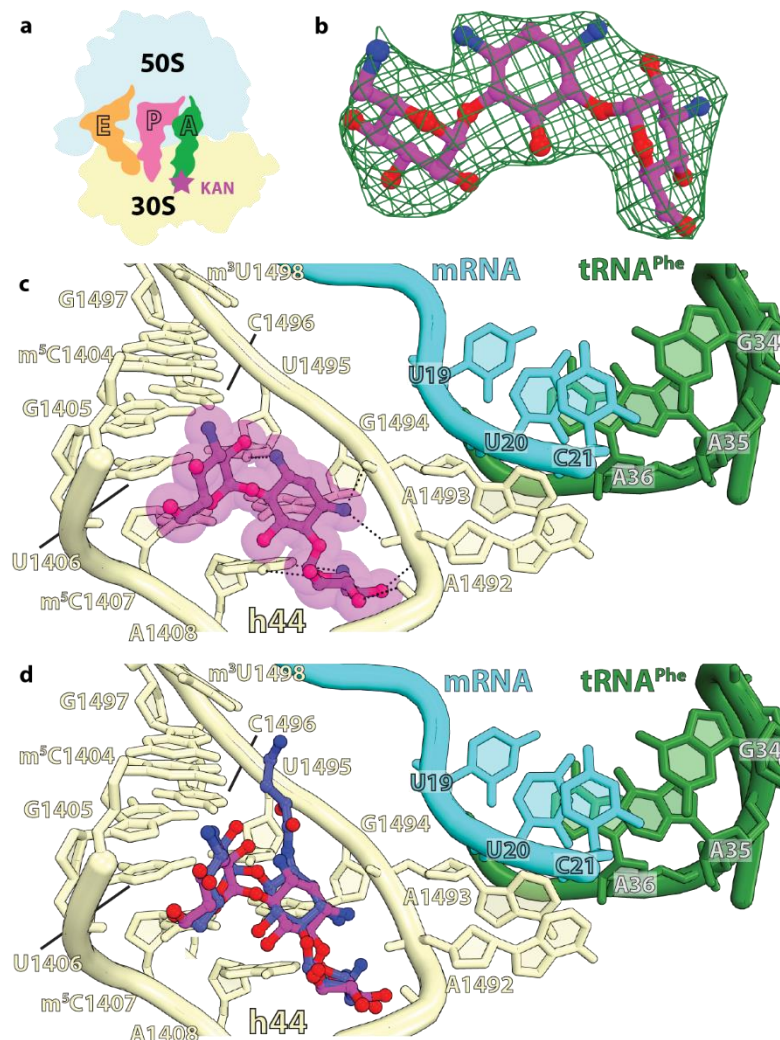


Figure 2.1 Kanamycin binds near the decoding center. **a** Simplified representation of the 70S ribosome with the kanamycin binding site indicated with the magenta star. **b** The unbiased ($F_o - F_c$) difference electron density map of kanamycin bound near the decoding center is contoured at 2.3σ . **c** KAN (magenta) binds within helix h44 (tan) near the decoding center. **d** Superposition of KAN (magenta) and AMK (blue) near the decoding center showing similar positioning of rings I, II and III, and unique interactions formed by the AHB moiety. Reproduced with permission from Seely, S.M. et al. Nature Communications. 2023.¹¹¹

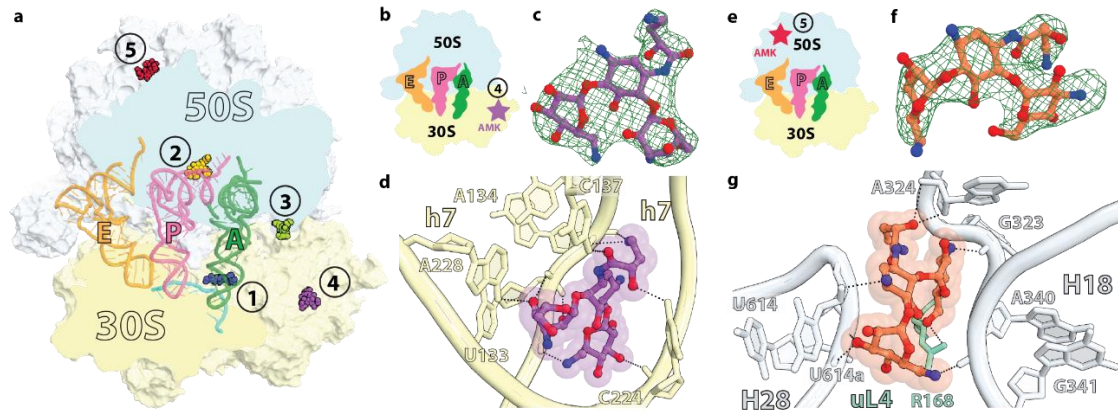


Figure 2.2 Amikacin binds in two additional sites of the *T. thermophilus* 70S ribosome. **a** Overview of the 70S ribosome with AMK bound in five sites. Sites 1 to 3 are described in the main text and figures. Sites 3, 4, and 5 are only observed in the crystal structure, which was obtained using a high-concentration of AMK (see Methods). In the cryo-EM structure of the *E. coli* 70S-AMK complex, only sites 1 and 2 are observed suggesting that AMK binds to sites 3, 4, and 5 with a low-affinity. **b** Simplified representation of the 70S ribosome with the amikacin binding site 4 indicated with the purple star. **c** The unbiased ($F_o - F_c$) difference electron density map of amikacin bound to site 4 is contoured at 2.3σ . **d** AMK #4 (purple) binds to the body domain of the 30S subunit interacting with 16S rRNA helix h7 (yellow). **e** Simplified representation of the 70S ribosome with the amikacin binding site 5 indicated with the orange star. **f** The unbiased ($F_o - F_c$) difference electron density map of amikacin bound to site 5 is contoured at 2.3σ . **g** AMK #5 (orange) binds in domain II of the 23S rRNA (white) interacting with helices H28 and H18 (white), and ribosomal protein uL4 (green). Note that in the *E. coli* ribosome helix H28 is shorter, which ablates this binding site. Reproduced with permission from Seely, S.M. et al. Nature Communications. 2023.¹¹¹

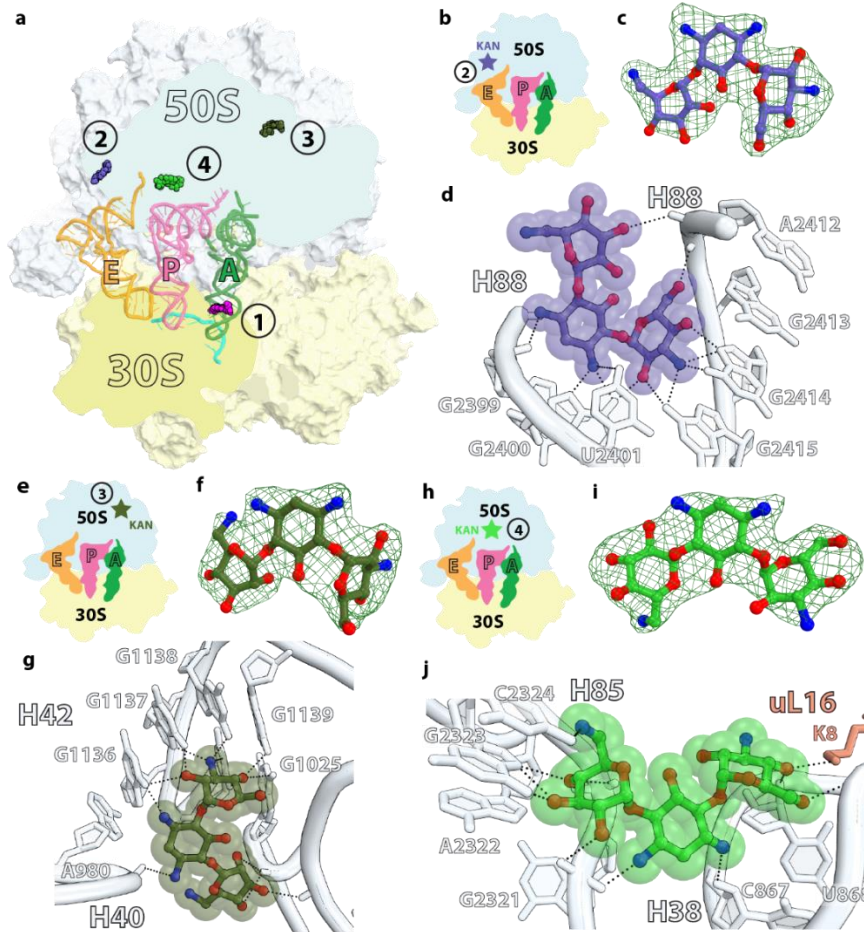


Figure 2.3 Kanamycin binds in three additional sites of the *T. thermophilus* 70S ribosome. **a** Overview of the 70S ribosome with KAN bound in four sites. Site 1 is described in the main text and Supplementary Fig. 1. Sites 2, 3, and 4 represent the three additional sites. **b** Simplified representation of the 70S ribosome with the kanamycin binding site 2 indicated with the purple star. **c** The unbiased ($F_o - F_c$) difference electron density map of kanamycin bound to site 2 is contoured at 2.3σ . **d** KAN at site 2 (purple) binds in domain V of the 23S rRNA (white) and interacts with helix H88. **e** Simplified representation of the 70S ribosome with the kanamycin binding site 3 indicated with the dark green star. **f** The unbiased ($F_o - F_c$) difference electron density map of kanamycin bound to site 3 is contoured at 2.3σ . **g** KAN at site 3 (dark green) binds in domain II of the 23S rRNA (white) and interacts with helices H40 and H42. **h** Simplified representation of the 70S ribosome with the kanamycin binding site 4 indicated with the green star. **i** The unbiased ($F_o - F_c$) difference electron density map of kanamycin bound to site 4 is contoured at 2.3σ . **j** KAN at site 4 (green) binds at the base of the 50S A-site finger helix H38, interacting with the latter, helix H85, and ribosomal protein uL16 (salmon). Reproduced with permission from Seely, S.M. et al. Nature Communications. 2023.¹¹¹

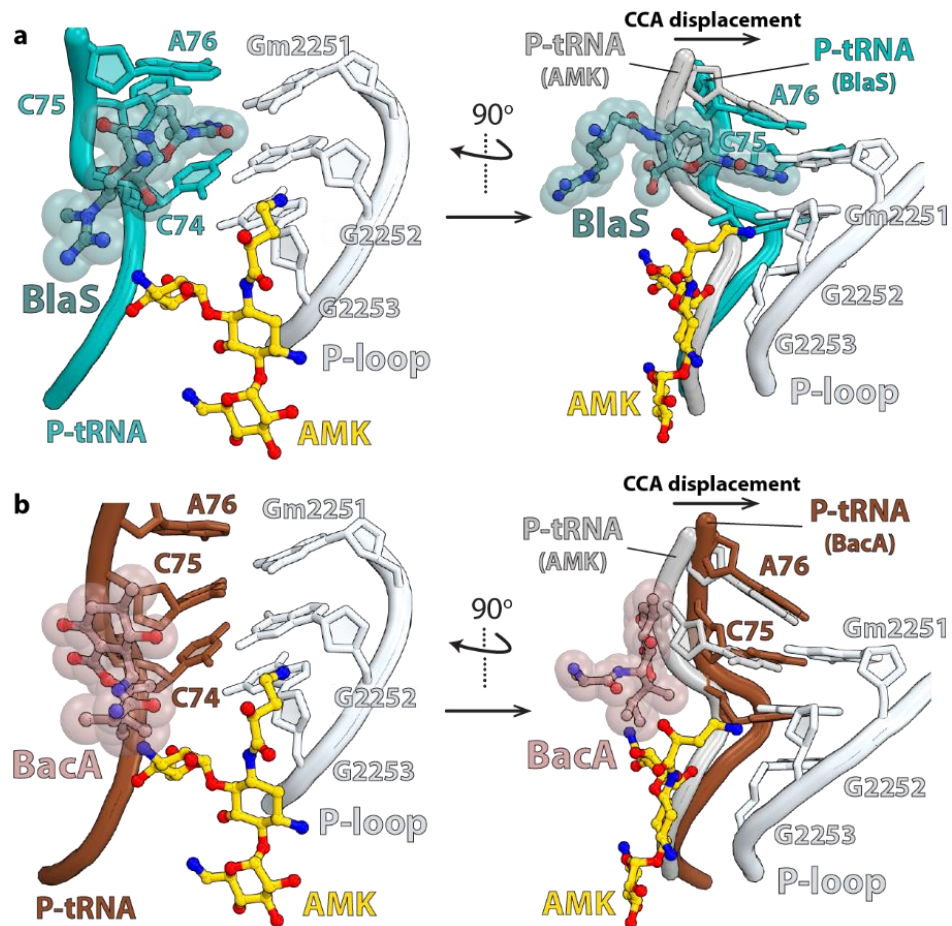


Figure 2.4 Relative binding sites of amikacin, blasticidin S (BlaS), and bactobolin A (BacA) in the large subunit P site. **a** Superposition of the *T. thermophilus* 70S-AMK (this work) and 70S-BlaS (PDB: 4V9Q)¹³⁸ complexes using the 23S rRNA shows the location of BlaS (teal) relative to that of AMK (yellow). The P-site tRNA taken from the 70S-BlaS complex is turquoise. **b** Similar superposition with the 70S-BacA (PDB: 4WT8)¹¹⁹ complex shows the relative binding sites of AMK (yellow) and BacA (tan). The P-site tRNA from the 70S-BacA complex is brown. In the panels to the right, the CCA-end of the P-site tRNA from the *T. thermophilus* 70S-AMK complex (this work) is shown in gray. Reproduced with permission from Seely, S.M. et al. Nature Communications. 2023.¹¹¹

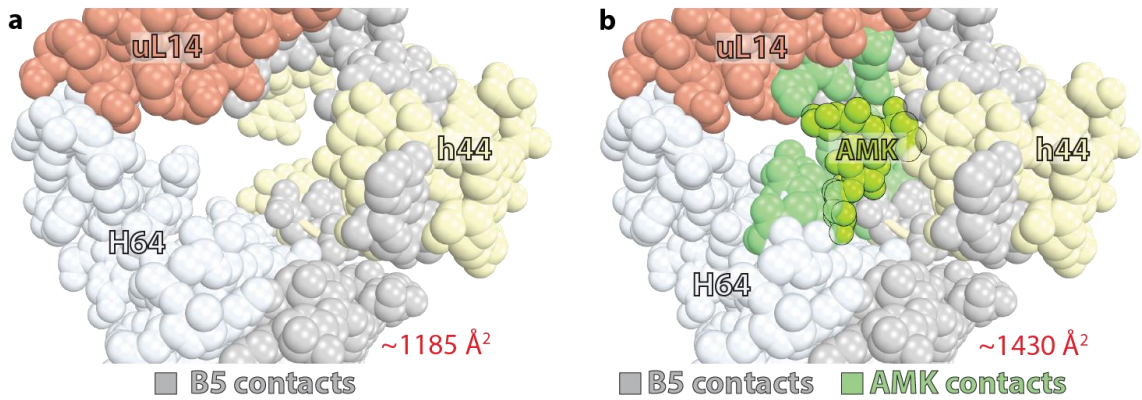


Figure 2.5 Binding of amikacin between the subunits in the *T. thermophilus* ribosome increases the contact area of inter-subunit bridge B5. a Space filling representation of inter-subunit bridge B5 components; 23S helix H64 (white), large subunit protein uL14 (salmon), and 16S helix h44 (tan) with bridge contacts displayed in gray. **b** Same as in panel (a) but with bound amikacin (lime) at bridge B5. Additional contacts between AMK and elements of the ribosome are shown in green. Reproduced with permission from Seely, S.M. et al. Nature Communications. 2023.¹¹¹

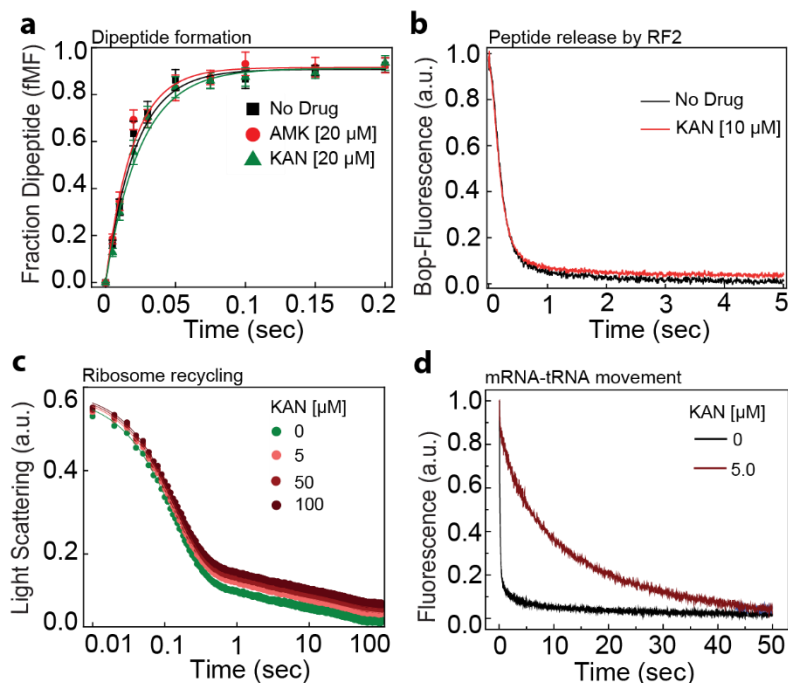


Figure 2.6 Effects of amikacin and kanamycin on the kinetics of dipeptide formation, peptide release, and ribosome recycling. **a** Time courses of $f[{}^3\text{H}]$ Met-Phe dipeptide formation upon rapid mixing of EF-Tu ternary complex (TC) ($5\ \mu\text{M}$) with mRNA-programmed *E. coli* 70S ribosomes ($0.5\ \mu\text{M}$) carrying $f[{}^3\text{H}]$ Met-tRNA^{fMet} in the P site, in the absence (black) and presence of AMK (red) and KAN (green) at indicated concentrations. Solid lines represent the single-exponential fit of the data. Our data show that the rates of dipeptide formation are highly similar in all three conditions. **b** The time courses of BOP-Met-Phe-Leu tripeptide release from pre-termination ribosome complexes (pre-TCs) in the absence (black) and presence of $10\ \mu\text{M}$ KAN (red). The data was fitted to double exponential function and rates were estimated from predominant fast phase, which were alike in both cases. **c** Time traces of Rayleigh light scattering upon splitting of post-termination 70S ribosomes (post-TCs) into subunits by RRF and EF-G in the absence and presence of various amounts of KAN. Traces were fitted with a double exponential function. All experiments were conducted in triplicates and the figures present average data with SEM (where applicable). **d** Time traces of pyrene-mRNA+10 translocation without and with KAN ($5\ \mu\text{M}$). The traces are fitted with single exponential function to obtain the rates. Reproduced with permission from Seely, S.M. et al. Nature Communications. 2023.¹¹¹

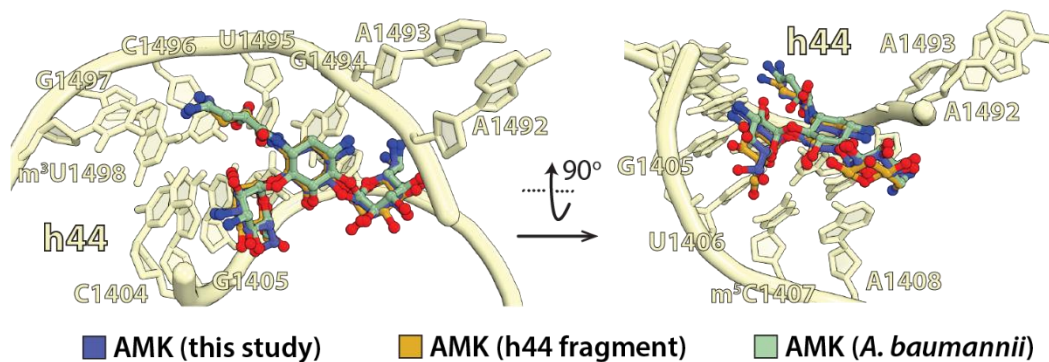


Figure 2.7 Conformation of amikacin near the decoding center. Comparison of the conformation of amikacin bound near the decoding center from the current study (blue) with that obtained using the 16S rRNA helix h44 model fragment (PDB: 4P20; gold)⁹¹ and the *A. baumannii* 70S ribosome lacking tRNAs (PDB: 6YPU; green)⁹³. Reproduced with permission from Seely, S.M. et al. Nature Communications. 2023.¹¹¹

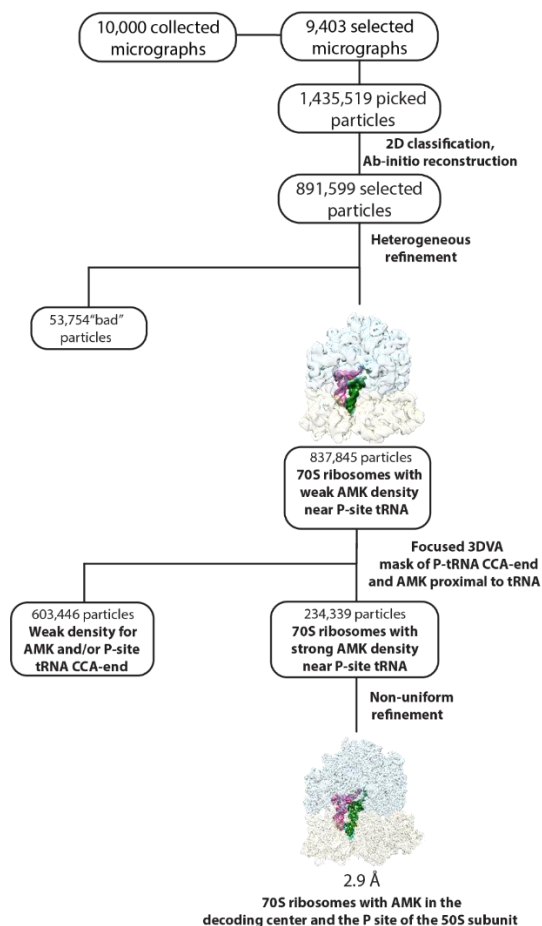


Figure 2.8. Cryo-EM data processing and particle classification workflow. All data processing steps were performed in cryoSPARC 4.1.2¹⁵⁷. 10,000 micrographs were collected, from which 9,403 were selected for further processing. Following two rounds of reference-free 2D classification, the selected particles were used to generate the ab-initio volumes. ‘Heterogeneous refinement’ was performed to sort particles from the ab-initio 3D volumes into two groups, allowing to discard 53,754 particles, resulting in a major class average containing A-, P- and E-site tRNAs (837,845 particles). Variability analysis (3DVA) focused around the CCA-end of the P-site tRNA and the AMK binding site in the 50S subunit proximal the tRNA was utilized to separate particles containing solid density for both the P-site tRNA and AMK near the peptidyl transferase center (234,339 particles). This process discarded 603,446 particles with weak density for AMK and/or the P-site tRNA. Non-uniform and CTF refinement yielded a reconstruction of the *E. coli* 70S ribosome with A-site Phe-tRNA^{Phe}, P-site tRNA^{fMet}, E-site tRNA^{Phe}, and AMK at nominal resolution of 2.9 Å. Reproduced with permission from Seely, S.M. et al. Nature Communications. 2023.¹¹¹

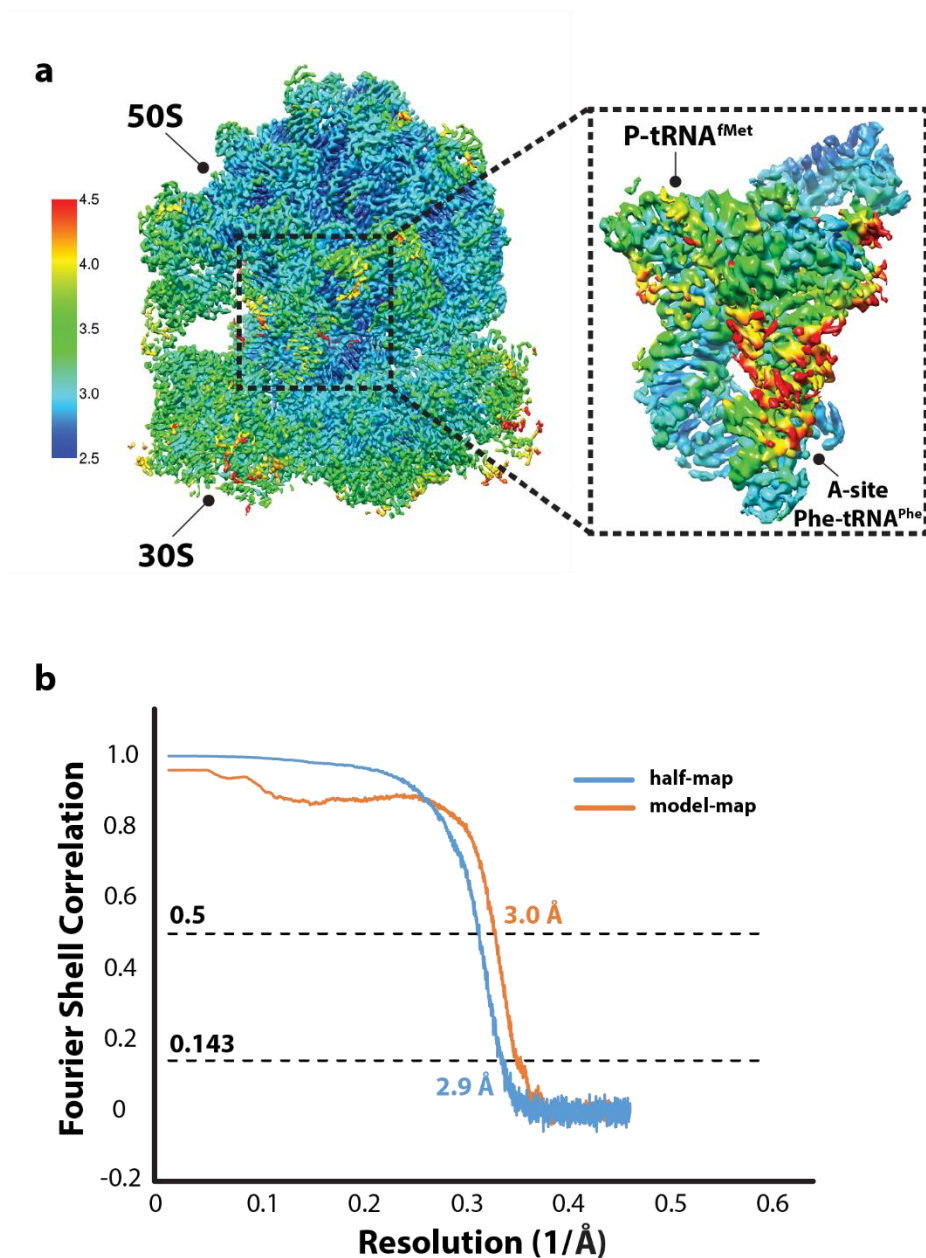


Figure 2.9. Local resolution estimation and Fourier Shell Correlation (FSC) validation. **a** Local resolution heat map of the *E. coli* 70S ribosome with A-site Phe-tRNA^{Phe}, P-site tRNA^{fMet}, E-site tRNA^{Phe}, and AMK shown in the range of 2.5 – 4.5 Å resolution, calculated with cryoSPARC 4.1.2 implementation of BlocRes²¹⁷. **b** Gold-standard Fourier Shell Correlation (FSC) curves of half-maps using a ‘soft mask’ excluding solvent (blue) and model-map are plotted across resolution. Validation of the maps was performed in PHENIX 1.19.2¹⁵⁹. Reproduced with permission from Seely, S.M. et al. Nature Communications. 2023.¹¹¹

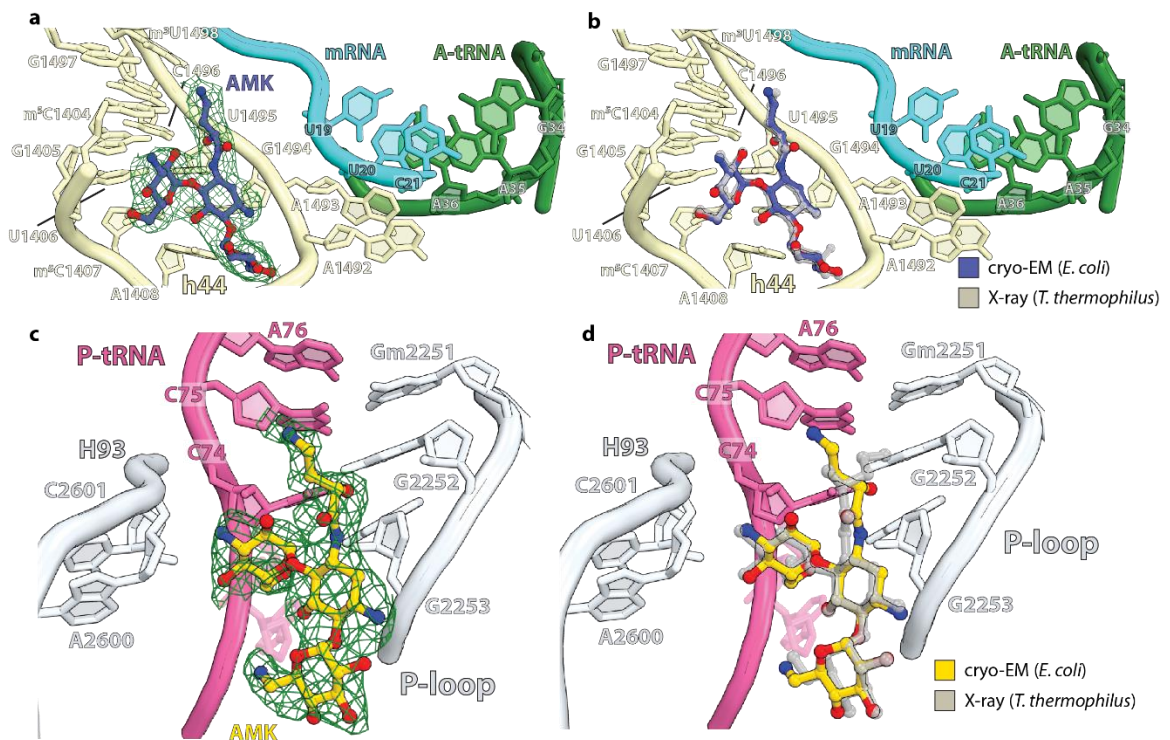


Figure 2.10 Amikacin near the decoding center and in the 50S subunit. **a** Cryo-EM map of amikacin bound to helix h44 near the decoding center in the *E. coli* 70S ribosome. **b** Comparison of the conformation of amikacin bound near the decoding center from the cryo-EM (blue) and crystal (gray) structures. **c** EM map of amikacin bound in the 50S subunit near the CCA-end of the P-site tRNA. **d** Comparison of the conformation of amikacin bound proximal to the peptidyl transferase center in the 50S subunit from the cryo-EM (yellow) and crystal (gray) structures. Reproduced with permission from Seely, S.M. et al. Nature Communications. 2023.¹¹¹

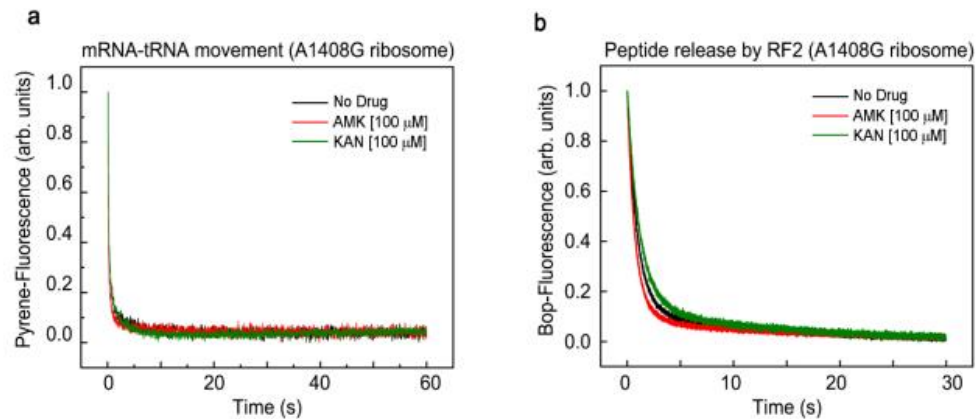


Figure 2.12 Kinetics of mRNA-tRNA translocation and RF2-mediated peptide release on the A1408G ribosomes. **a** Time traces obtained for the EF-G (5 μM) catalyzed movement of pyrene-labeled mRNA on the A1408G ribosomes (0.5 μM) in the absence (black) and presence of 100 μM AMK (red) and 100 μM KAN (green). The traces were fitted with single exponential function to obtain the rates. **b** RF-mediated peptide release from the A1408G ribosomes. The time courses of BOP-Met release from pre-termination ribosome complexes (0.1 μM) upon mixing with RF2 (10 μM) in the absence (black) and presence of 100 μM AMK (red) and 100 μM KAN (green). The data was fitted to double exponential function and rates ($\sim 1.0 \text{ s}^{-1}$) were estimated from predominant fast phase. The results show that the A1408G ribosomes are insensitive to AMK and KAN up to 100 μM in translation translocation and termination. Reproduced with permission from Seely, S.M. et al. Nature Communications. 2023.¹¹¹

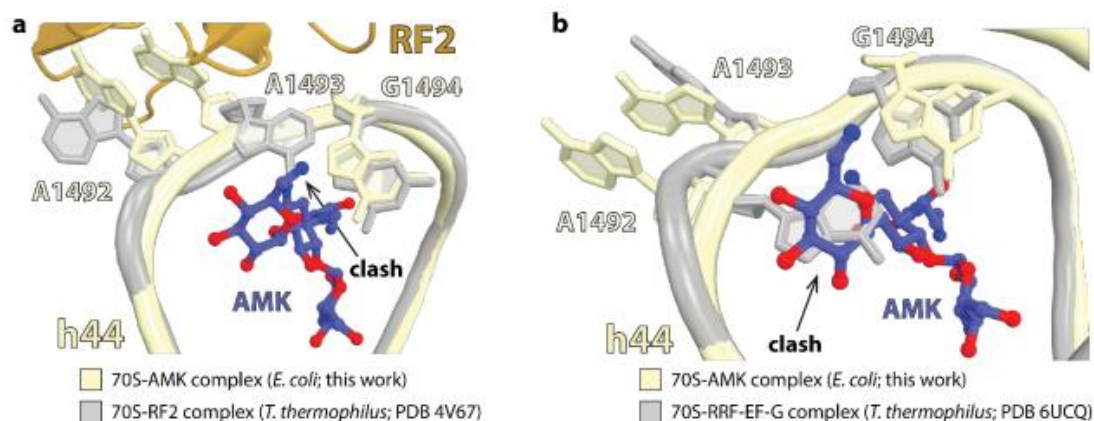


Figure 2.13 Structural basis for the interference of amikacin with RF2-mediated peptide release and ribosome recycling. **a** Amikacin located in h44 near the decoding center is not compatible with the conformation of A1493 upon binding of RF2 to the ribosome (PDB: 4V67)²⁶. **b** Similarly, in the 70S ribosome bound to EF-G and RRF (PDB: 6UCQ)⁶³, A1492 would collide with amikacin. Reproduced with permission from Seely, S.M. et al. Nature Communications. 2023.¹¹¹

Table 2.1 Minimum inhibitory concentrations (MICs) of AMK and KAN for the *E. coli* strain SQ171 harboring wild-type and A1408G mutant ribosomes.

Antibiotic	WT <i>E. coli</i> SQ171 MIC (µg/mL)			A1408G <i>E. coli</i> SQ171 MIC (µg/mL)		
	Exp1	Exp2	Exp3	Exp1	Exp2	Exp3
KAN	8	8	8	>256	256	256
AMK	1	1	1	32	16	16

Reproduced with permission from Seely, S.M. et al. Nature Communications. 2023.¹¹¹

Table 2.2 X-ray data collection, refinement and validation statistics

	<i>T. thermophilus</i> 70S-AMK (PDB 8EV6)	<i>T. thermophilus</i> 70S-KAN (PDB 8EV7)
Data collection		
Space group	$P2_12_12_1$	$P2_12_12_1$
Cell dimensions		
<i>a</i> , <i>b</i> , <i>c</i> (Å)	210.1, 446.8, 620.2	209.4, 447.6, 617.8
α , β , γ (°)	90, 90, 90	90, 90, 90
Resolution (Å)	187.65 – 2.95 (3.12 – 2.95) ^a	187.07 – 2.89 (3.06 – 2.89) ^b
R_{sym} (%)	28.5 (237.8)	26.5 (207.5)
$I/\sigma(I)$	5.59 (0.67)	6.81 (0.80)
$CC_{1/2}$	99.4 (11.3)	99.5 (18.7)
Completeness (%)	99.0 (97.7)	98.7 (94.8)
Redundancy	4.7 (4.7)	4.6 (4.7)
Refinement		
Resolution (Å)	2.95	2.89
No. reflections	1,198,299	1,260,633
$R_{\text{work}} / R_{\text{free}}$	22.3 / 27.2	21.6 / 26.3
No. of non-hydrogen atoms		
Protein	90,976	90,976
RNA	200,224	200,225
Ions (Mg/Zn/Fe)	2,333/12/2	2,259/12/2
Waters	2,328	2,125
Amikacin/Kanamycin	8	7
Average <i>B</i> factors (Å ²)		
Protein	75.9	70.0
RNA	73.3	67.4
Ions	62.4	59.7
Waters	58.0	55.7
MolProbity score	2.86	2.77
Clashscore	10.66	9.46
R.m.s. deviations		
Bond lengths (Å)	0.004	0.004
Bond angles (°)	0.889	0.835
Ramachandran plot		
Favored (%)	89.91	91.24
Allowed (%)	8.71	7.43
Disallowed (%)	1.38	1.33

Diffraction data from single crystals were used to determine the structures. Values in parentheses are for the highest-resolution shell.

^a $I/\sigma(I) = 2$ at 3.34 Å resolution.

^b $I/\sigma(I) = 2$ at 3.20 Å resolution.

Reproduced with permission from Seely, S.M. et al. Nature Communications. 2023.¹¹¹

Table 2.3 Cryo-EM data collection, refinement and validation statistics.

	<i>E. coli</i> 70S-AMK (EMD-40882) (PDB 8SYL)
Data collection and processing	
Magnification	105,000x
Voltage (kV)	300
Electron exposure (e ⁻ /Å ²)	40.6
Defocus range (μm)	-0.7 to -2.0
Detector	Gatan K3
Pixel size (Å)	0.839
Symmetry imposed	C1
Initial particle images (no.)	891,599
Final particle images (no.)	234,339
Map resolution (Å)	2.9
FSC threshold	0.143
Refinement	
Initial model used (PDB code)	8EKC
Model resolution (Å)	3.0
FSC threshold	0.5
Map sharpening <i>B</i> factor (Å ²)	-40
CC _{mask}	0.88
MolProbity score	1.74
Clashscore	8.34
Model composition	
Chains	57
Non-hydrogen atoms	144,592
Protein residues	5,549
RNA residues	4,728
Ions (Mg / Zn)	474 / 2
Waters	74
Amikacin	2
Average <i>B</i> factors (Å ²)	
Protein	68.9
RNA	71.8
Ions	45.7
Waters	40.2
R.m.s. deviations	
Bond lengths (Å)	0.004
Bond angles (°)	0.551
Ramachandran plot	
Favored (%)	95.88
Allowed (%)	3.97
Disallowed (%)	0.15

Reproduced with permission from Seely, S.M. et al. Nature Communications. 2023.¹¹¹

Appendix B Chapter 3 Supplementary Materials

Table 3.1. Data collection, processing and structure refinement statistics.

	Structure I-A (EMD-42554) (PDB 8UU4)	Structure I-B (EMD-42557) (PDB 8UU5)
Data collection and processing		
Magnification	96,000x	96,000x
Voltage (kV)	300	300
Electron exposure (e ⁻ /Å ²)	40	40
Defocus range (μm)	-1 to -2.3	-1 to -2.3
Detector	Falcon III (ThermoFisher)	Falcon III (ThermoFisher)
Pixel size (Å)	0.85	0.85
Symmetry imposed	C1	C1
Initial particle images (no.)	607,118	607,118
Final particle images (no.)	303,270	196,886
Map resolution (Å)	3.0	3.0
FSC threshold	0.143	0.143
Refinement		
Initial model used (PDB code)	7NHN	7NHN
Model resolution (Å)	3.1	3.1
FSC threshold	0.5	0.5
Map sharpening <i>B</i> factor (Å ²)	-85	-90
Model composition		
Chains	50	51
Non-hydrogen atoms	139,761	140,861
Protein residues	5,407	5,298
RNA residues	4,533	4,627
Ligands: Mg ²⁺ /Zn ²⁺	449 / 4	490 / 4
Waters	133	323
<i>B</i> factors (Å ²)		
Protein residues	60.1	36.3
RNA residues	67.0	46.3
Ions	41.9	29.0
Waters	39.1	26.3
CC _{mask}	0.88	0.84
R.m.s. deviations		
Bond lengths (Å)	0.005	0.002
Bond angles (°)	0.614	0.544
Validation		
MolProbity score	1.72	1.91
Clashscore	5.7	6.7
Rotamer outliers (%)	0	0.02
Cβ outliers (%)	0	0
Ramachandran plot		
Favored (%)	93.77	94.98
Allowed (%)	6.14	4.88
Disallowed (%)	0.09	0.13

Table 3.1. Continued.

	Structure II-A (EMD-42561) (PDB 8UU6)	Structure II-B (EMDB-42566) (PDB 8UU7)	Structure II-C (EMD-42571) (PDB 8UU8)	Structure II-D (EMD-42576) (PDB 8UU9)
Data collection and processing				
Magnification	96,000x	96,000x	96,000x	96,000x
Voltage (kV)	300	300	300	300
Electron exposure (e-/Å ²)	40	40	40	40
Defocus range (µm)	-1 to -2.3	-1 to -2.3	-1 to -2.3	-1 to -2.3
Detector	Falcon III (ThermoFisher)	Falcon III (ThermoFisher)	Falcon III (ThermoFisher)	Falcon III (ThermoFisher)
Pixel size (Å)	0.85	0.85	0.85	0.85
Symmetry imposed	C1	C1	C1	C1
Initial particle images (no.)	802,665	802,665	802,665	802,665
Final particle images (no.)	15,497	27,543	55,099	80,381
Map resolution (Å)	3.3	3.2	3.1	3.1
FSC threshold	0.143	0.143	0.143	0.143
Refinement				
Initial model used (PDB code)	7NHN	7NHN	7NHN	7NHN
Model resolution (Å)	3.5	3.3	3.2	3.2
FSC threshold	0.5	0.5	0.5	0.5
Map sharpening <i>B</i> factor (Å ²)	-50	-60	-65	-60
Model composition				
Chains	51	52	54	52
Non-hydrogen atoms	136,923	145,251	142,031	142,177
Protein residues	5,269	5,827	5,929	5,710
RNA residues	4,614	4,613	4,614	4,610
Ligands: Mg ²⁺ /Zn ²⁺	98 / 4	392 / 4	423 / 4	475 / 4
Waters	5	15	364	396
<i>B</i> factors (Å²)				
Protein residues	112.6	84.5	83.4	68.11
RNA residues	130.6	94.9	88.3	79.08
Ions	87.9	63.4	61.5	51.02
Waters	87.6	60.3	57.7	48.65
CC _{mask}	0.84	0.84	0.83	0.85
R.m.s. deviations				
Bond lengths (Å)	0.006	0.003	0.005	0.005
Bond angles (°)	0.654	0.541	0.611	0.615
Validation				
MolProbity score	1.91	1.73	1.87	1.77
Clashscore	8.5	6.5	6.8	5.82
Rotamer outliers (%)	0.06	0	0	0.2
Cβ outliers (%)	0	0	0	0
Ramachandran plot				
Favored (%)	92.83	94.60	91.81	92.99
Allowed (%)	7.11	5.30	8.03	6.84
Disallowed (%)	0.06	0.09	0.15	0.16

Table 3.1. Continued.

	Structure III (EMD-42577) (PDB 8UUA)
Data collection and processing	
Magnification	96,000x
Voltage (kV)	300
Electron exposure (e ⁻ /Å ²)	40
Defocus range (µm)	-1 to -2.3
Detector	Falcon III (ThermoFisher)
Pixel size (Å)	0.85
Symmetry imposed	C1
Initial particle images (no.)	866,478
Final particle images (no.)	332,513
Map resolution (Å)	2.7
FSC threshold	0.143
Refinement	
Initial model used (PDB code)	7NHN
Model resolution (Å)	2.7
FSC threshold	0.5
Map sharpening <i>B</i> factor (Å ²)	-65
Model composition	
Chains	30
Non-hydrogen atoms	91,008
Protein residues	3,406
RNA residues	3,008
Ligands: Mg ²⁺ /Zn ²⁺	200 / 3
Waters	134
<i>B</i> factors (Å ²)	
Protein residues	64.44
RNA residues	63.10
Ions	55.15
Waters	43.49
CC _{mask}	0.88
R.m.s. deviations	
Bond lengths (Å)	0.007
Bond angles (°)	0.716
Validation	
MolProbity score	1.50
Clashscore	4.14
Rotamer outliers (%)	0
Cβ outliers (%)	0
Ramachandran plot	
Favored (%)	95.64
Allowed (%)	4.30
Disallowed (%)	0.06

Reproduced with permission from Seely, S.M. et al. Nucleic Acids Research.

2024.¹⁶¹

Table 3.2. Buried Surface area of inter-subunit bridges of the six 70S ribosome complexes.

Bridge	Structure I-A	Structure I-B	Structure II-A	Structure II-B	Structure II-C	Structure II-D
B1a	0.00	0.00	0.00	0.00	0.00	0.00
B1b	347.48	24.21	0	290.30	0	0
B1c	573.12	779.57	610.67	917.01	20.37	323.42
B2a	1233.73	1161.60	1163.87	1250.25	1229.44	1152.72
B2b	177.64	190.52	25.54	19.99	28.41	43.99
B2c	184.36	199.37	15.05	113.68	78.30	11.16
B3	954.60	936.17	886.20	933.35	921.62	889.07
B4	593.14	606.35	485.30	487.49	397.24	412.99
B5	579.81	581.58	537.44	544.93	563.47	522.26
B6	361.58	369.14	196.30	335.19	122.33	231.94
B7a	330.90	335.69	73.62	252.17	179.09	105.97
B7b	558.39	598.96	695.66	297.52	149.97	616.18
B8	481.58	431.18	627.03	504.15	457.98	603.98
TOTAL*	5455.75	5410.55	4706.01	4738.69	4127.86	4590.25

* Total buried surface area excludes bridges B1a, B1b, and B1c (grayed out) located in the head domain of the 30S subunit.

Reproduced with permission from Seely, S.M. et al. Nature Communications. 2023.¹¹¹

Table 3.3. Hydrogen bonds at each inter-subunit bridge in the 70S ribosome complexes.

Structure I-A			Structure I-B			Structure II-A			Structure II-B			Structure II-C			Structure II-D		
B2a																	
23S	Distance (Å)	16S															
A1945[N1]	2.77	C1414[O2']	A1945[N1]	2.99	C1414[O2']	A1945[N1]	2.43	C1414[O2']	A1945[N1]	3.26	C1414[O2']	A1945[N1]	3.07	C1414[O2']	A1945[N1]	2.84	C1414[O2']
C1947[N4]	2.93	C1416[O2']	A1945[N1]	2.75	C1415[O4']	A1945[N3]	3.70	U1503[O2']	C1947[N4]	3.65	C1416[O2']	A1946[N6]	3.44	C1416[O2']	A1946[N6]	3.88	A1501[OP1]
C1947[N4]	2.92	C1416[O3']	A1946[N1]	3.00	G1502[OP2]	A1946[N6]	3.63	C1416[O2']	C1947[N4]	3.12	C1416[O3']	A1949[N6]	2.88	A1415[O2']	A1946[N1]	3.00	A1501[OP2]
A1949[N6]	3.23	A1415[O2']	A1949[N6]	3.14	A1415[O2']	C1947[N4]	3.77	A1417[OP1]	A1949[N1]	2.89	A1415[O2']	A1949[N1]	3.43	A1415[O3']	C1947[N4]	3.69	C1416[O2']
A1949[N1]	3.76	A1415[O3']	A1949[N1]	3.29	A1415[O3']	C1947[N4]	3.41	C1416[O3']	A1949[N1]	3.53	A1415[O3']	A1949[N1]	2.69	A1415[O2']	C1947[N4]	3.57	C1416[O3']
A1949[N1]	3.37	A1415[O2']	A1949[N1]	3.46	A1415[O2']	A1949[N6]	2.95	A1415[O2']	A1952[N1]	2.41	U1503[O2']	A1952[N1]	2.61	U1503[O2']	A1949[N6]	3.06	A1415[O2']
A1952[N1]	2.73	U1503[O2']	A1952[N1]	2.58	U1503[O2']	A1949[N1]	3.41	A1415[O3']	A1952[N1]	2.52	U1503[O2']	A1949[N1]	2.82	A1415[O2']	A1949[N1]	2.82	A1415[O2']
A1952[N1]	2.73	U1503[O2']	A1952[N1]	2.58	U1503[O2']	A1952[N1]	2.52	U1503[O2']	A1952[N1]	2.52	U1503[O2']	A1952[N1]	2.68	U1503[O2']	A1952[N1]	2.68	U1503[O2']
B3			B3			B3			B3			B3			B3		
23S	Distance (Å)	16S															
G1981[O2']	2.73	A1425[N1]	G1981[O2']	3.00	A1425[N1]	G1981[O2']	2.69	A1425[N1]	G1981[O2']	3.00	A1425[N1]	G1981[O2']	2.84	A1425[N1]	G1981[O2']	2.90	A1425[N1]
chain M	Distance (Å)	16S															
GLY 49[N]	3.60	U1429[OP1]	GLY 49[N]	3.90	U1429[OP1]	GLY 49[N]	3.90	U1429[OP1]	GLY 49[N]	3.33	A1491[N1]	GLY 49[N]	3.83	U1429[OP1]	GLY 49[N]	3.83	U1429[OP1]
B4			B4			B4			B4			B4			B4		
23S	Distance (Å)	uS15															
U 760[OP2]	2.77	ARG 88[NH1]	G 759[OP2]	3.80	ARG 88[NH2]	U 760[OP2]	3.31	ARG 88[NH2]	A 761[N6]	3.18	MET 57[SD]	A 761[N6]	3.21	TYR 53[OH]	A 761[N6]	3.21	TYR 53[OH]
A 761[N6]	2.98	TYR 53[OH]	U 760[OP2]	2.29	ARG 88[NH2]	A 761[N6]	3.50	TYR 53[OH]	A 761[N6]	3.03	TYR 53[OH]	A 761[N1]	3.60	TYR 53[OH]	A 761[N1]	3.00	TYR 53[OH]
A 761[N6]	3.05	MET 57[SD]	A 761[N6]	2.96	TYR 53[OH]	A 761[N6]	3.27	MET 57[SD]	A 761[OP1]	2.40	ARG 64[NH2]	A 761[OP1]	2.89	ARG 64[NH2]	A 761[O4']	3.64	ARG 63[NH2]
A 761[OP1]	2.77	ARG 64[NH2]	A 761[N6]	3.15	MET 57[SD]	A 761[N1]	3.46	TYR 53[OH]	A 761[OP1]	2.40	ARG 64[NH2]	A 761[O2']	3.82	ARG 63[NH2]	A 761[O2']	3.86	ARG 63[NH2]
A 761[OP2]	3.27	ARG 88[NH2]	A 761[O2']	3.78	ARG 63[NH2]	A 761[O4']	3.72	ARG 63[NH2]	A 761[OP1]	2.40	ARG 64[NH2]	A 761[O2']	3.82	ARG 63[NH2]	A 761[O2']	3.86	ARG 63[NH2]
A 762[OP2]	2.92	ARG 88[NH2]	A 761[OP1]	2.33	ARG 64[NH2]	A 762[OP1]	3.83	ARG 88[NH1]	A 762[OP1]	3.83	ARG 88[NH1]	A 762[OP1]	3.82	ARG 63[NH2]	A 762[OP1]	3.08	ARG 88[NH1]
A 762[OP2]	2.92	ARG 88[NH2]	A 761[OP1]	2.33	ARG 64[NH2]	A 762[OP2]	3.61	ARG 88[NH2]	A 762[OP2]	3.61	ARG 88[NH2]	A 762[OP2]	3.61	ARG 88[NH2]	A 762[OP2]	3.61	ARG 88[NH2]
B5			B5			B5			B5			B5			B5		
23S	Distance (Å)	16S															
A1749[N6]	3.36	G1482[O3']	A1749[N6]	3.45	G1482[O3']	A1749[N6]	3.74	G1482[O3']	A1749[N6]	3.74	G1482[O3']	A1749[N6]	3.33	G1482[O3']	A1749[N6]	3.33	G1482[O3']
A1749[N6]	3.70	G1483[OP1]	A1749[N6]	3.41	G1483[OP1]	A1749[N6]	3.74	G1483[OP1]	A1749[N6]	3.74	G1483[OP1]	A1749[N6]	3.27	G1483[OP1]	A1749[N6]	3.27	G1483[OP1]
B6			B6			B6			B6			B6			B6		
bL19	Distance (Å)	16S															
LYS 106[N]	3.70	G1439[OP1]	LYS 106[N2]	3.76	G1472[OP2]	GLU 112[OE2]	3.71	G1449[N1]	LYS 106[N]	3.65	G1439[OP1]	LYS 106[N]	3.65	G1439[OP1]	GLU 112[OE2]	2.50	G1449[N1]
ARG 109[NH1]	2.33	G1472[OP2]	ARG 109[NH1]	3.76	G1472[OP2]	GLU 112[OE2]	3.71	G1449[N1]	ARG 109[NH1]	3.51	G1472[OP2]	ARG 109[NH1]	3.51	G1472[OP2]	GLU 112[OE2]	2.50	G1449[N1]
ARG 109[NH1]	3.71	C1471[OP1]	ILE 113[O]	3.51	G1449[N2]	GLU 112[OE2]	3.71	G1449[N1]	ARG 109[NH1]	3.51	G1472[OP2]	ARG 109[NH1]	3.51	G1472[OP2]	GLU 112[OE2]	2.50	G1449[N1]
ARG 109[NH2]	3.64	G1472[OP2]	ILE 113[O]	3.51	G1449[N2]	GLU 112[OE2]	3.71	G1449[N1]	ARG 109[NH2]	3.42	G1472[OP1]	ARG 109[NH2]	3.42	G1472[OP1]	GLU 112[OE2]	2.50	G1449[N1]
B7a			B7a			B7a			B7a			B7a			B7a		
23S	Distance (Å)	16S															
C1928[O4']	3.58	A 710[N6]	C1928[O4']	3.53	A 710[N6]	G1879[OP1]	3.47	A 710[N6]	G1879[OP1]	3.47	A 710[N6]	G1879[OP1]	3.47	A 710[N6]	G1879[OP1]	3.47	A 710[N6]
C1928[O4']	3.58	A 710[N6]	C1928[O4']	3.53	A 710[N6]	A1880[OP1]	3.88	A 710[N6]	A1880[OP1]	3.88	A 710[N6]	A1880[OP1]	3.88	A 710[N6]	A1880[OP1]	3.88	A 710[N6]
B7b			B7b			B7b			B7b			B7b			B7b		
uL2	Distance (Å)	16S															
ARG 175[NH1]	3.45	G 721[OP1]	ARG 175[NH1]	3.38	G 721[OP1]	ARG 272[NH2]	3.39	A 689[OP1]	ARG 175[NH1]	3.45	G 721[OP1]	ARG 175[NH1]	3.45	G 721[OP1]	ARG 272[NH2]	3.39	A 689[OP1]
ARG 175[NH2]	3.62	A 720[O3']	ARG 175[NH2]	3.61	A 720[O3']	ARG 272[NH2]	3.39	A 689[OP1]	ARG 175[NH2]	3.62	A 720[O3']	ARG 175[NH2]	3.62	A 720[O3']	ARG 272[NH2]	3.39	A 689[OP1]
uL2	Distance (Å)	b56	ARG 175[NH2]	3.74	A 720[O2']	uL2	Distance (Å)	b56	ARG 175[NH2]	3.74	A 720[O2']	uL2	Distance (Å)	b56	ARG 175[NH2]	3.74	A 720[O2']
ASP 123[OD1]	3.74	ARG 79[NH1]	uL2	Distance (Å)	b56	ASP 123[OD1]	3.58	ARG 79[NH2]	ASP 123[OD1]	3.58	ARG 79[NH2]	ASP 123[OD1]	3.58	ARG 79[NH2]	ASP 123[OD1]	3.58	ARG 79[NH2]
ASP 123[OD2]	2.74	ARG 79[NH2]	ASP 123[OD2]	2.44	ARG 79[NH2]	ASP 123[OD2]	3.84	ARG 79[NH2]	ASP 123[OD2]	2.44	ARG 79[NH2]	ASP 123[OD2]	2.44	ARG 79[NH2]	ASP 123[OD2]	2.44	ARG 79[NH2]
ASP 123[OD2]	3.07	ARG 79[NH2]	ASP 123[OD2]	3.84	ARG 79[NH2]	ASP 123[OD2]	3.84	ARG 79[NH2]	ASP 123[OD2]	3.07	ARG 79[NH2]	ASP 123[OD2]	3.07	ARG 79[NH2]	ASP 123[OD2]	3.07	ARG 79[NH2]
B8			B8			B8			B8			B8			B8		
uL14	Distance (Å)	16S															
ASN 13[ND2]	3.78	C 347[OP1]	ASN 13[ND2]	3.58	C 347[OP1]	ASN 13[ND2]	3.63	C 347[OP1]	ARG 17[NH2]	3.23	U1480[OP1]	ASN 13[ND2]	3.82	C 347[OP1]	ASN 13[ND2]	3.05	A 346[OP1]
ARG 97[NH1]	3.29	C 347[OP2]	ARG 97[NH1]	2.46	C 347[OP2]	ASN 13[ND2]	3.40	C 347[OP2]	ARG 97[NH1]	2.56	C 347[OP2]	ARG 97[NH1]	2.56	C 347[OP2]	ASN 13[ND2]	3.03	C 347[OP2]
ARG 97[NH1]	3.09	A 346[OP1]	bL19	Distance (Å)	16S	ARG 17[NH2]	2.17	U1480[OP1]	ARG 97[NH2]	2.88	A 346[OP1]	ARG 97[NH2]	3.79	C 347[OP2]	THR 96[OP1]	2.92	C 347[OP2]
bL19	Distance (Å)	16S	ARG 37[NH1]	2.90	C 353[OP2]	THR 96[OG1]	2.95	C 347[OP2]	ARG 97[NH2]	2.88	A 346[OP1]	ARG 97[NH2]	3.73	A 346[OP1]	ARG 97[NE]	3.18	A 346[OP1]
ARG 37[NH1]	3.65	C 353[OP2]	ARG 37[NH1]	3.59	A 352[O3']	ARG 97[NH2]	3.89	A 346[OP2]	ARG 97[NH2]	2.84	G 354[OP1]	ARG 97[NH2]	3.09	G 354[OP1]	ARG 97[NH2]	3.57	G 345[OP1]
ARG 37[NH2]	3.34	C 353[OP1]	ARG 37[NH2]	3.42	C 353[OP1]	ARG 107[NH2]	2.86	G 354[OP2]	ARG 97[NH2]	2.84	G 354[OP1]	ARG 97[NH2]	3.09	G 354[OP1]	ARG 107[NH1]	2.36	G 354[OP2]
ARG 39[NH1]	2.91	G 354[OP1]	ARG 39[NH1]	3.78	C 353[OP1]	SER 116[OG]	3.82	C 354[O2]	ARG 39[NH1]	2.84	G 354[OP1]	ARG 39[NH1]	3.89	G 354[OP2]	ARG 107[NH1]	2.36	G 354[OP2]
ARG 39[NH1]	2.91	G 354[OP1]	ARG 39[NH2]	2.84	G 354[OP1]	SER 116[OG]	3.82	C 354[O2]	ARG 39[NH1]	2.84	G 354[OP1]	ARG 39[NH1]	3.89	G 354[OP2]	ARG 107[NH1]	2.36	G 354[OP2]

Reproduced with permission from Seely, S.M. et al. Nature Communications. 2023.¹¹¹

Table 3.4. Overall, focused and composite cryo-EM maps generated in this study.

	EMDB ID	PDB ID	Map	No. particles	B-factor sharpening	Resolution ^a
Structure I-A	EMD-42554	8UU4	Overall	303,270	-85	3.0
	EMD-42555	-	Overall		-90	3.0
Structure I-B	EMD-42556	-	Focused (head)		-120	3.0
	EMD-42557	8UU5	Composite	196,886	-	3.0
Structure II-A	EMD-42558	-	Overall		-50	3.3
	EMD-42559	-	Focused (head)		-90	3.6
	EMD-42560	-	Focused (body)		-80	3.5
	EMD-42561	8UU6	Composite	15,497	-	3.3
Structure II-B	EMD-42562	-	Overall		-60	3.2
	EMD-42563	-	Focused (head)		-95	3.3
	EMD-42564	-	Focused (body)		-85	3.3
	EMD-42565	-	Focused (HfIXr)		-120	3.8
	EMD-42566	8UU7	Composite	27,543	-	3.2
Structure II-C	EMD-42567	-	Overall		-65	3.1
	EMD-42568	-	Focused (head)		-120	3.6
	EMD-42569	-	Focused (body)		-100	3.2
	EMD-42570	-	Focused (HfIXr)		-85	3.0
	EMD-42571	8UU8	Composite	55,099	-	3.1
Structure II-D	EMD-42572	-	Overall		-60	3.1
	EMD-42573	-	Focused (head)		-120	3.4
	EMD-42574	-	Focused (body)		-100	3.1
	EMD-42575	-	Focused (HfIXr)		-90	3.0
	EMD-42576	8UU9	Composite	80,381	-	3.1
Structure III	EMD-42577	8UUA	Overall	332,513	-65	2.7

^a Resolution based on the 0.143 threshold in the Fourier Shell Correlation (FSC) curve between two independent reconstructions (see Figures S3, S6, S7, and S10).

Reproduced with permission from Seely, S.M. et al. Nature Communications.

2023.¹¹¹

Table 3.5. Correspondence between rRNA nucleotide numbers in *Listeria innocua* and *Escherichia coli*.

<i>Listeria innocua</i>	<i>Escherichia coli</i>
23S rRNA	
G759	G713
U760	U714
A761	A715
G1864	G1831
C1865	C1832
C1866	C1833
G1868	m ² G1835
C1869	C1836
C1870	C1837
A1881	A1848
G1939	G1906
G1940	G1907
C1941	C1908
C1942	C1909
G1943	G1910
A1945	A1912
A1946	A1913
U1948	m ³ ψ1915
A1949	A1916
U1950	ψ1917
A1951	A1918
A1952	A1919
C2485	C2452
U2537	ψ2504
G2538	G2505
U2539	U2506
C2540	C2507
16S rRNA	
A710	A702
A720	A712
G721	G713
A790	A782
C791	C783
A792	A784
C908	C899
A909	A900
C1414	m ⁵ C1407
A1415	A1408
G1449	G1442
G1472	U1464
A1500	A1492
A1501	A1493
U1503	U1495

Reproduced with permission from Seely, S.M. et al. Nature Communications. 2023.¹¹¹

Table 3.6. Sequence differences between *Listeria innocua* and *Listeria monocytogenes*.

	<i>Listeria innocua</i>	<i>Listeria monocytogenes</i>
Ribosomal RNA		
16S rRNA	A98	U98
	G187	A187
	A188	G188
	G189	A189
	U207	C207
	C208	U208
	C1289	U1289
23S rRNA	G392	A392
	C973	U973
	C1221	U1221
	G1222	A1222
	U1555	C1555
	A2244	U2244
Ribosomal proteins		
uS4	Q79	R79
	T71	K71
uS5	F74	L74
bS6	V88	I88
uS9	P108	S108
	Y116	P116
bS16	M10	I10
uL3	K59	I59
	D73	N73
uL6	N44	K44
	E122	D122
uL13	K137	Q137
uL15	I96	V96
	D113	N113
bL17	H27	F27
uL18	V44	I44
bL19	S19	N19
	G67	S67
uL23	I42	V42
uL24	I50	V50

Reproduced with permission from Seely, S.M. et al. Nature Communications. 2023.¹¹¹

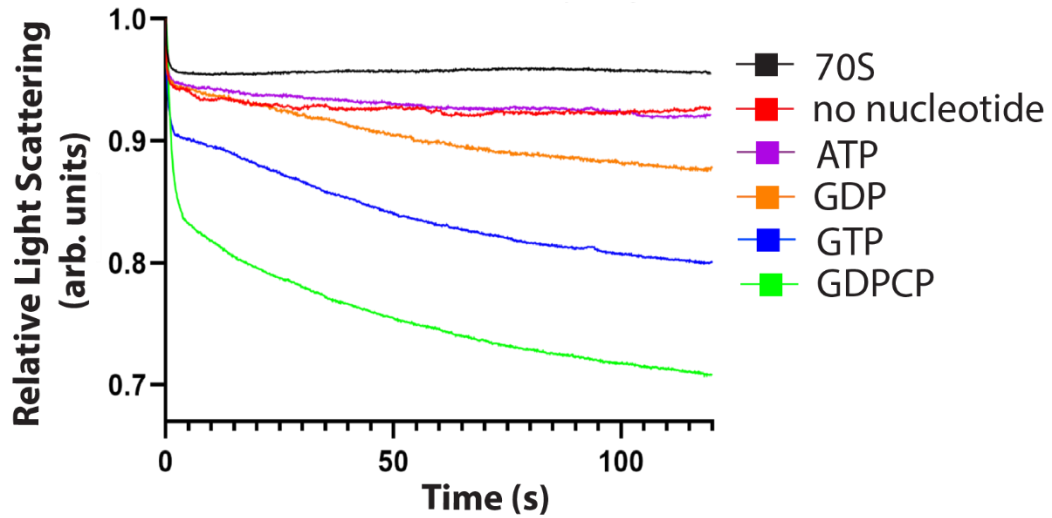


Figure 3.1 HflXr dissociates ribosomes *in vitro* in a nucleotide-dependent manner. Change in light scattering as a response to the dissociation of the 70S ribosome into individual subunits mediated by HflXr. The scattered light intensity at 435 nm after passing through a 400 nm cut-off filter was measured in a stopped-flow apparatus. Ribosomes were rapidly mixed with HflXr in the presence or absence of nucleotides; ATP, GDP, GTP, and GDPCP. Each curve represents the average of 5-8 traces. Reproduced with permission from Seely, S.M. et al. Nature Communications. 2023.¹¹¹

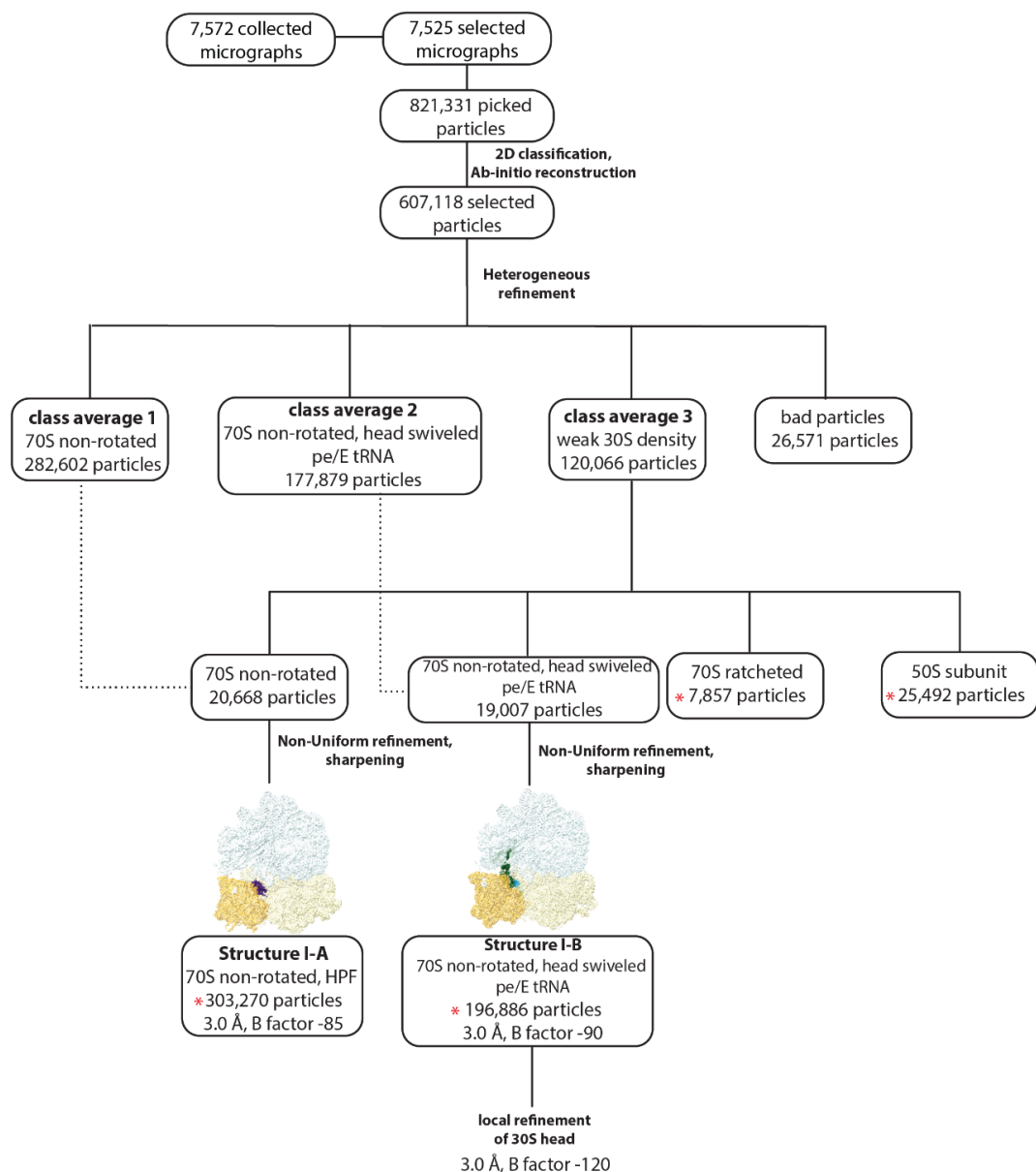


Figure 3.2 Cryo-EM data processing and particle classification workflow (0-second dataset). All processing steps were performed in cryoSPARC 4.1.0¹⁵⁷. The number of micrographs, particles and the volume reconstruction are indicated in boxes with the processing method labeled in each step. Two final ribosome class averages, structures I-A and I-B, were both refined to a nominal resolution of 3.0 Å. The resolution and the sharpening B-factor of the final maps are indicated for each class. See Materials and Methods for details. Red asterisks indicate particles considered to calculate the fraction 70S ribosomes and 50S subunits, reported in Figure 1B. Reproduced with permission from Seely, S.M. et al. Nature Communications. 2023.¹¹¹

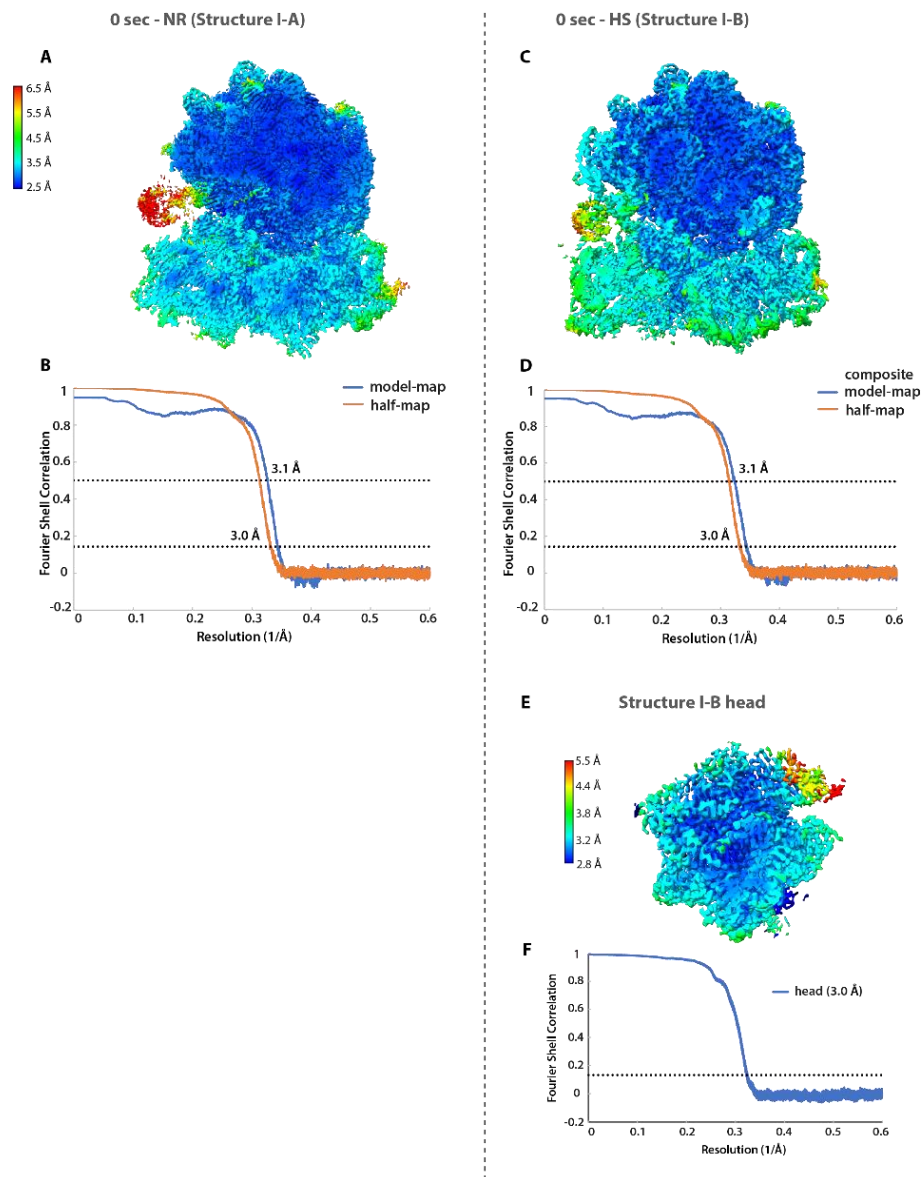


Figure 3.3. Local resolution estimation and Fourier Shell Correction (FSC) validation (0-second dataset). Transverse sections of refined maps of structure I-A (A), structure I-B (C) and the locally refined map of structure I-B head region (E), colored by local resolution as calculated by the cryoSPARC 4.1.0 implementation of BlocRes¹⁵⁷. FSC curves of the masked refinement maps for structure I-A (B) and masked composite map for structure I-B (D) shown in orange, and of the model-to-map correlation curves shown in blue. The FSC curve for the local refinement of the structure I-B head domain (F) is shown in blue. The dashed lines at FSC 0.143 and FSC 0.5 indicate the average resolution for masked maps and the model-to-map correlation, respectively. Reproduced with permission from Seely, S.M. et al. Nature Communications. 2023.¹¹¹

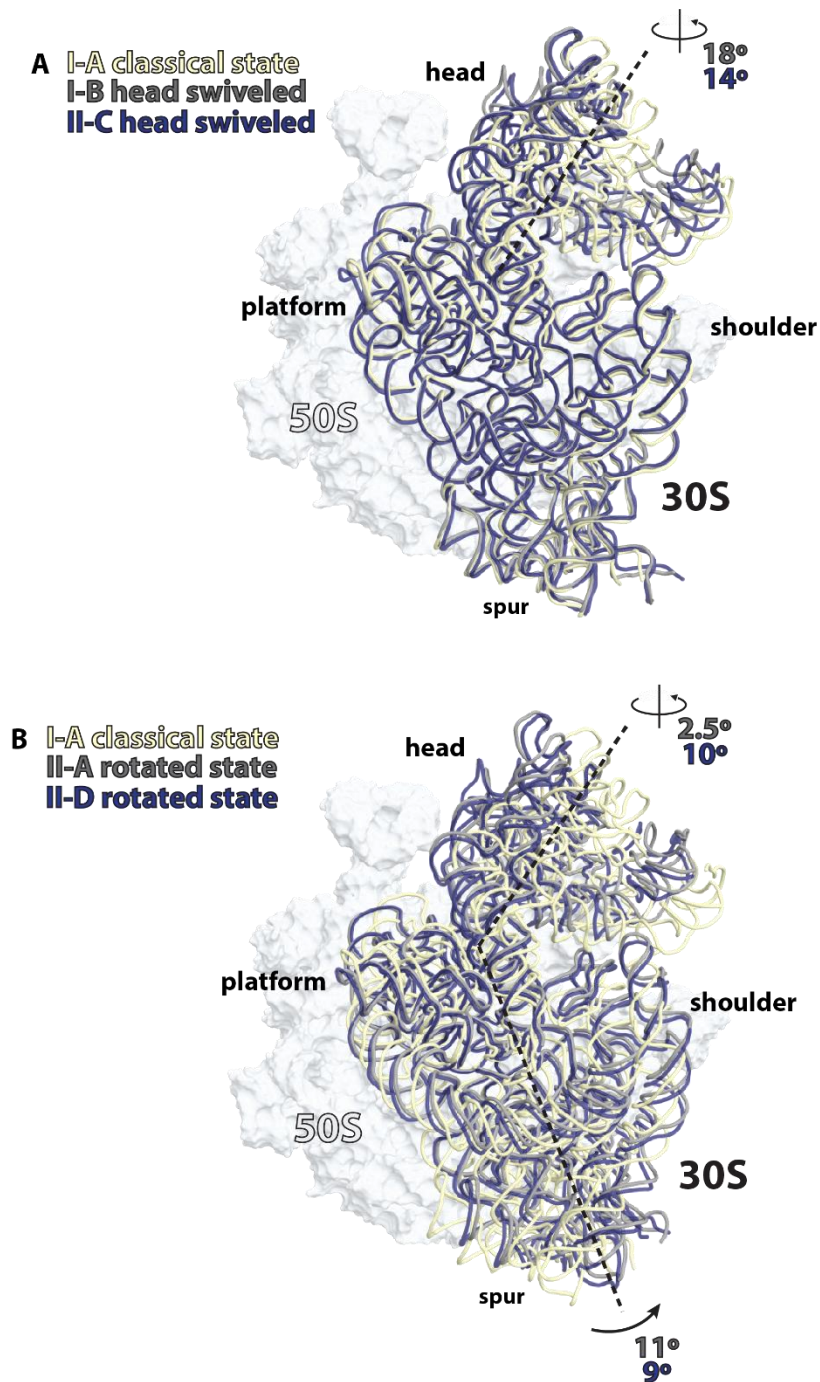


Figure 3.4. Head swiveling and ratchet-like movement of the 30S subunit. (A) Alignment of structures I-B (gray) and II-C (blue) on the classical state ribosome I-A (yellow) by superimposing their 23S rRNA indicates a swiveling motion of the head domain of the 30S subunit. (B) Similar alignment with II-A (gray) and II-D (blue) indicates a counterclockwise ratcheted state of the 30S subunit relative to the 50S subunit (white). The direction of the 30S body rotation is indicated by the curved arrow. Reproduced with permission from Seely, S.M. et al. Nature Communications. 2023.¹¹¹

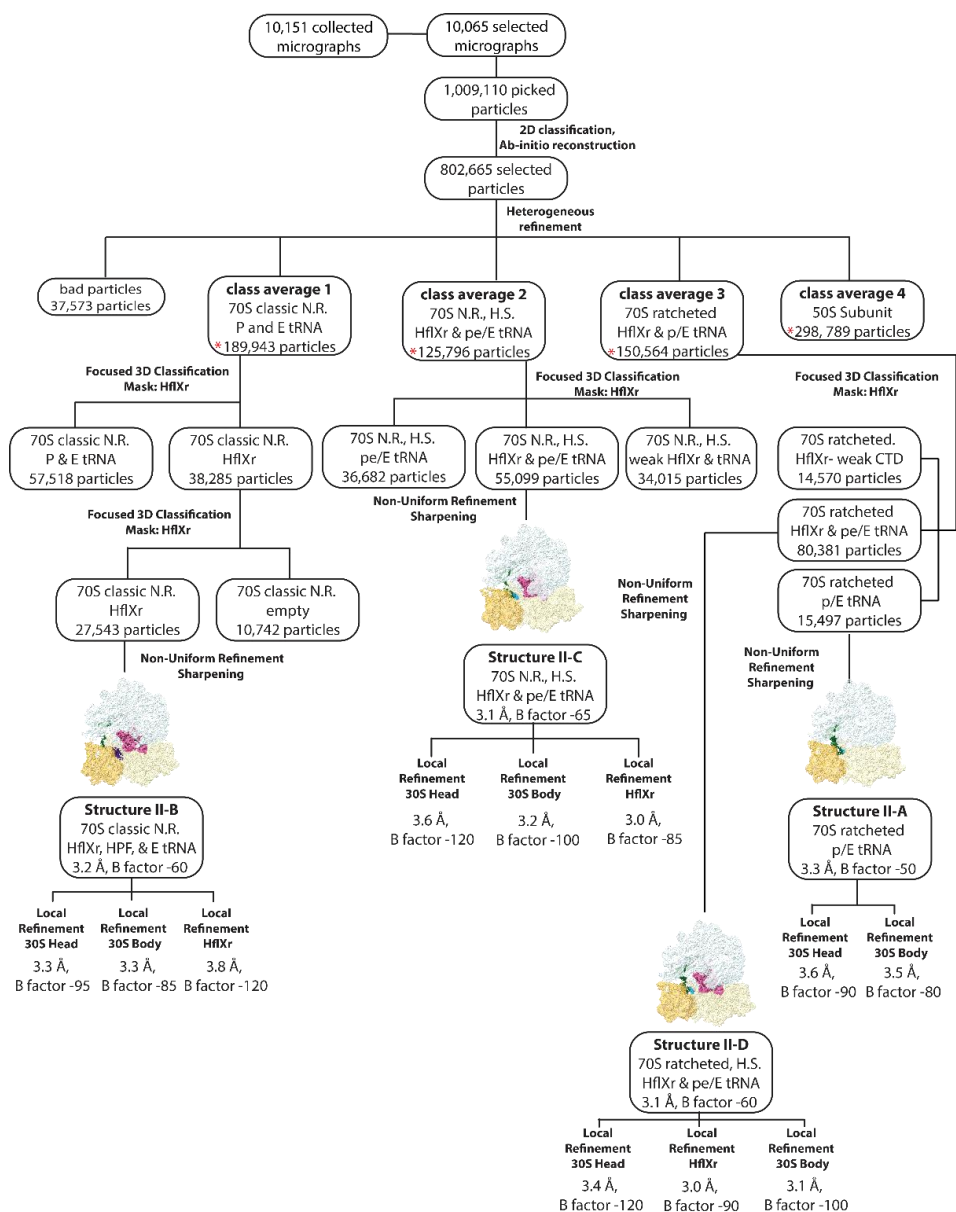


Figure 3.5. Cryo-EM data processing and particle classification workflow (160-second dataset). All processing steps were done in cryoSPARC 4.1.0¹⁵⁷. The number of micrographs, particles and the volume reconstruction are mentioned in boxes with the processing method labeled in each step. The sorting scheme led to four unique ribosome classes structure II-A, structure II-B, structure II-C, and structure II-D, that were refined to 3.3 Å, 3.2 Å, 3.1 Å, and 3.1 Å, respectively. Local refinement focusing on specific regions of these final classes was performed. The resolution and the sharpening B-factor of the final maps are indicated for each class. N.R. = non-rotated; H.S. = head-swiveled. See Materials and Methods for details. Red asterisks indicate particles considered to calculate the fraction 70S ribosomes and 50S subunits, reported in Figure 1B. Reproduced with permission from Seely, S.M. et al. Nature Communications. 2023.¹¹¹

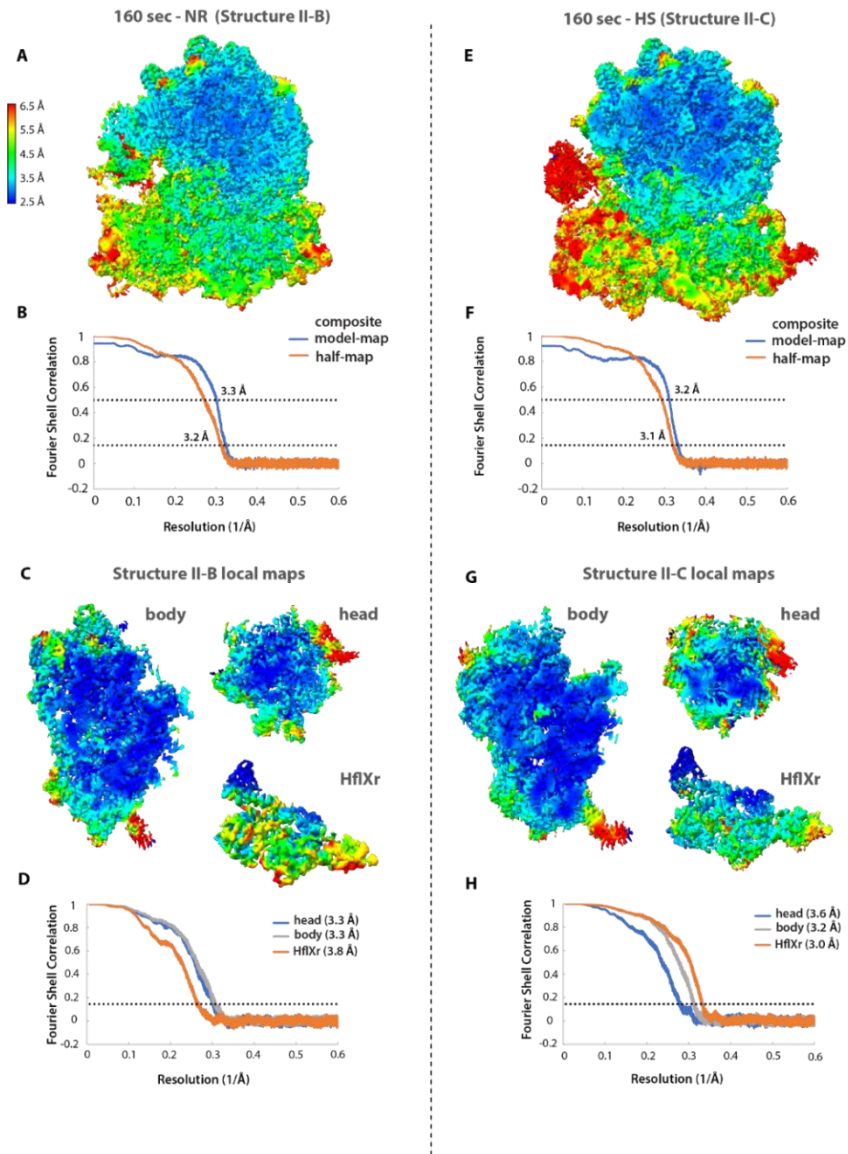


Figure 3.6. Local resolution estimation and Fourier Shell Correction (FSC) validation of structures II-B and II-C (160-second dataset). Transverse section of refined maps of structure II-B (A), structure II-C (E) and the locally refined maps of the 30S body, head, and HflXr in structure II-B (C) and structure II-C (G) are colored by local resolution. FSC curves of the masked composite map of structure II-B (B) and masked composite map for structure II-C (F) are shown in orange, and the model-to-map correlation curves are shown in blue. The FSC curves for the local refinement of structure II-B (D) and structure II-C (H) head (blue), body (gray) and HflXr (orange) are shown with the resolution at FSC 0.143 denoted in brackets. The dashed lines at FSC 0.143 and FSC 0.5 indicate the average resolution for masked maps and the model-to-map correlation resolution, respectively. Reproduced with permission from Seely, S.M. et al. Nature Communications. 2023.¹¹¹

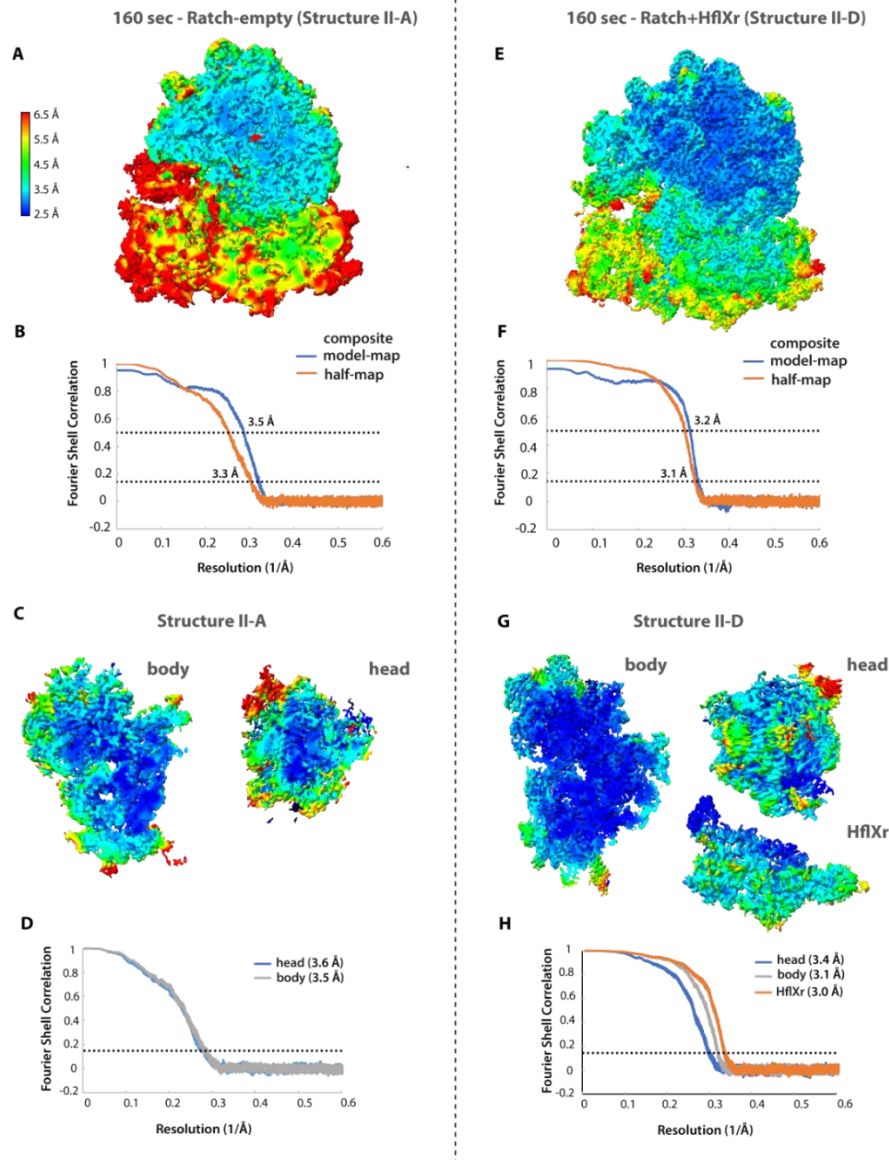


Figure 3.7. Local resolution estimation and Fourier Shell Correction (FSC) validation of structures II-A and II-D (160-second dataset). Transverse section of refined maps of structure II-A (A), structure II-D (E) and the locally refined maps of the 30S body, head or HflXr of structure II-A (C) and structure II-D (G), colored by local resolution. FSC curves of the masked composite map of structure II-A (B) and structure II-C (F) are shown in orange, and the model-to-map correlation curves are shown in blue. The FSC curves for the local refinement of structure II-A (D) and structure II-D (H) head (blue), body (gray), and HflXr (orange) are shown with the resolution at FSC 0.143 denoted in brackets. The dashed lines at FSC 0.143 and FSC 0.5 indicate the average resolution for masked maps and the model-to-map correlation, respectively. Reproduced with permission from Seely, S.M. et al. Nature Communications. 2023.¹¹¹

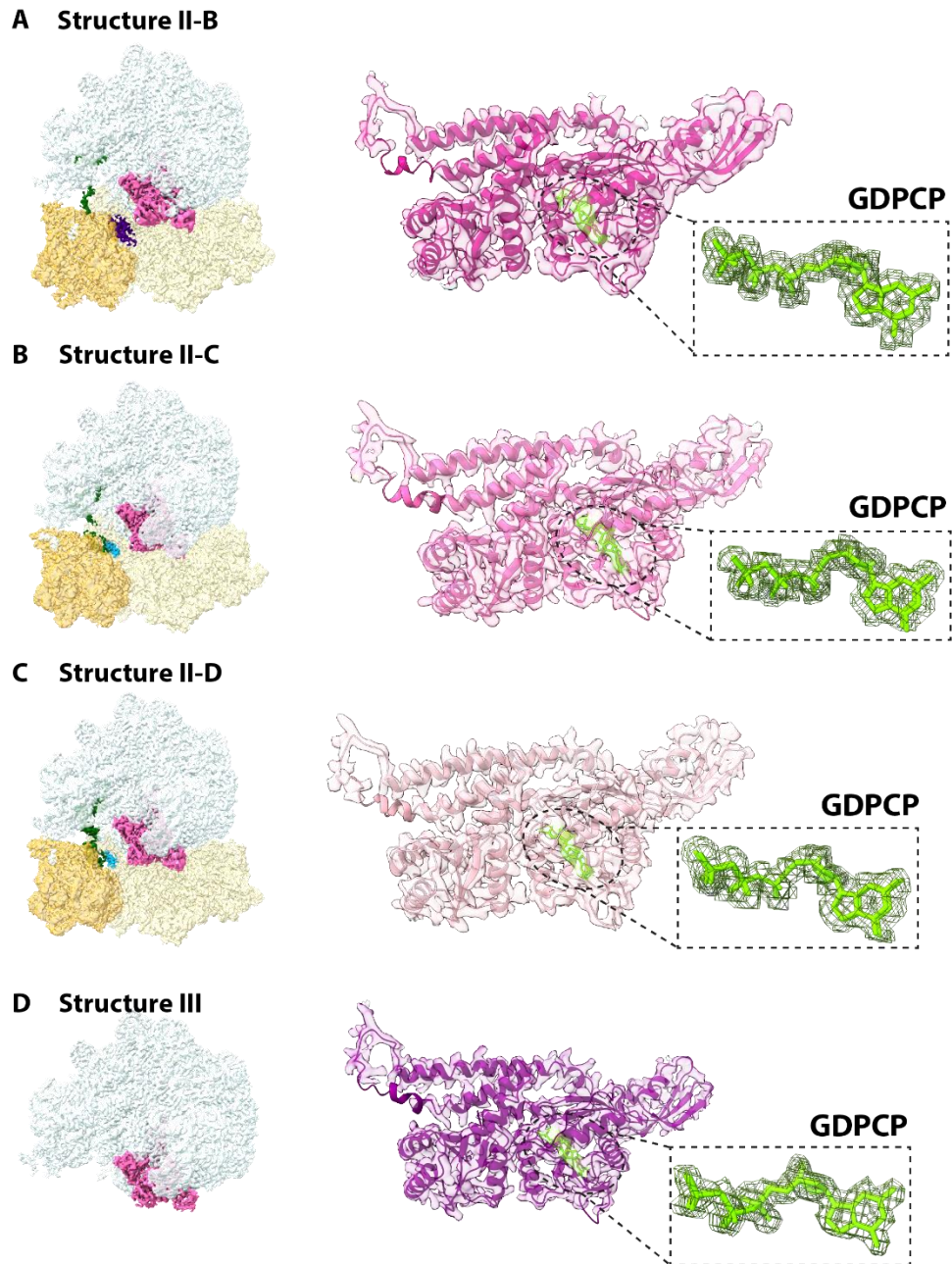


Figure 3.8. Electron density of HflXr on the ribosome in four states. (A-D) (left) Overview of HflXr bound states. (center) Volume representation of cryo-EM maps with a 2 Å radius around HflXr. (inset) EM density of GDPCP bound to the G-domain of HflXr. Reproduced with permission from Seely, S.M. et al. Nature Communications. 2023.¹¹¹

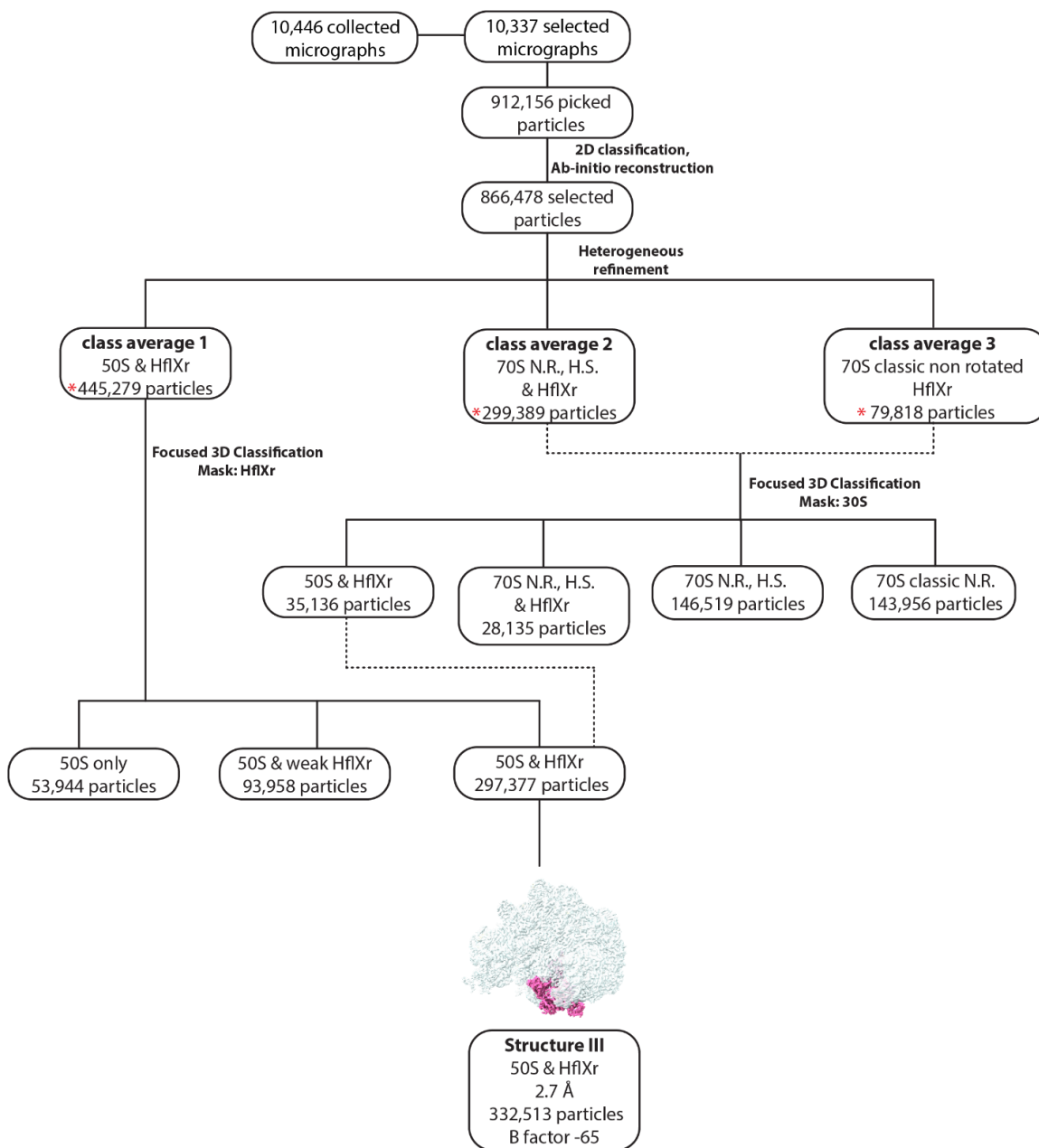


Figure 3.9. Cryo-EM data processing and particle classification workflow (600-second dataset). All processing steps were done in cryoSPARC 4.1.0¹⁵⁷. The number of micrographs, particles and the volume reconstruction are mentioned in boxes with the processing method labeled in each step. The final class of 50S subunits (structure III) contained HflXr, which was refined to a nominal resolution of 2.7 Å. The resolution and the B-factor used for sharpening of the final map are indicated. N.R. = non-rotated; H.S. = head-swiveled. See Materials and Methods for details. Red asterisks indicate particles considered to calculate the fraction 70S ribosomes and 50S subunits, reported in Figure 1B. Reproduced with permission from Seely, S.M. et al. Nature Communications. 2023.¹¹¹

600 sec - (Structure III)

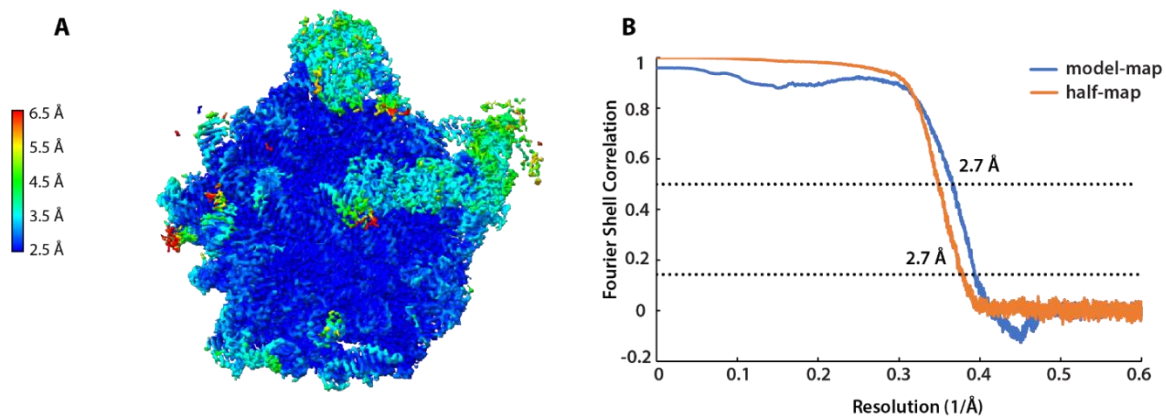


Figure 3.10. Local resolution estimation and Fourier Shell Correction (FSC) validation of structure III (600-second dataset). Transverse section of the final refined map of structure III colored by local resolution. FSC curves of the masked map (orange) and the model-to-map correlation (blue) are plotted. The dashed line at FSC 0.143 and FSC 0.5 indicate the average resolution for masked maps and the model-to-map correlation resolution, respectively. Reproduced with permission from Seely, S.M. et al. Nature Communications. 2023.¹¹¹

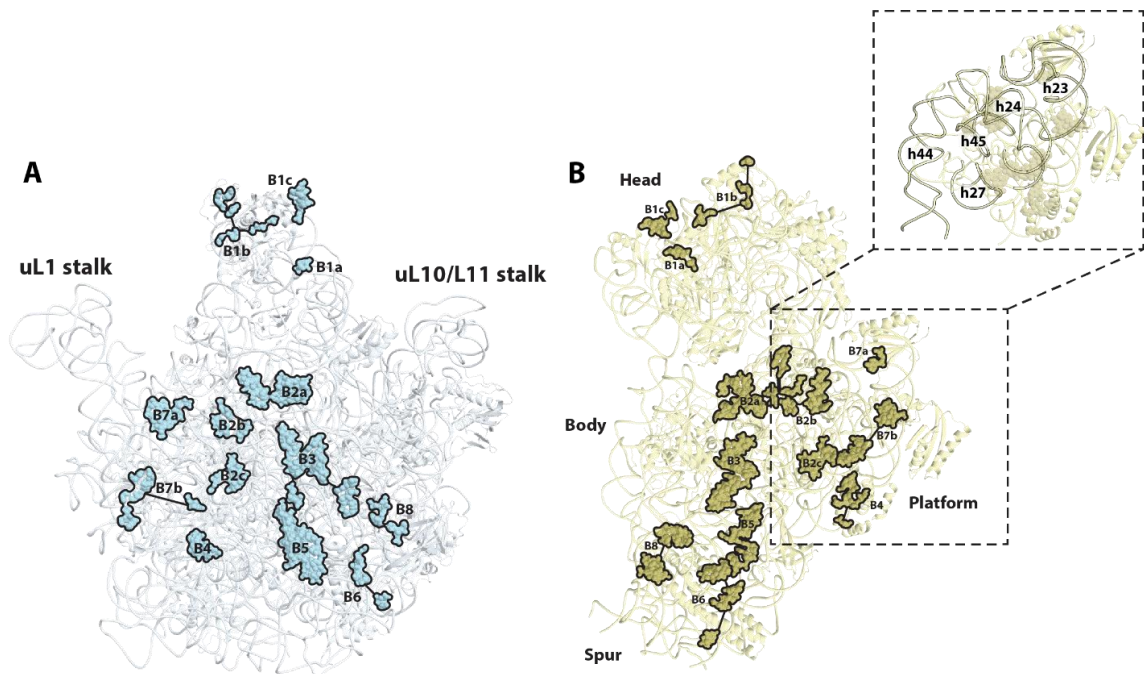


Figure 3.11. Overview of conserved inter-subunit bridges. Bridge components of the 50S (**A**) and 30S (**B**) subunits are shown in spheres from the interface perspective. Helices involved in bridges localized to the platform (inset **B**) are outlined in black. Reproduced with permission from Seely, S.M. et al. Nature Communications. 2023.¹¹¹

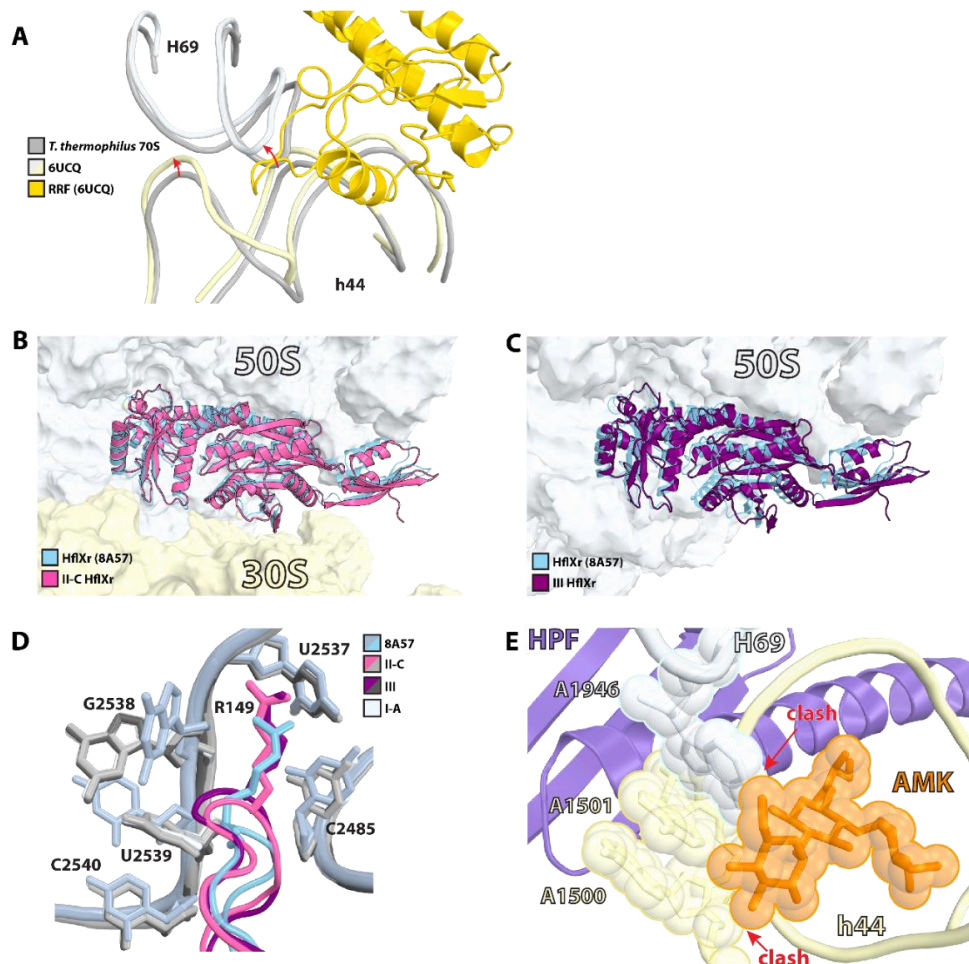


Figure 3.12. Ribosomes complexed with HflXr compared to previous structures. (A) Structure of RRF taken from the EF-G•RRF ribosome complex (yellow, PDB 4UCQ)⁶³ superimposed on the empty *T. thermophilus* ribosome (gray) shows the movement of H69 and h44 near bridge B2a during canonical recycling. (B) Structure II-C (pink) superimposed on PDB 8A57¹⁶⁶ (blue) indicates that HflXr binds in a near identical position on the 70S ribosome to that of the previously published 50S•HflXr complex. (C) Structure III (purple) superimposed on PDB 8A57¹⁶⁶ (blue) with an RMSD value of 1.6 Å, indicating that the 50S•HflXr structures are consistent. (D) Residue Arg149 of the HflXr NTD-II stacks with conserved 23S rRNA nucleotides in the PTC. While Arg149 occupies the same location in our and previous (PDB 8A57)¹⁶⁶, the conformation of G2538 and U2539 in the PTC is unaltered in our structures. (E) Structure I-A superimposed on the *E. coli* 70S ribosome bound with the aminoglycoside amikacin (PDB 8SYL, orange)¹¹¹ indicating clashes with decoding center nucleotides proximal to the binding site of HPF, explaining the increased tolerance of *L. monocytogenes* stationary-phase cultures to aminoglycoside antibiotics¹⁸³. All structures are aligned using 23S rRNA. Reproduced with permission from Seely, S.M. et al. Nature Communications. 2023.¹¹¹

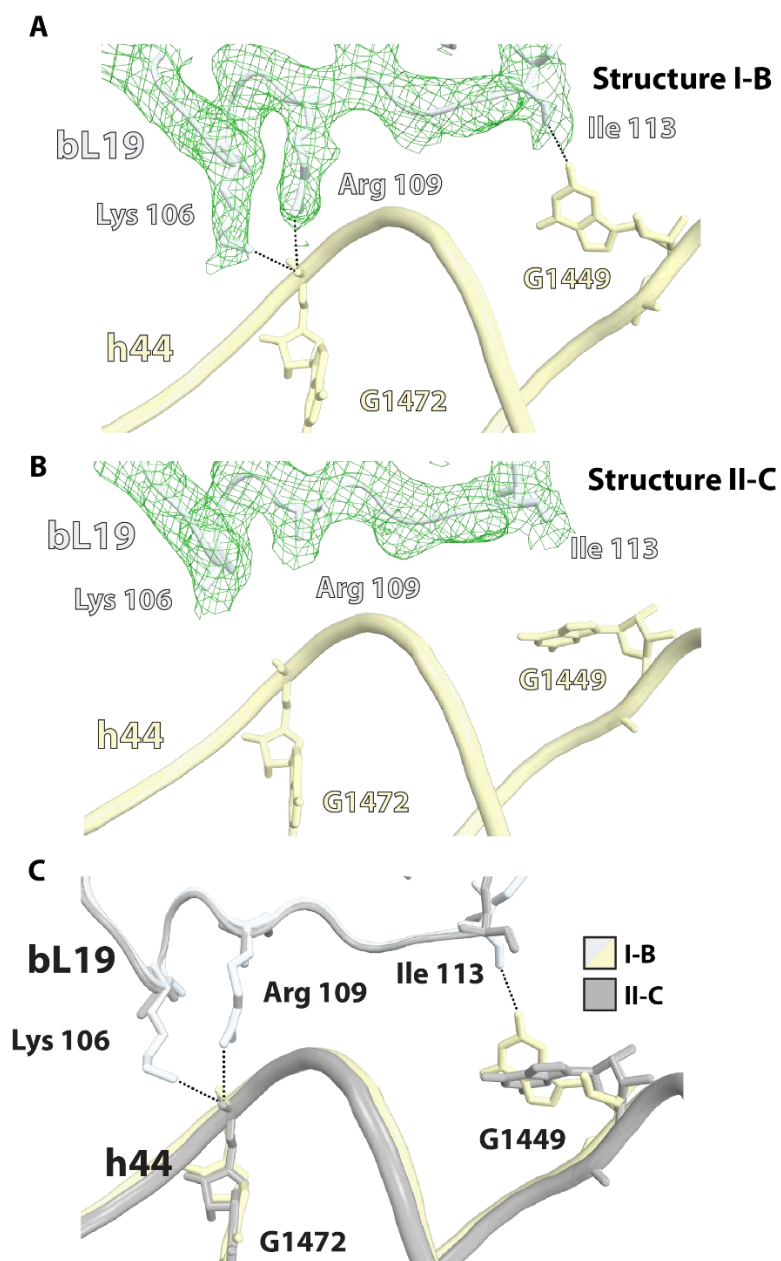


Figure 3.13. HflXr does not disrupt inter-subunit bridge B6 in the 70S ribosome II-C. (A) The EM density of large subunit protein bL19 at 0 second (I-B) is well resolved for side chains that form hydrogen bonds with h44. (B) Unlike I-B at 0 second, side chains of bL19 in structure II-C are not well resolved while the protein backbone could be fit into the EM map. (C) The superimposition of I-B and II-C using 23S rRNA indicates that neither bL19 nor h44 are displaced in the presence of HflXr, suggesting that bridge B6 is not disrupted by the binding of HflXr. Reproduced with permission from Seely, S.M. et al. Nature Communications. 2023.¹¹¹

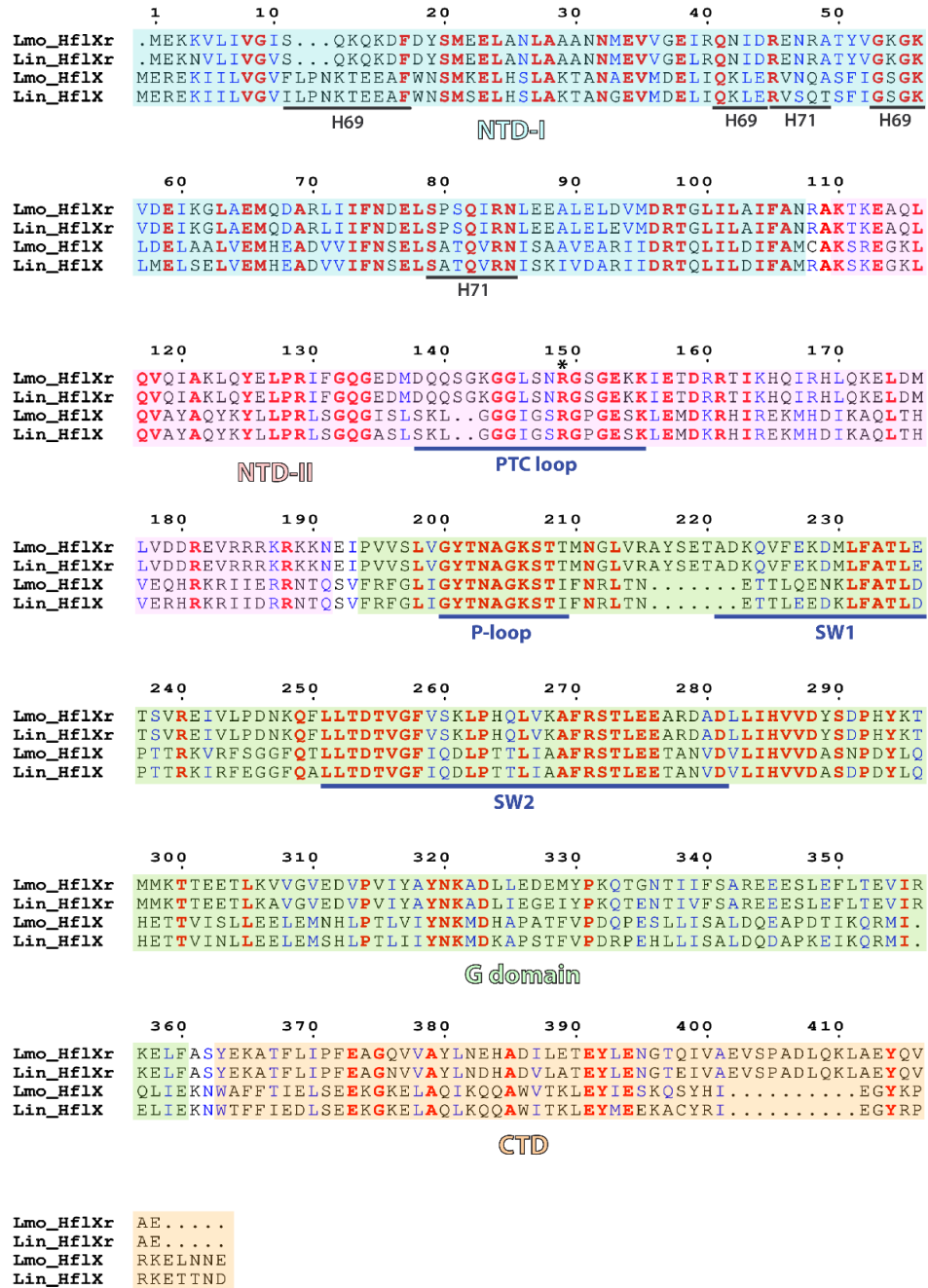


Figure 3.14. Sequence alignment of HflX and HflXr from *Listeria monocytogenes* and *Listeria innocua*. Identical residues are indicated in red and similar residues are blue. Domains of HflX and HflXr are colored and significant structural elements are labeled. Regions of the NTD-I interacting with helices H69 and H71 are underlined. Residue Arg149 is indicated with a black star. Reproduced with permission from Seely, S.M. et al. Nature Communications. 2023.¹¹¹

Bibliography / References

- [1] Seely, S. M., and Gagnon, M. G. (2022) Mechanisms of ribosome recycling in bacteria and mitochondria: a structural perspective, *RNA Biol* 19, 662-677.
- [2] Hussain, T., Llacer, J. L., Wimberly, B. T., Kieft, J. S., and Ramakrishnan, V. (2016) Large-Scale Movements of IF3 and tRNA during Bacterial Translation Initiation, *Cell* 167, 133-144 e113.
- [3] Sprink, T., Ramrath, D. J., Yamamoto, H., Yamamoto, K., Loerke, J., Ismer, J., Hildebrand, P. W., Scheerer, P., Burger, J., Mielke, T., and Spahn, C. M. (2016) Structures of ribosome-bound initiation factor 2 reveal the mechanism of subunit association, *Sci Adv* 2, e1501502.
- [4] Kaledhonkar, S., Fu, Z., Caban, K., Li, W., Chen, B., Sun, M., Gonzalez, R. L., Jr., and Frank, J. (2019) Late steps in bacterial translation initiation visualized using time-resolved cryo-EM, *Nature* 570, 400-404.
- [5] Gao, Y. G., Selmer, M., Dunham, C. M., Weixlbaumer, A., Kelley, A. C., and Ramakrishnan, V. (2009) The structure of the ribosome with elongation factor G trapped in the posttranslocational state, *Science* 326, 694-699.
- [6] Schmeing, T. M., Voorhees, R. M., Kelley, A. C., Gao, Y. G., Murphy, F. V. t., Weir, J. R., and Ramakrishnan, V. (2009) The crystal structure of the ribosome bound to EF-Tu and aminoacyl-tRNA, *Science* 326, 688-694.
- [7] Loveland, A. B., Demo, G., Grigorieff, N., and Korostelev, A. A. (2017) Ensemble cryo-EM elucidates the mechanism of translation fidelity, *Nature* 546, 113-117.
- [8] Loveland, A. B., Demo, G., and Korostelev, A. A. (2020) Cryo-EM of elongating ribosome with EF-Tu*GTP elucidates tRNA proofreading, *Nature* 584, 640-645.
- [9] Tourigny, D. S., Fernandez, I. S., Kelley, A. C., and Ramakrishnan, V. (2013) Elongation factor G bound to the ribosome in an intermediate state of translocation, *Science* 340, 1235490.
- [10] Zhou, J., Lancaster, L., Donohue, J. P., and Noller, H. F. (2013) Crystal structures of EF-G-ribosome complexes trapped in intermediate states of translocation, *Science* 340, 1236086.
- [11] Pulk, A., and Cate, J. H. (2013) Control of ribosomal subunit rotation by elongation factor G, *Science* 340, 1235970.
- [12] Petrychenko, V., Peng, B. Z., de, A. P. S. A. C., Peske, F., Rodnina, M. V., and Fischer, N. (2021) Structural mechanism of GTPase-powered ribosome-tRNA movement, *Nat Commun* 12, 5933.
- [13] Carbone, C. E., Loveland, A. B., Gamper, H. B., Jr., Hou, Y. M., Demo, G., and Korostelev, A. A. (2021) Time-resolved cryo-EM visualizes ribosomal translocation with EF-G and GTP, *Nat Commun* 12, 7236.
- [14] Salsi, E., Farah, E., Netter, Z., Dann, J., and Ermolenko, D. N. (2015) Movement of elongation factor G between compact and extended conformations, *J Mol Biol* 427, 454-467.
- [15] Stark, H., Rodnina, M. V., Wieden, H. J., van Heel, M., and Wintermeyer, W. (2000) Large-scale movement of elongation factor G and extensive conformational change of the ribosome during translocation, *Cell* 100, 301-309.
- [16] Lin, J., Gagnon, M. G., Bulkley, D., and Steitz, T. A. (2015) Conformational changes of elongation factor G on the ribosome during tRNA translocation, *Cell* 160, 219-227.
- [17] Zhang, W., Dunkle, J. A., and Cate, J. H. (2009) Structures of the ribosome in intermediate states of ratcheting, *Science* 325, 1014-1017.
- [18] Ratje, A. H., Loerke, J., Mikolajka, A., Brunner, M., Hildebrand, P. W., Starosta, A. L., Donhofer, A., Connell, S. R., Fucini, P., Mielke, T., Whitford, P. C., Onuchic, J. N., Yu, Y., Sanbonmatsu, K. Y., Hartmann, R. K., Penczek, P. A., Wilson, D. N., and Spahn, C. M. (2010) Head swivel

- on the ribosome facilitates translocation by means of intra-subunit tRNA hybrid sites, *Nature* 468, 713-716.
- [19] Guo, Z., and Noller, H. F. (2012) Rotation of the head of the 30S ribosomal subunit during mRNA translocation, *Proc Natl Acad Sci U S A* 109, 20391-20394.
- [20] Zhou, J., Lancaster, L., Donohue, J. P., and Noller, H. F. (2014) How the ribosome hands the A-site tRNA to the P site during EF-G-catalyzed translocation, *Science* 345, 1188-1191.
- [21] Frank, J., and Agrawal, R. K. (2000) A ratchet-like inter-subunit reorganization of the ribosome during translocation, *Nature* 406, 318-322.
- [22] Fu, Z., Indrisiunaite, G., Kaledhonkar, S., Shah, B., Sun, M., Chen, B., Grassucci, R. A., Ehrenberg, M., and Frank, J. (2019) The structural basis for release-factor activation during translation termination revealed by time-resolved cryogenic electron microscopy, *Nat Commun* 10, 2579.
- [23] Korostelev, A., Zhu, J., Asahara, H., and Noller, H. F. (2010) Recognition of the amber UAG stop codon by release factor RF1, *EMBO J* 29, 2577-2585.
- [24] Weixlbaumer, A., Jin, H., Neubauer, C., Voorhees, R. M., Petry, S., Kelley, A. C., and Ramakrishnan, V. (2008) Insights into translational termination from the structure of RF2 bound to the ribosome, *Science* 322, 953-956.
- [25] Laurberg, M., Asahara, H., Korostelev, A., Zhu, J., Trakhanov, S., and Noller, H. F. (2008) Structural basis for translation termination on the 70S ribosome, *Nature* 454, 852-857.
- [26] Korostelev, A., Asahara, H., Lancaster, L., Laurberg, M., Hirschi, A., Zhu, J., Trakhanov, S., Scott, W. G., and Noller, H. F. (2008) Crystal structure of a translation termination complex formed with release factor RF2, *Proc Natl Acad Sci U S A* 105, 19684-19689.
- [27] Petry, S., Brodersen, D. E., Murphy, F. V. t., Dunham, C. M., Selmer, M., Tarry, M. J., Kelley, A. C., and Ramakrishnan, V. (2005) Crystal structures of the ribosome in complex with release factors RF1 and RF2 bound to a cognate stop codon, *Cell* 123, 1255-1266.
- [28] Pallesen, J., Hashem, Y., Korkmaz, G., Koripella, R. K., Huang, C., Ehrenberg, M., Sanyal, S., and Frank, J. (2013) Cryo-EM visualization of the ribosome in termination complex with apo-RF3 and RF1, *Elife* 2, e00411.
- [29] Zhou, J., Lancaster, L., Trakhanov, S., and Noller, H. F. (2012) Crystal structure of release factor RF3 trapped in the GTP state on a rotated conformation of the ribosome, *RNA* 18, 230-240.
- [30] Jin, H., Kelley, A. C., and Ramakrishnan, V. (2011) Crystal structure of the hybrid state of ribosome in complex with the guanosine triphosphatase release factor 3, *Proc Natl Acad Sci U S A* 108, 15798-15803.
- [31] Fu, Z., Kaledhonkar, S., Borg, A., Sun, M., Chen, B., Grassucci, R. A., Ehrenberg, M., and Frank, J. (2016) Key Intermediates in Ribosome Recycling Visualized by Time-Resolved Cryoelectron Microscopy, *Structure* 24, 2092-2101.
- [32] Pai, R. D., Zhang, W., Schuwirth, B. S., Hirokawa, G., Kaji, H., Kaji, A., and Cate, J. H. (2008) Structural Insights into ribosome recycling factor interactions with the 70S ribosome, *J. Mol. Biol.* 376, 1334-1347.
- [33] Weixlbaumer, A., Petry, S., Dunham, C. M., Selmer, M., Kelley, A. C., and Ramakrishnan, V. (2007) Crystal structure of the ribosome recycling factor bound to the ribosome, *Nat Struct Mol Biol* 14, 733-737.
- [34] Borovinskaya, M. A., Pai, R. D., Zhang, W., Schuwirth, B. S., Holton, J. M., Hirokawa, G., Kaji, H., Kaji, A., and Cate, J. H. (2007) Structural basis for aminoglycoside inhibition of bacterial ribosome recycling, *Nat Struct Mol Biol* 14, 727-732.
- [35] Kim, K. K., Min, K., and Suh, S. W. (2000) Crystal structure of the ribosome recycling factor from *Escherichia coli*, *EMBO J* 19, 2362-2370.

- [36] Selmer, M., Al-Karadaghi, S., Hirokawa, G., Kaji, A., and Liljas, A. (1999) Crystal structure of *Thermotoga maritima* ribosome recycling factor: a tRNA mimic, *Science* **286**, 2349-2352.
- [37] Toyoda, T., Tin, O. F., Ito, K., Fujiwara, T., Kumasaka, T., Yamamoto, M., Garber, M. B., and Nakamura, Y. (2000) Crystal structure combined with genetic analysis of the *Thermus thermophilus* ribosome recycling factor shows that a flexible hinge may act as a functional switch, *RNA* **6**, 1432-1444.
- [38] Yoshida, T., Uchiyama, S., Nakano, H., Kashimori, H., Kijima, H., Ohshima, T., Saihara, Y., Ishino, T., Shimahara, H., Yoshida, T., Yokose, K., Ohkubo, T., Kaji, A., and Kobayashi, Y. (2001) Solution structure of the ribosome recycling factor from *Aquifex aeolicus*, *Biochemistry* **40**, 2387-2396.
- [39] Janosi, L., Mottagui-Tabar, S., Isaksson, L. A., Sekine, Y., Ohtsubo, E., Zhang, S., Goon, S., Nelken, S., Shuda, M., and Kaji, A. (1998) Evidence for in vivo ribosome recycling, the fourth step in protein biosynthesis, *EMBO J* **17**, 1141-1151.
- [40] Janosi, L., Shimizu, I., and Kaji, A. (1994) Ribosome recycling factor (ribosome releasing factor) is essential for bacterial growth, *Proc Natl Acad Sci U S A* **91**, 4249-4253.
- [41] Pavlov, M. Y., Freistroffer, D. V., Heurgue-Hamard, V., Buckingham, R. H., and Ehrenberg, M. (1997) Release factor RF3 abolishes competition between release factor RF1 and ribosome recycling factor (RRF) for a ribosome binding site, *J Mol Biol* **273**, 389-401.
- [42] Lancaster, L., Kiel, M. C., Kaji, A., and Noller, H. F. (2002) Orientation of ribosome recycling factor in the ribosome from directed hydroxyl radical probing, *Cell* **111**, 129-140.
- [43] Guo, P., Zhang, L., Zhang, H., Feng, Y., and Jing, G. (2006) Domain II plays a crucial role in the function of ribosome recycling factor, *Biochem J* **393**, 767-777.
- [44] Agrawal, R. K., Sharma, M. R., Kiel, M. C., Hirokawa, G., Booth, T. M., Spahn, C. M., Grassucci, R. A., Kaji, A., and Frank, J. (2004) Visualization of ribosome-recycling factor on the *Escherichia coli* 70S ribosome: functional implications, *Proc Natl Acad Sci U S A* **101**, 8900-8905.
- [45] Ali, I. K., Lancaster, L., Feinberg, J., Joseph, S., and Noller, H. F. (2006) Deletion of a conserved, central ribosomal intersubunit RNA bridge, *Mol Cell* **23**, 865-874.
- [46] Wilson, D. N., Schluenzen, F., Harms, J. M., Yoshida, T., Ohkubo, T., Albrecht, R., Buerger, J., Kobayashi, Y., and Fucini, P. (2005) X-ray crystallography study on ribosome recycling: the mechanism of binding and action of RRF on the 50S ribosomal subunit, *EMBO J* **24**, 251-260.
- [47] Hirokawa, G., Kiel, M. C., Muto, A., Selmer, M., Raj, V. S., Liljas, A., Igarashi, K., Kaji, H., and Kaji, A. (2002) Post-termination complex disassembly by ribosome recycling factor, a functional tRNA mimic, *EMBO J* **21**, 2272-2281.
- [48] Hirokawa, G., Kiel, M. C., Muto, A., Kawai, G., Igarashi, K., Kaji, H., and Kaji, A. (2002) Binding of ribosome recycling factor to ribosomes, comparison with tRNA, *J Biol Chem* **277**, 35847-35852.
- [49] Kiel, M. C., Raj, V. S., Kaji, H., and Kaji, A. (2003) Release of ribosome-bound ribosome recycling factor by elongation factor G, *J Biol Chem* **278**, 48041-48050.
- [50] Cornish, P. V., Ermolenko, D. N., Noller, H. F., and Ha, T. (2008) Spontaneous intersubunit rotation in single ribosomes, *Mol Cell* **30**, 578-588.
- [51] Frank, J., Gao, H., Sengupta, J., Gao, N., and Taylor, D. J. (2007) The process of mRNA-tRNA translocation, *Proc Natl Acad Sci U S A* **104**, 19671-19678.
- [52] Zhou, J., Lancaster, L., Donohue, J. P., and Noller, H. F. (2019) Spontaneous ribosomal translocation of mRNA and tRNAs into a chimeric hybrid state, *Proc Natl Acad Sci U S A* **116**, 7813-7818.

- [53] Gao, N., Zavialov, A. V., Li, W., Sengupta, J., Valle, M., Gursky, R. P., Ehrenberg, M., and Frank, J. (2005) Mechanism for the disassembly of the posttermination complex inferred from cryo-EM studies, *Mol. Cell* 18, 663-674.
- [54] Sternberg, S. H., Fei, J., Prywes, N., McGrath, K. A., and Gonzalez, R. L., Jr. (2009) Translation factors direct intrinsic ribosome dynamics during translation termination and ribosome recycling, *Nat Struct Mol Biol* 16, 861-868.
- [55] Prabhakar, A., Capece, M. C., Petrov, A., Choi, J., and Puglisi, J. D. (2017) Post-termination Ribosome Intermediate Acts as the Gateway to Ribosome Recycling, *Cell Rep* 20, 161-172.
- [56] Valle, M., Zavialov, A., Sengupta, J., Rawat, U., Ehrenberg, M., and Frank, J. (2003) Locking and unlocking of ribosomal motions, *Cell* 114, 123-134.
- [57] Dunkle, J. A., Wang, L., Feldman, M. B., Pulk, A., Chen, V. B., Kapral, G. J., Noeske, J., Richardson, J. S., Blanchard, S. C., and Cate, J. H. (2011) Structures of the bacterial ribosome in classical and hybrid states of tRNA binding, *Science* 332, 981-984.
- [58] Pavlov, M. Y., Antoun, A., Lovmar, M., and Ehrenberg, M. (2008) Complementary roles of initiation factor 1 and ribosome recycling factor in 70S ribosome splitting, *EMBO J* 27, 1706-1717.
- [59] Karimi, R., Pavlov, M. Y., Buckingham, R. H., and Ehrenberg, M. (1999) Novel roles for classical factors at the interface between translation termination and initiation, *Mol Cell* 3, 601-609.
- [60] Zavialov, A. V., Hauryliuk, V. V., and Ehrenberg, M. (2005) Splitting of the posttermination ribosome into subunits by the concerted action of RRF and EF-G, *Mol Cell* 18, 675-686.
- [61] Barat, C., Datta, P. P., Raj, V. S., Sharma, M. R., Kaji, H., Kaji, A., and Agrawal, R. K. (2007) Progression of the ribosome recycling factor through the ribosome dissociates the two ribosomal subunits, *Mol Cell* 27, 250-261.
- [62] Borg, A., Pavlov, M., and Ehrenberg, M. (2016) Complete kinetic mechanism for recycling of the bacterial ribosome, *RNA* 22, 10-21.
- [63] Zhou, D., Tanzawa, T., Lin, J., and Gagnon, M. G. (2020) Structural basis for ribosome recycling by RRF and tRNA, *Nat Struct Mol Biol* 27, 25-32.
- [64] Gagnon, M. G., Seetharaman, S. V., Bulkley, D., and Steitz, T. A. (2012) Structural basis for the rescue of stalled ribosomes: structure of YaeJ bound to the ribosome, *Science* 335, 1370-1372.
- [65] Polikanov, Y. S., Steitz, T. A., and Innis, C. A. (2014) A proton wire to couple aminoacyl-tRNA accommodation and peptide-bond formation on the ribosome, *Nat Struct Mol Biol* 21, 787-793.
- [66] Polikanov, Y. S., Blaha, G. M., and Steitz, T. A. (2012) How hibernation factors RMF, HPF, and YfiA turn off protein synthesis, *Science* 336, 915-918.
- [67] Kim, L. Y., Rice, W. J., Eng, E. T., Kopylov, M., Cheng, A., Raczkowski, A. M., Jordan, K. D., Bobe, D., Potter, C. S., and Carragher, B. (2018) Benchmarking cryo-EM Single Particle Analysis Workflow, *Front Mol Biosci* 5, 50.
- [68] Rivera-Calzada, A., and Carroni, M. (2019) Editorial: Technical Advances in Cryo-Electron Microscopy, *Front Mol Biosci* 6, 72.
- [69] Frank, J. (2017) Time-resolved cryo-electron microscopy: Recent progress, *J Struct Biol* 200, 303-306.
- [70] Yokoyama, T., Shaikh, T. R., Iwakura, N., Kaji, H., Kaji, A., and Agrawal, R. K. (2012) Structural insights into initial and intermediate steps of the ribosome-recycling process, *EMBO J* 31, 1836-1846.

- [71] Ito, K., Fujiwara, T., Toyoda, T., and Nakamura, Y. (2002) Elongation factor G participates in ribosome disassembly by interacting with ribosome recycling factor at their tRNA-mimicry domains, *Mol Cell* 9, 1263-1272.
- [72] Fujiwara, T., Ito, K., Nakayashiki, T., and Nakamura, Y. (1999) Amber mutations in ribosome recycling factors of *Escherichia coli* and *Thermus thermophilus*: evidence for C-terminal modulator element, *FEBS Lett* 447, 297-302.
- [73] Fujiwara, T., Ito, K., Yamami, T., and Nakamura, Y. (2004) Ribosome recycling factor disassembles the post-termination ribosomal complex independent of the ribosomal translocase activity of elongation factor G, *Mol Microbiol* 53, 517-528.
- [74] Peske, F., Rodnina, M. V., and Wintermeyer, W. (2005) Sequence of steps in ribosome recycling as defined by kinetic analysis, *Mol Cell* 18, 403-412.
- [75] Koripella, R. K., Deep, A., Agrawal, E. K., Keshavan, P., Banavali, N. K., and Agrawal, R. K. (2021) Distinct mechanisms of the human mitoribosome recycling and antibiotic resistance, *Nat Commun* 12, 3607.
- [76] Gao, N., Zavialov, A. V., Ehrenberg, M., and Frank, J. (2007) Specific interaction between EF-G and RRF and its implication for GTP-dependent ribosome splitting into subunits, *J Mol Biol* 374, 1345-1358.
- [77] Demo, G., Gamper, H. B., Loveland, A. B., Masuda, I., Carbone, C. E., Svidritskiy, E., Hou, Y. M., and Korostelev, A. A. (2021) Structural basis for +1 ribosomal frameshifting during EF-G-catalyzed translocation, *Nat Commun* 12, 4644.
- [78] Margus, T., Remm, M., and Tenson, T. (2011) A computational study of elongation factor G (EFG) duplicated genes: diverged nature underlying the innovation on the same structural template, *PLoS One* 6, e22789.
- [79] Margus, T., Remm, M., and Tenson, T. (2007) Phylogenetic distribution of translational GTPases in bacteria, *BMC Genomics* 8, 15.
- [80] Connell, S. R., Takemoto, C., Wilson, D. N., Wang, H., Murayama, K., Terada, T., Shirouzu, M., Rost, M., Schuler, M., Giesebrecht, J., Dabrowski, M., Mielke, T., Fucini, P., Yokoyama, S., and Spahn, C. M. (2007) Structural basis for interaction of the ribosome with the switch regions of GTP-bound elongation factors, *Mol Cell* 25, 751-764.
- [81] Seshadri, A., Samhita, L., Gaur, R., Malshetty, V., and Varshney, U. (2009) Analysis of the fusA2 locus encoding EFG2 in *Mycobacterium smegmatis*, *Tuberculosis (Edinb)* 89, 453-464.
- [82] Palmer, S. O., Rangel, E. Y., Hu, Y., Tran, A. T., and Bullard, J. M. (2013) Two homologous EF-G proteins from *Pseudomonas aeruginosa* exhibit distinct functions, *PLoS One* 8, e80252.
- [83] Suematsu, T., Yokobori, S., Morita, H., Yoshinari, S., Ueda, T., Kita, K., Takeuchi, N., and Watanabe, Y. (2010) A bacterial elongation factor G homologue exclusively functions in ribosome recycling in the spirochaete *Borrelia burgdorferi*, *Mol Microbiol* 75, 1445-1454.
- [84] Recht, M. I., Douthwaite, S., and Puglisi, J. D. (1999) Basis for prokaryotic specificity of action of aminoglycoside antibiotics, *EMBO J* 18, 3133-3138.
- [85] Moazed, D., and Noller, H. F. (1987) Interaction of antibiotics with functional sites in 16S ribosomal RNA, *Nature* 327, 389-394.
- [86] Russell, R. J., Murray, J. B., Lentzen, G., Haddad, J., and Mobashery, S. (2003) The complex of a designer antibiotic with a model aminoacyl site of the 30S ribosomal subunit revealed by X-ray crystallography, *J Am Chem Soc* 125, 3410-3411.
- [87] Fourmy, D., Recht, M. I., Blanchard, S. C., and Puglisi, J. D. (1996) Structure of the A site of *Escherichia coli* 16S ribosomal RNA complexed with an aminoglycoside antibiotic, *Science* 274, 1367-1371.
- [88] Francois, B., Russell, R. J., Murray, J. B., Aboul-ela, F., Masquida, B., Vicens, Q., and Westhof, E. (2005) Crystal structures of complexes between aminoglycosides and decoding A site

- oligonucleotides: role of the number of rings and positive charges in the specific binding leading to miscoding, *Nucleic Acids Res* 33, 5677-5690.
- [89] Vicens, Q., and Westhof, E. (2003) Crystal structure of geneticin bound to a bacterial 16S ribosomal RNA A site oligonucleotide, *J Mol Biol* 326, 1175-1188.
- [90] Lescoute, A., and Westhof, E. (2006) The A-minor motifs in the decoding recognition process, *Biochimie* 88, 993-999.
- [91] Kondo, J., Francois, B., Russell, R. J., Murray, J. B., and Westhof, E. (2006) Crystal structure of the bacterial ribosomal decoding site complexed with amikacin containing the gamma-amino-alpha-hydroxybutyryl (haba) group, *Biochimie* 88, 1027-1031.
- [92] Krause, K. M., Serio, A. W., Kane, T. R., and Connolly, L. E. (2016) Aminoglycosides: An Overview, *Cold Spring Harb Perspect Med* 6.
- [93] Nicholson, D., Edwards, T. A., O'Neill, A. J., and Ranson, N. A. (2020) Structure of the 70S Ribosome from the Human Pathogen *Acinetobacter baumannii* in Complex with Clinically Relevant Antibiotics, *Structure* 28, 1087-1100 e1083.
- [94] Zhang, Y., Mandava, C. S., Cao, W., Li, X., Zhang, D., Li, N., Zhang, Y., Zhang, X., Qin, Y., Mi, K., Lei, J., Sanyal, S., and Gao, N. (2015) HflX is a ribosome-splitting factor rescuing stalled ribosomes under stress conditions, *Nat Struct Mol Biol* 22, 906-913.
- [95] Park, J. H., Jensen, B. C., Kifer, C. T., and Parsons, M. (2001) A novel nucleolar G-protein conserved in eukaryotes, *J Cell Sci* 114, 173-185.
- [96] Jain, N., Dhimole, N., Khan, A. R., De, D., Tomar, S. K., Sajish, M., Dutta, D., Parrack, P., and Prakash, B. (2009) E. coli HflX interacts with 50S ribosomal subunits in presence of nucleotides, *Biochem Biophys Res Commun* 379, 201-205.
- [97] Blombach, F., Launay, H., Zorraquino, V., Swarts, D. C., Cabrita, L. D., Benelli, D., Christodoulou, J., Londei, P., and van der Oost, J. (2011) An HflX-type GTPase from *Sulfolobus solfataricus* binds to the 50S ribosomal subunit in all nucleotide-bound states, *J Bacteriol* 193, 2861-2867.
- [98] Fischer, J. J., Coatham, M. L., Bear, S. E., Brandon, H. E., De Laurentis, E. I., Shields, M. J., and Wieden, H. J. (2012) The ribosome modulates the structural dynamics of the conserved GTPase HflX and triggers tight nucleotide binding, *Biochimie* 94, 1647-1659.
- [99] Shields, M. J., Fischer, J. J., and Wieden, H. J. (2009) Toward understanding the function of the universally conserved GTPase HflX from *Escherichia coli*: a kinetic approach, *Biochemistry* 48, 10793-10802.
- [100] Baba, T., Ara, T., Hasegawa, M., Takai, Y., Okumura, Y., Baba, M., Datsenko, K. A., Tomita, M., Wanner, B. L., and Mori, H. (2006) Construction of *Escherichia coli* K-12 in-frame, single-gene knockout mutants: the Keio collection, *Mol Syst Biol* 2, 2006 0008.
- [101] Tsui, H. C., Feng, G., and Winkler, M. E. (1996) Transcription of the mutL repair, miaA tRNA modification, hfq pleiotropic regulator, and hflA region protease genes of *Escherichia coli* K-12 from clustered σ^{32} -specific promoters during heat shock, *J Bacteriol* 178, 5719-5731.
- [102] Tsui, H. C., Leung, H. C., and Winkler, M. E. (1994) Characterization of broadly pleiotropic phenotypes caused by an hfq insertion mutation in *Escherichia coli* K-12, *Mol Microbiol* 13, 35-49.
- [103] Shalgi, R., Hurt, J. A., Krykbaeva, I., Taipale, M., Lindquist, S., and Burge, C. B. (2013) Widespread regulation of translation by elongation pausing in heat shock, *Mol Cell* 49, 439-452.
- [104] Coatham, M. L., Brandon, H. E., Fischer, J. J., Schummer, T., and Wieden, H. J. (2016) The conserved GTPase HflX is a ribosome splitting factor that binds to the E-site of the bacterial ribosome, *Nucleic Acids Res* 44, 1952-1961.

- [105] Hurst-Hess, K. R., Rudra, P., and Ghosh, P. (2021) Ribosome Protection as a Mechanism of Lincosamide Resistance in *Mycobacterium abscessus*, *Antimicrob Agents Chemother* 65, e0118421.
- [106] Rudra, P., Hurst-Hess, K. R., Cotten, K. L., Partida-Miranda, A., and Ghosh, P. (2020) Mycobacterial HflX is a ribosome splitting factor that mediates antibiotic resistance, *Proc Natl Acad Sci U S A* 117, 629-634.
- [107] Burian, J., Ramon-Garcia, S., Howes, C. G., and Thompson, C. J. (2012) WhiB7, a transcriptional activator that coordinates physiology with intrinsic drug resistance in *Mycobacterium tuberculosis*, *Expert Rev Anti Infect Ther* 10, 1037-1047.
- [108] Burian, J., and Thompson, C. J. (2018) Regulatory genes coordinating antibiotic-induced changes in promoter activity and early transcriptional termination of the mycobacterial intrinsic resistance gene whiB7, *Mol Microbiol* 107, 402-415.
- [109] Svetlov, M. S., Plessa, E., Chen, C. W., Bougas, A., Krokidis, M. G., Dinos, G. P., and Polikanov, Y. S. (2019) High-resolution crystal structures of ribosome-bound chloramphenicol and erythromycin provide the ultimate basis for their competition, *RNA* 25, 600-606.
- [110] Duval, M., Dar, D., Carvalho, F., Rocha, E. P. C., Sorek, R., and Cossart, P. (2018) HflXr, a homolog of a ribosome-splitting factor, mediates antibiotic resistance, *Proc Natl Acad Sci U S A* 115, 13359-13364.
- [111] Seely, S. M., Parajuli, N. P., De Tarafder, A., Ge, X., Sanyal, S., and Gagnon, M. G. (2023) Molecular basis of the pleiotropic effects by the antibiotic amikacin on the ribosome, *Nat Commun* 14, 4666.
- [112] Lin, J., Zhou, D., Steitz, T. A., Polikanov, Y. S., and Gagnon, M. G. (2018) Ribosome-Targeting Antibiotics: Modes of Action, Mechanisms of Resistance, and Implications for Drug Design, *Annu Rev Biochem* 87, 451-478.
- [113] Wasserman, M. R., Pulk, A., Zhou, Z., Altman, R. B., Zinder, J. C., Green, K. D., Garneau-Tsodikova, S., Cate, J. H., and Blanchard, S. C. (2015) Chemically related 4,5-linked aminoglycoside antibiotics drive subunit rotation in opposite directions, *Nat Commun* 6, 7896.
- [114] Feldman, M. B., Terry, D. S., Altman, R. B., and Blanchard, S. C. (2010) Aminoglycoside activity observed on single pre-translocation ribosome complexes, *Nat Chem Biol* 6, 244.
- [115] Powers, K. T., Stevenson-Jones, F., Yadav, S. K. N., Amthor, B., Bufton, J. C., Borucu, U., Shen, D., Becker, J. P., Lavysch, D., Hentze, M. W., Kulozik, A. E., Neu-Yilik, G., and Schaffitzel, C. (2021) Blastcidin S inhibits mammalian translation and enhances production of protein encoded by nonsense mRNA, *Nucleic Acids Res* 49, 7665-7679.
- [116] Svidritskiy, E., and Korostelev, A. A. (2018) Conformational Control of Translation Termination on the 70S Ribosome, *Structure* 26, 821-828 e823.
- [117] Hansen, J. L., Moore, P. B., and Steitz, T. A. (2003) Structures of five antibiotics bound at the peptidyl transferase center of the large ribosomal subunit, *J Mol Biol* 330, 1061-1075.
- [118] Svidritskiy, E., and Korostelev, A. A. (2018) Mechanism of Inhibition of Translation Termination by Blastcidin S, *J Mol Biol* 430, 591-593.
- [119] Amunts, A., Fiedorczuk, K., Truong, T. T., Chandler, J., Greenberg, E. P., and Ramakrishnan, V. (2015) Bactobolin A binds to a site on the 70S ribosome distinct from previously seen antibiotics, *J Mol Biol* 427, 753-755.
- [120] Parajuli, N. P., Mandava, C. S., Pavlov, M. Y., and Sanyal, S. (2021) Mechanistic insights into translation inhibition by aminoglycoside antibiotic arbekacin, *Nucleic Acids Res* 49, 6880-6892.
- [121] Cabanas, M. J., Vazquez, D., and Modolell, J. (1978) Inhibition of ribosomal translocation by aminoglycoside antibiotics, *Biochem Biophys Res Commun* 83, 991-997.

- [122] Studer, S. M., Feinberg, J. S., and Joseph, S. (2003) Rapid kinetic analysis of EF-G-dependent mRNA translocation in the ribosome, *J Mol Biol* 327, 369-381.
- [123] Ying, L., Zhu, H., Shoji, S., and Fredrick, K. (2019) Roles of specific aminoglycoside-ribosome interactions in the inhibition of translation, *RNA* 25, 247-254.
- [124] Kim, C., Holm, M., Mandava, C. S., and Sanyal, S. (2021) Optimization of a fluorescent-mRNA based real-time assay for precise kinetic measurements of ribosomal translocation, *RNA Biol* 18, 2363-2375.
- [125] VanLoock, M. S., Agrawal, R. K., Gabashvili, I. S., Qi, L., Frank, J., and Harvey, S. C. (2000) Movement of the decoding region of the 16 S ribosomal RNA accompanies tRNA translocation, *J Mol Biol* 304, 507-515.
- [126] Brown, C. M., McCaughan, K. K., and Tate, W. P. (1993) Two regions of the Escherichia coli 16S ribosomal RNA are important for decoding stop signals in polypeptide chain termination, *Nucleic Acids Res* 21, 2109-2115.
- [127] Youngman, E. M., He, S. L., Nikstad, L. J., and Green, R. (2007) Stop codon recognition by release factors induces structural rearrangement of the ribosomal decoding center that is productive for peptide release, *Mol Cell* 28, 533-543.
- [128] Ogawa, K., and Kaji, A. (1975) Requirement for ribosome-releasing factor for the release of ribosomes at the termination codon, *Eur J Biochem* 58, 411-419.
- [129] Hirashima, A., and Kaji, A. (1972) Factor-dependent release of ribosomes from messenger RNA. Requirement for two heat-stable factors, *J Mol Biol* 65, 43-58.
- [130] Tsai, A., Uemura, S., Johansson, M., Puglisi, E. V., Marshall, R. A., Aitken, C. E., Korlach, J., Ehrenberg, M., and Puglisi, J. D. (2013) The impact of aminoglycosides on the dynamics of translation elongation, *Cell Rep* 3, 497-508.
- [131] Cassir, N., Rolain, J. M., and Brouqui, P. (2014) A new strategy to fight antimicrobial resistance: the revival of old antibiotics, *Front Microbiol* 5, 551.
- [132] Carlson-Banning, K. M., Chou, A., Liu, Z., Hamill, R. J., Song, Y., and Zechiedrich, L. (2013) Toward repurposing ciclopirox as an antibiotic against drug-resistant *Acinetobacter baumannii*, *Escherichia coli*, and *Klebsiella pneumoniae*, *PLoS One* 8, e69646.
- [133] Zhou, J., Bhattacharjee, A., Chen, S., Chen, Y., Duffy, E., Farmer, J., Goldberg, J., Hanselmann, R., Ippolito, J. A., Lou, R., Orbin, A., Oyelere, A., Salvino, J., Springer, D., Tran, J., Wang, D., Wu, Y., and Johnson, G. (2008) Design at the atomic level: generation of novel hybrid biaryloxazolidinones as promising new antibiotics, *Bioorg Med Chem Lett* 18, 6179-6183.
- [134] Ippolito, J. A., Kanyo, Z. F., Wang, D., Franceschi, F. J., Moore, P. B., Steitz, T. A., and Duffy, E. M. (2008) Crystal structure of the oxazolidinone antibiotic linezolid bound to the 50S ribosomal subunit, *J Med Chem* 51, 3353-3356.
- [135] Chan, J., Khan, S. N., Harvey, I., Merrick, W., and Pelletier, J. (2004) Eukaryotic protein synthesis inhibitors identified by comparison of cytotoxicity profiles, *RNA* 10, 528-543.
- [136] Hori, M., Suzukake, K., Ishikawa, C., Asakura, H., and Umezawa, H. (1981) Biochemical studies on bactobolin in relation to actinobolin, *J Antibiot (Tokyo)* 34, 465-468.
- [137] Kondo, S., Horiuchi, Y., Hamada, M., Takeuchi, T., and Umezawa, H. (1979) A new antitumor antibiotic, bactobolin produced by *Pseudomonas*, *J Antibiot (Tokyo)* 32, 1069-1071.
- [138] Svidritskiy, E., Ling, C., Ermolenko, D. N., and Korostelev, A. A. (2013) Blastidicin S inhibits translation by trapping deformed tRNA on the ribosome, *Proc Natl Acad Sci U S A* 110, 12283-12288.
- [139] Greenberg, E. P., Chandler, J. R., and Seyedsayamdost, M. R. (2020) The Chemistry and Biology of Bactobolin: A 10-Year Collaboration with Natural Product Chemist Extraordinaire Jon Clardy, *J Nat Prod* 83, 738-743.

- [140] Davison, J. R., Lohith, K. M., Wang, X., Bobyk, K., Mandadapu, S. R., Lee, S. L., Cencic, R., Nelson, J., Simpkins, S., Frank, K. M., Pelletier, J., Myers, C. L., Piotrowski, J., Smith, H. E., and Bewley, C. A. (2017) A New Natural Product Analog of Blasticidin S Reveals Cellular Uptake Facilitated by the NorA Multidrug Transporter, *Antimicrob Agents Chemother* 61.
- [141] Housman, S. T., Sutherland, C., and Nicolau, D. P. (2012) In vitro evaluation of novel compounds against selected resistant *Pseudomonas aeruginosa* isolates, *Antimicrob Agents Chemother* 56, 1646-1649.
- [142] Adachi, H., Nishimura, Y., and Takeuchi, T. (2002) Synthesis and activities of bactobolin derivatives having new functionality at C-3, *J Antibiot (Tokyo)* 55, 92-98.
- [143] Adachi, H., Usui, T., Nishimura, Y., Kondo, S., Ishizuka, M., and Takeuchi, T. (1998) Synthesis and activities of bactobolin derivatives based on the alteration of the functionality at C-3 position, *J Antibiot (Tokyo)* 51, 184-188.
- [144] Aguirre Rivera, J., Larsson, J., Volkov, I. L., Seefeldt, A. C., Sanyal, S., and Johansson, M. (2021) Real-time measurements of aminoglycoside effects on protein synthesis in live cells, *Proc Natl Acad Sci U S A* 118.
- [145] Johansson, M., Bouakaz, E., Lovmar, M., and Ehrenberg, M. (2008) The kinetics of ribosomal peptidyl transfer revisited, *Mol Cell* 30, 589-598.
- [146] Junemann, R., Wadzack, J., Triana-Alonso, F. J., Bittner, J. U., Caillet, J., Meinnel, T., Vanatalu, K., and Nierhaus, K. H. (1996) In vivo deuteration of transfer RNAs: overexpression and large-scale purification of deuterated specific tRNAs, *Nucleic Acids Res* 24, 907-913.
- [147] Pundir, S., Ge, X., and Sanyal, S. (2021) GGQ methylation enhances both speed and accuracy of stop codon recognition by bacterial class-I release factors, *J Biol Chem* 296, 100681.
- [148] Antoun, A., Pavlov, M. Y., Tenson, T., and Ehrenberg, M. M. (2004) Ribosome formation from subunits studied by stopped-flow and Rayleigh light scattering, *Biol Proced Online* 6, 35-54.
- [149] Paranjpe, M. N., Marina, V. I., Grachev, A. A., Maviza, T. P., Tolicheva, O. A., Paleskava, A., Osterman, I. A., Sergiev, P. V., Konevega, A. L., Polikanov, Y. S., and Gagnon, M. G. (2023) Insights into the molecular mechanism of translation inhibition by the ribosome-targeting antibiotic thermorubin, *Nucleic Acids Res* 51, 449-462.
- [150] Kabsch, W. (2010) Xds, *Acta Crystallogr D Biol Crystallogr* 66, 125-132.
- [151] McCoy, A. J., Grosse-Kunstleve, R. W., Adams, P. D., Winn, M. D., Storoni, L. C., and Read, R. J. (2007) Phaser crystallographic software, *J Appl Crystallogr* 40, 658-674.
- [152] Adams, P. D., Grosse-Kunstleve, R. W., Hung, L. W., Ioerger, T. R., McCoy, A. J., Moriarty, N. W., Read, R. J., Sacchettini, J. C., Sauter, N. K., and Terwilliger, T. C. (2002) PHENIX: building new software for automated crystallographic structure determination, *Acta Crystallogr D Biol Crystallogr* 58, 1948-1954.
- [153] Moriarty, N. W., Grosse-Kunstleve, R. W., and Adams, P. D. (2009) electronic Ligand Builder and Optimization Workbench (eLBOW): a tool for ligand coordinate and restraint generation, *Acta Crystallogr D Biol Crystallogr* 65, 1074-1080.
- [154] Emsley, P., Lohkamp, B., Scott, W. G., and Cowtan, K. (2010) Features and development of Coot, *Acta Crystallogr D Biol Crystallogr* 66, 486-501.
- [155] Liebschner, D., Afonine, P. V., Baker, M. L., Bunkoczi, G., Chen, V. B., Croll, T. I., Hintze, B., Hung, L. W., Jain, S., McCoy, A. J., Moriarty, N. W., Oeffner, R. D., Poon, B. K., Prisant, M. G., Read, R. J., Richardson, J. S., Richardson, D. C., Sammito, M. D., Sobolev, O. V., Stockwell, D. H., Terwilliger, T. C., Urzhumtsev, A. G., Videau, L. L., Williams, C. J., and Adams, P. D. (2019) Macromolecular structure determination using X-rays, neutrons and electrons: recent developments in Phenix, *Acta Crystallogr D Struct Biol* 75, 861-877.

- [156] Mastronarde, D. N. (2005) Automated electron microscope tomography using robust prediction of specimen movements, *J Struct Biol* 152, 36-51.
- [157] Punjani, A., Rubinstein, J. L., Fleet, D. J., and Brubaker, M. A. (2017) cryoSPARC: algorithms for rapid unsupervised cryo-EM structure determination, *Nat Methods* 14, 290-296.
- [158] Punjani, A., and Fleet, D. J. (2021) 3D variability analysis: Resolving continuous flexibility and discrete heterogeneity from single particle cryo-EM, *J Struct Biol* 213, 107702.
- [159] Afonine, P. V., Klaholz, B. P., Moriarty, N. W., Poon, B. K., Sobolev, O. V., Terwilliger, T. C., Adams, P. D., and Urzhumtsev, A. (2018) New tools for the analysis and validation of cryo-EM maps and atomic models, *Acta Crystallogr D Struct Biol* 74, 814-840.
- [160] Pettersen, E. F., Goddard, T. D., Huang, C. C., Couch, G. S., Greenblatt, D. M., Meng, E. C., and Ferrin, T. E. (2004) UCSF Chimera--a visualization system for exploratory research and analysis, *J Comput Chem* 25, 1605-1612.
- [161] Seely, S. M., Basu, R. S., and Gagnon, M. G. (2024) Mechanistic insights into the alternative ribosome recycling by HflXr, *Nucleic Acids Res.*
- [162] Brown, E. D. (2005) Conserved P-loop GTPases of unknown function in bacteria: an emerging and vital ensemble in bacterial physiology, *Biochem Cell Biol* 83, 738-746.
- [163] Sengupta, S., Mondal, A., Dutta, D., and Parrack, P. (2018) HflX protein protects *Escherichia coli* from manganese stress, *J Biosci* 43, 1001-1013.
- [164] Tsui, H. C., Zhao, G., Feng, G., Leung, H. C., and Winkler, M. E. (1994) The mutL repair gene of *Escherichia coli* K-12 forms a superoperon with a gene encoding a new cell-wall amidase, *Mol Microbiol* 11, 189-202.
- [165] Dey, S., Biswas, C., and Sengupta, J. (2018) The universally conserved GTPase HflX is an RNA helicase that restores heat-damaged *Escherichia coli* ribosomes, *J Cell Biol* 217, 2519-2529.
- [166] Koller, T. O., Turnbull, K. J., Vaitkevicius, K., Crowe-McAuliffe, C., Roghanian, M., Bulvas, O., Nakamoto, J. A., Kurata, T., Julius, C., Atkinson, G. C., Johansson, J., Haurlyliuk, V., and Wilson, D. N. (2022) Structural basis for HflXr-mediated antibiotic resistance in *Listeria monocytogenes*, *Nucleic Acids Res* 50, 11285-11300.
- [167] Hillen, H. S., Lavdovskaia, E., Nadler, F., Hanitsch, E., Linden, A., Bohnsack, K. E., Urlaub, H., and Richter-Dennerlein, R. (2021) Structural basis of GTPase-mediated mitochondrial ribosome biogenesis and recycling, *Nat Commun* 12, 3672.
- [168] Vazquez-Laslop, N., and Mankin, A. S. (2018) How Macrolide Antibiotics Work, *Trends Biochem Sci* 43, 668-684.
- [169] Bhattacharjee, S., Feng, X., Maji, S., Dadhwal, P., Zhang, Z., Brown, Z. P., and Frank, J. (2024) Time resolution in cryo-EM using a PDMS-based microfluidic chip assembly and its application to the study of HflX-mediated ribosome recycling, *Cell*.
- [170] Crowe-McAuliffe, C., Murina, V., Turnbull, K. J., Kasari, M., Mohamad, M., Polte, C., Takada, H., Vaitkevicius, K., Johansson, J., Ignatova, Z., Atkinson, G. C., O'Neill, A. J., Haurlyliuk, V., and Wilson, D. N. (2021) Structural basis of ABCF-mediated resistance to pleuromutilin, lincosamide, and streptogramin A antibiotics in Gram-positive pathogens, *Nat Commun* 12, 3577.
- [171] Jumper, J., Evans, R., Pritzel, A., Green, T., Figurnov, M., Ronneberger, O., Tunyasuvunakool, K., Bates, R., Zidek, A., Potapenko, A., Bridgland, A., Meyer, C., Kohl, S. A. A., Ballard, A. J., Cowie, A., Romera-Paredes, B., Nikolov, S., Jain, R., Adler, J., Back, T., Petersen, S., Reiman, D., Clancy, E., Zielinski, M., Steinegger, M., Pacholska, M., Berghammer, T., Bodenstein, S., Silver, D., Vinyals, O., Senior, A. W., Kavukcuoglu, K., Kohli, P., and Hassabis, D. (2021) Highly accurate protein structure prediction with AlphaFold, *Nature* 596, 583-589.

- [172] Pettersen, E. F., Goddard, T. D., Huang, C. C., Meng, E. C., Couch, G. S., Croll, T. I., Morris, J. H., and Ferrin, T. E. (2021) UCSF ChimeraX: Structure visualization for researchers, educators, and developers, *Protein Sci* 30, 70-82.
- [173] Grunberg-Manago, M., Dessen, P., Pantaloni, D., Godefroy-Colburn, T., Wolfe, A. D., and Dondon, J. (1975) Light-scattering studies showing the effect of initiation factors on the reversible dissociation of Escherichia coli ribosomes, *J Mol Biol* 94, 461-478.
- [174] Lavdovskaia, E., Denks, K., Nadler, F., Steube, E., Linden, A., Urlaub, H., Rodnina, M. V., and Richter-Dennerlein, R. (2020) Dual function of GTPBP6 in biogenesis and recycling of human mitochondrial ribosomes, *Nucleic Acids Res* 48, 12929-12942.
- [175] Bhattacharjee, S., Feng, X., Maji, S., Dadhwal, P., Zhang, Z., Brown, Z. P., and Frank, J. (2023) Time resolution in cryo-EM using a novel PDMS-based microfluidic chip assembly and its application to the study of HflX-mediated ribosome recycling, *bioRxiv*.
- [176] Krissinel, E., and Henrick, K. (2007) Inference of macromolecular assemblies from crystalline state, *J Mol Biol* 372, 774-797.
- [177] Ghosh, S., and Joseph, S. (2005) Nonbridging phosphate oxygens in 16S rRNA important for 30S subunit assembly and association with the 50S ribosomal subunit, *RNA* 11, 657-667.
- [178] Komoda, T., Sato, N. S., Phelps, S. S., Namba, N., Joseph, S., and Suzuki, T. (2006) The A-site finger in 23 S rRNA acts as a functional attenuator for translocation, *J Biol Chem* 281, 32303-32309.
- [179] Agafonov, D. E., Kolb, V. A., Nazimov, I. V., and Spirin, A. S. (1999) A protein residing at the subunit interface of the bacterial ribosome, *Proc Natl Acad Sci U S A* 96, 12345-12349.
- [180] Vila-Sanjurjo, A., Schuwirth, B. S., Hau, C. W., and Cate, J. H. (2004) Structural basis for the control of translation initiation during stress, *Nat Struct Mol Biol* 11, 1054-1059.
- [181] Sharma, M. R., Donhofer, A., Barat, C., Marquez, V., Datta, P. P., Fucini, P., Wilson, D. N., and Agrawal, R. K. (2010) PSRP1 is not a ribosomal protein, but a ribosome-binding factor that is recycled by the ribosome-recycling factor (RRF) and elongation factor G (EF-G), *J Biol Chem* 285, 4006-4014.
- [182] Bieri, P., Leibundgut, M., Saurer, M., Boehringer, D., and Ban, N. (2017) The complete structure of the chloroplast 70S ribosome in complex with translation factor pY, *EMBO J* 36, 475-486.
- [183] McKay, S. L., and Portnoy, D. A. (2015) Ribosome hibernation facilitates tolerance of stationary-phase bacteria to aminoglycosides, *Antimicrob. Agents Chemother.* 59, 6992-6999.
- [184] Liu, Q., and Fredrick, K. (2016) Intersubunit Bridges of the Bacterial Ribosome, *J Mol Biol* 428, 2146-2164.
- [185] Julian, P., Konevega, A. L., Scheres, S. H., Lazaro, M., Gil, D., Wintermeyer, W., Rodnina, M. V., and Valle, M. (2008) Structure of ratcheted ribosomes with tRNAs in hybrid states, *Proc Natl Acad Sci U S A* 105, 16924-16927.
- [186] Ermolenko, D. N., Majumdar, Z. K., Hickerson, R. P., Spiegel, P. C., Clegg, R. M., and Noller, H. F. (2007) Observation of intersubunit movement of the ribosome in solution using FRET, *J. Mol. Biol.* 370, 530-540.
- [187] Ling, C., and Ermolenko, D. N. (2015) Initiation factor 2 stabilizes the ribosome in a semirotated conformation, *Proc. Natl. Acad. Sci. U S A* 112, 15874-15879.
- [188] Basu, R. S., Sherman, M. B., and Gagnon, M. G. (2022) Compact IF2 allows initiator tRNA accommodation into the P site and gates the ribosome to elongation, *Nat. Commun.* 13, 3388.
- [189] Chen, Y., Feng, S., Kumar, V., Ero, R., and Gao, Y. G. (2013) Structure of EF-G-ribosome complex in a pretranslocation state, *Nat. Struct. Mol. Biol.* 20, 1077-1084.

- [190] Brilot, A. F., Korostelev, A. A., Ermolenko, D. N., and Grigorieff, N. (2013) Structure of the ribosome with elongation factor G trapped in the pretranslocation state, *Proc. Natl. Acad. Sci. U S A* *110*, 20994-20999.
- [191] Gao, H., Zhou, Z., Rawat, U., Huang, C., Bouakaz, L., Wang, C., Cheng, Z., Liu, Y., Zavialov, A., Gursky, R., Sanyal, S., Ehrenberg, M., Frank, J., and Song, H. (2007) RF3 induces ribosomal conformational changes responsible for dissociation of class I release factors, *Cell* *129*, 929-941.
- [192] Graf, M., Huter, P., Maracci, C., Peterek, M., Rodnina, M. V., and Wilson, D. N. (2018) Visualization of translation termination intermediates trapped by the Apidaecin 137 peptide during RF3-mediated recycling of RF1, *Nat. Commun.* *9*, 3053.
- [193] Rundlet, E. J., Holm, M., Schacherl, M., Natchiar, S. K., Altman, R. B., Spahn, C. M. T., Myasnikov, A. G., and Blanchard, S. C. (2021) Structural basis of early translocation events on the ribosome, *Nature* *595*, 741-745.
- [194] Ermolenko, D. N., and Noller, H. F. (2011) mRNA translocation occurs during the second step of ribosomal intersubunit rotation, *Nat. Struct. Mol. Biol.* *18*, 457-462.
- [195] Rae, C. D., Gordiyenko, Y., and Ramakrishnan, V. (2019) How a circularized tmRNA moves through the ribosome, *Science* *363*, 740-744.
- [196] Neubauer, C., Gillet, R., Kelley, A. C., and Ramakrishnan, V. (2012) Decoding in the absence of a codon by tmRNA and SmpB in the ribosome, *Science* *335*, 1366-1369.
- [197] Moore, S. D., and Sauer, R. T. (2007) The tmRNA system for translational surveillance and ribosome rescue, *Annu. Rev. Biochem.* *76*, 101-124.
- [198] Valle, M., Gillet, R., Kaur, S., Henne, A., Ramakrishnan, V., and Frank, J. (2003) Visualizing tmRNA entry into a stalled ribosome, *Science* *300*, 127-130.
- [199] Zeng, F., Chen, Y., Remis, J., Shekhar, M., Phillips, J. C., Tajkhorshid, E., and Jin, H. (2017) Structural basis of co-translational quality control by ArfA and RF2 bound to ribosome, *Nature* *541*, 554-557.
- [200] Ma, C., Kurita, D., Li, N., Chen, Y., Himeno, H., and Gao, N. (2017) Mechanistic insights into the alternative translation termination by ArfA and RF2, *Nature* *541*, 550-553.
- [201] Huter, P., Muller, C., Beckert, B., Arenz, S., Berninghausen, O., Beckmann, R., and Wilson, D. N. (2017) Structural basis for ArfA-RF2-mediated translation termination on mRNAs lacking stop codons, *Nature* *541*, 546-549.
- [202] Demo, G., Svidritskiy, E., Madireddy, R., Diaz-Avalos, R., Grant, T., Grigorieff, N., Sousa, D., and Korostelev, A. A. (2017) Mechanism of ribosome rescue by ArfA and RF2, *Elife* *6*.
- [203] James, N. R., Brown, A., Gordiyenko, Y., and Ramakrishnan, V. (2016) Translational termination without a stop codon, *Science* *354*, 1437-1440.
- [204] Shimizu, Y. (2012) ArfA recruits RF2 into stalled ribosomes, *J. Mol. Biol.* *423*, 624-631.
- [205] Chadani, Y., Ito, K., Kutsukake, K., and Abo, T. (2012) ArfA recruits release factor 2 to rescue stalled ribosomes by peptidyl-tRNA hydrolysis in *Escherichia coli*, *Mol. Microbiol.* *86*, 37-50.
- [206] Chadani, Y., Ono, K., Ozawa, S., Takahashi, Y., Takai, K., Nanamiya, H., Tozawa, Y., Kutsukake, K., and Abo, T. (2010) Ribosome rescue by *Escherichia coli* ArfA (YhdL) in the absence of trans-translation system, *Mol. Microbiol.* *78*, 796-808.
- [207] Handa, Y., Inaho, N., and Nameki, N. (2011) YaeJ is a novel ribosome-associated protein in *Escherichia coli* that can hydrolyze peptidyl-tRNA on stalled ribosomes, *Nucl. Acids Res.* *39*, 1739-1748.
- [208] Chadani, Y., Ono, K., Kutsukake, K., and Abo, T. (2011) *Escherichia coli* YaeJ protein mediates a novel ribosome-rescue pathway distinct from SsrA- and ArfA-mediated pathways, *Mol. Microbiol.* *80*, 772-785.

- [209] Chan, K. H., Petrychenko, V., Mueller, C., Maracci, C., Holtkamp, W., Wilson, D. N., Fischer, N., and Rodnina, M. V. (2020) Mechanism of ribosome rescue by alternative ribosome-rescue factor B, *Nat. Commun.* **11**, 4106.
- [210] Carbone, C. E., Demo, G., Madireddy, R., Svidritskiy, E., and Korostelev, A. A. (2020) ArfB can displace mRNA to rescue stalled ribosomes, *Nat. Commun.* **11**, 5552.
- [211] Basu, A., Shields, K. E., and Yap, M. F. (2020) The hibernating 100S complex is a target of ribosome-recycling factor and elongation factor G in *Staphylococcus aureus*, *J. Biol. Chem.* **295**, 6053-6063.
- [212] Basu, A., and Yap, M. N. (2017) Disassembly of the *Staphylococcus aureus* hibernating 100S ribosome by an evolutionarily conserved GTPase, *Proc. Natl. Acad. Sci. U S A* **114**, E8165-E8173.
- [213] Bolard, A., Plesiat, P., and Jeannot, K. (2018) Mutations in Gene fusA1 as a Novel Mechanism of Aminoglycoside Resistance in Clinical Strains of *Pseudomonas aeruginosa*, *Antimicrob Agents Chemother* **62**.
- [214] Ramsay, K. A., McTavish, S. M., Wardell, S. J. T., and Lamont, I. L. (2021) The Effects of Sub-inhibitory Antibiotic Concentrations on *Pseudomonas aeruginosa*: Reduced Susceptibility Due to Mutations, *Front Microbiol* **12**, 789550.
- [215] Abisado-Duque, R. G., Townsend, K. A., McKee, B. M., Woods, K., Koirala, P., Holder, A. J., Craddock, V. D., Cabeen, M., and Chandler, J. R. (2023) An Amino Acid Substitution in Elongation Factor EF-G1A Alters the Antibiotic Susceptibility of *Pseudomonas aeruginosa* LasR-Null Mutants, *J Bacteriol* **205**, e0011423.
- [216] Thacharodi, A., and Lamont, I. L. (2023) Gene-Gene Interactions Reduce Aminoglycoside Susceptibility of *Pseudomonas aeruginosa* through Efflux Pump-Dependent and -Independent Mechanisms, *Antibiotics (Basel)* **12**.
- [217] Cardone, G., Heymann, J. B., and Steven, A. C. (2013) One number does not fit all: mapping local variations in resolution in cryo-EM reconstructions, *J Struct Biol* **184**, 226-236.
- [218] Larkin, M. A., Blackshields, G., Brown, N. P., Chenna, R., McGettigan, P. A., McWilliam, H., Valentin, F., Wallace, I. M., Wilm, A., Lopez, R., Thompson, J. D., Gibson, T. J., and Higgins, D. G. (2007) Clustal W and Clustal X version 2.0, *Bioinformatics* **23**, 2947-2948.
- [219] Robert, X., and Gouet, P. (2014) Deciphering key features in protein structures with the new ENDscript server, *Nucleic Acids Res* **42**, W320-324.

Vita

Savannah attended The University of Texas at Tyler and earned a Bachelor of Science in Biochemistry in May of 2019. Savannah then entered the Biochemistry and Molecular Biology graduate program at The University of Texas Medical Branch in Galveston, Texas in August 2018. In March 2019, Savannah joined the laboratory of Dr. Matthieu Gagnon where she conducted biochemical and structural studies of the bacterial ribosome, focusing on mechanisms of ribosome recycling and ribosome rescue in the context of antibiotic resistance. Savannah published three first author articles in *RNA Biology*, *Nature Communications*, and *Nucleic Acids Research*. Savannah also received numerous awards including UTMB scholarships and a predoctoral fellowship from the Houston Area Molecular Biophysics Training Program. Savannah was awarded the degree of Doctor of Philosophy in May 2024.

Publications:

1. **Seely SM**, Basu RB, Gagnon MG. Mechanistic insights into the alternative ribosome recycling by HflXr. *Nucleic Acids Res.* 2024 Feb 26:gkae128. doi: 10.1093/nar/gkae128. Epub ahead of print. Erratum in: *Nucleic Acids Res.* 2024 Mar 18;; PMID: 38407413.
2. **Seely SM**, Parajuli NP, De Tarafder A, Ge X, Sanyal S, Gagnon MG. Molecular basis of the pleiotropic effects by the antibiotic amikacin on the ribosome. *Nat Commun.* 2023 Aug 3;14(1):4666. doi: 10.1038/s41467-023-40416-5. PMID: 37537169; PMCID: PMC10400623.
3. **Seely SM**, Gagnon MG. Mechanisms of ribosome recycling in bacteria and mitochondria: a structural perspective. *RNA Biol.* 2022;19(1):662-677. doi: 10.1080/15476286.2022.2067712. Epub 2021 Dec 31. PMID: 35485608; PMCID: PMC9067457.

This dissertation was typed by the author